Geometry and Mechanics of Self-Assembled Colloidal Membranes

by

Leroy L. Jia

B.S., Georgia Institute of Technology, GA, 2012

B.S., Georgia Institute of Technology, GA 2012

Sc.M., Brown University, RI, 2013

Sc.M., Brown University, RI, 2017

A dissertation submitted in partial fulfillment of the
requirements for the degree of Doctor of Philosophy
in The Division of Applied Mathematics at Brown University

PROVIDENCE, RHODE ISLAND

May 2018

This dissertation by Leroy L. Jia is accepted in its present form
by The Division of Applied Mathematics as satisfying the
dissertation requirement for the degree of Doctor of Philosophy.

Date_____ _____

Thomas R. Powers, Ph.D., Advisor

Recommended to the Graduate Council

Date_____ _____

Robert A. Pelcovits, Ph.D., Advisor

Date_____ _____

Anastasios Matzavinos, Ph.D., Reader

Approved by the Graduate Council

Date_____ _____

Andrew G. Campbell, Dean of the Graduate School

Vitae

Leroy L. Jia is from the Atlanta Metropolitan area. He studied physics and applied mathematics at Georgia Tech before coming to Brown University for graduate school in applied mathematics. This thesis was defended on May 7, 2018.

Preface

The research described herein was conducted under the supervision of Professor Thomas R. Powers (School of Engineering and Department of Physics) and Professor Robert A. Pelcovits (Department of Physics). Part of the work presented in this dissertation appeared in or is being prepared in the following publications:

Chapter 1:

- T. Gibaud, C. N. Kaplan, P. Sharma, M. J. Zakhary, A. Ward, R. Oldenbourg, R. B. Meyer, R. D. Kamien, T. R. Powers, Z. Dogic, Achiral symmetry breaking and positive Gaussian modulus lead to scalloped colloidal membranes. *Proc. Natl. Acad. Sci.* **114** E3376 (2017). T.G., R.B.M., and Z.D. designed research; C.N.K. developed the theoretical model of defect interactions; R.D.K. and T.R.P. provided theoretical estimate of the Gaussian curvature modulus; R.B.M. contributed to the theoretical model; T.G., C.N.K., P.S., M.J.Z., and A.W. performed research; R.O. contributed new reagents/analytic tools; P.S. acquired coalescence movies; A.W. contributed optical-tweezer measurements; R.O. contributed microscopy expertise; T.G., C.N.K., and T.R.P. analyzed data; and T.G., C.N.K., T.R.P., and Z.D. wrote the paper.

Chapter 2:

- L. L. Jia, M. J. Zakhary, Z. Dogic, R. A. Pelcovits, T. R. Powers, Chiral edge fluctuations of colloidal membranes. *Phys. Rev. E* **95** 060701(R) (2017). Z.D., R.A.P., and T.R.P. designed research; L.L.J. and M.J.Z. performed research.

Chapter 3:

- A. Balchunas, L. L. Jia, P. Sharma, Z. Dogic, R. A. Pelcovits, T. R. Powers, Tunable Gaussian curvature modulus directs unduloid formation from 2D colloidal membranes*. To be submitted in 2018. A.B., L.L.J., and P.S. performed research; Z.D., R.A.P., and T.R.P. designed research.

- J. Robaszewski, L. L. Jia, Z. Dogic, R. A. Pelcovits, T. R. Powers†, Inducing Vesicle Formation in Colloidal Membranes by Controlling Membrane Thickness*. To be submitted. J.R. and L.L.J. performed research; Z.D., R.A.P., and T.R.P. designed research.

- S. Pei, L. L. Jia, R. A. Pelcovits, T. R. Powers, Force vs. extension for stiff catenoids*. To be submitted in 2018. S.P. and L.L.J. performed research; R.A.P. and T.R.P. designed research.

Chapter 4:

- A. Balchunas, L. L. Jia, M. J. Zakhary, Z. Dogic, R. A. Pelcovits, T. R. Powers. Stretching induced disk-to-ribbon transition of chiral colloidal membranes*. To be submitted in 2018. A.B., L.L.J., and M.J.Z. performed research; Z.D., R.A.P., and T.R.P. designed research.

L.L.J., R.A.P, and T.R.P. were supported by National Science Foundation grants MRSEC-1420382 and CMMI-1634552. L.L.J., R.A.P., and T.R.P. also thank the Brandeis Materials Research Science and Engineering Center for funding and resources.

*indicates temporary title for work not yet submitted

†indicates temporary author list for work not yet finished

Acknowledgements

As the old Chinese saying goes, 饮水思源—loosely translated, it means "When you drink from the river, remember its source." These past five plus years, I have had the privilege of drinking deeply from a river of knowledge, partaking in exciting academic adventures and collecting valuable life experiences along the way. Now that my time at graduate school is nearing an end, it is only proper that I express my gratitude to those who made this dream achievable, in the spirit of 饮水思源.

First and foremost, I owe too much to my advisors Tom Powers and Bob Pelcovits, who took me under their wings and shouldered the enormous task of guiding my journey through graduate school. I have benefited enormously from their insight, feedback, encouragement, and advice—to say that they have been critical to my development as a scientist would be an egregious understatement. It really is impossible to thank Tom and Bob enough for all that they have given me, and I count myself fortunate to have found such wonderful mentors.

The scientific work in this document is based on the elegant experiments of Zvonimir Dogic (UCSB) and his team at Brandeis University. I would like to especially thank Andrew Balchunas, Joanna Robaszewski, and Mark Zakhary (Mayo Clinic) for working tirelessly to provide data, images, and feedback, which appear in the pages below. I am also fortunate to have been part of the Brandeis Materials Research Science and Engineering Center, which has enhanced my professional development

by providing funding[‡] and collaborative opportunities.

Other professional thanks to my DAM reader, Tasos Matzavinos, as well as the rest of the faculty of the Divison of Applied Mathematics and the School of Engineering including: Yan Guo, David Hennan, Shreyas Mandre, Bjorn Sandstede, and Petia Vlahovska (Northwestern)—as well as my academic siblings Juan Shi, Ski Krieger, Harsh Soni, and Dan Beller, all of whom helped me out at one point or another.

Beyond academia, my deepest gratitude goes to my brothers Leo and Leigh and my parents James and Lynn, who supported me every step of the way. They taught me what my (what is getting to become an uncomfortably large number of) years of school could not. Additional thanks to the many, many wonderful people I am proud to call my friends—there are too many of them to name here, but without their emotional support, I would never have seen the light at the end of this tunnel.

Lastly, this endeavor would not have been possible without the myriad scientists who came before me, whose discoveries I used to illuminate my own, nor without my dedicated teachers, who showed me the incomparable splendor of mathematics as a youth. Being able to lay my own infinitesimal scientific contribution on top of theirs is a tremendous honor, but I am only able to do so by standing on their shoulders. As I do not have the space to thank these lodestars by name, I will simply quote:

"What more can I say?
I wouldn't be here today
if the Old School didn't pave the way."
—2Pac (sampling Grand Puba)

[‡]This work was supported in part by the National Science Foundation through Grants No. MRSEC-1420382 and No. CMMI-1634552.

Abstract of " Geometry and Mechanics of Self-Assembled Colloidal Membranes " by Leroy L. Jia, Ph.D., Brown University, May 2018

Colloidal membranes are an example of a novel bioinspired soft material with rich properties that stem from the interplay of geometry and molecular order. A colloidal membrane is a two-dimensional monolayer composed of colloidal particles—in this case, rod-shaped viruses roughly 1 micron long and 6 nm in diameter—that are bound by entropic depletion forces. Because of their relatively large (micron) size, these membranes can be manipulated directly in the laboratory, offering a promising avenue to study other similar systems of biological importance such as lipid bilayer membranes or the endoplasmic reticulum.

Perhaps the most notable feature of these colloidal membranes is their propensity to bend into exotic shapes such as saddles, unduloids, helicoidal ribbons, and closed vesicles under appropriate conditions. Strikingly, many of these shapes have zero mean curvature and/or negative Gaussian curvature, which contrasts with the case for other commonly encountered membranes and materials. Using a combination of theory and experiments, we put forth a minimal model based only on geometric quantities—such as length, curvature, and geodesic torsion—to describe these phases mathematically and characterize the conditions under which they appear. Our effective model is most valid when the twist penetration depth of the membrane is much smaller than the membrane length scale—if this is the case, then it provides a way to describe membrane configurations without resorting to calculation of the cumbersome full liquid crystal energy.

Contents

Vitae **iv**

Preface **v**

Acknowledgments **vii**

1 Introduction **1**
1.1 Mathematical background 2
1.1.1 Geometry of curves 2
1.1.2 Geometry of surfaces 5
1.2 Description of colloidal membranes 12
1.3 A mathematical model for colloidal membranes 15
1.3.1 Canham-Helfrich membrane energy 15
1.3.2 Entropy favors positive Gaussian curvature modulus 17
1.3.3 Liquid crystalline energy 21
1.3.4 Edge energy and effective geometric theory 22

2 Chiral Edge Fluctuations **25**
2.1 Introduction 26
2.2 Description of experiments 27
2.3 Stability criteria for a flat membrane with edge 28
2.4 Stability criteria for a disk 32
2.5 Expressions for the fluctuation spectrum 35

3 Axisymmetric Membranes **39**
3.1 Introduction 40
3.2 Arclength parameterization 41
3.3 Coalesence of saddles into unduloids 42
3.3.1 Experimental methods 44
3.3.2 Spontaneous curvature as a function of long rod fraction . . . 45
3.3.3 Delaunay surfaces 48

3.3.4 Critical Gaussian curvature modulus for unduloid formation . 50
3.3.5 Comparison with full liquid crystal energy 50
3.4 Willmore surfaces with fixed area 52
3.5 Colloidal vesicles 55
3.5.1 Experimental methods 57
3.5.2 Minimal model for vesicles 58
3.5.3 Estimating the bending rigidity 60
3.5.4 Vesicle with a hole 62

4 Force vs. Extension of Ribbons 66
4.1 Introduction 67
4.2 Experimental methods 67
4.3 Small extensions of a flat membrane 69
4.4 A simplified strip model 76
4.4.1 Asymptotic formulas for large extension 77
4.4.2 Second order strip-to-ribbon transition 78
4.4.3 Adding a chiral term 80
4.5 Effective model for a helicoid 81
4.5.1 Energy and Euler-Lagrange equations 82
4.5.2 Achiral vs chiral ribbons 86

5 Conclusion 89
5.1 Summary 90
5.2 Future work 91

A Force- and Torque-Free Boundary Conditions for the Minimal Model 93
A.1 The membrane shape equation 94
A.2 Natural boundary conditions 95

B Euler-Lagrange Equations for an Axisymmetric Membrane 97
B.1 Euler-Lagrange equations for the minimal model 98
B.2 Force- and Torque-free boundary conditions for the minimal model . 100
B.3 The transversality condition for problems with unknown length . . . 101
B.4 Euler-Lagrange equations for the full liquid crystal energy 103
B.5 Force- and Torque-free boundary conditions for the full liquid crystal energy 108

List of Figures

1.1 Principal, mean, and Gaussian curvatures 9
1.2 Physical origin of the depletion interaction 12
1.3 Visualizations of a colloidal membrane 13
1.4 Distortions in a nematic liquid crystal 21
1.5 Approximate rod orientation in a colloidal disk 24

2.1 Disk-to-ribbon transition of a colloidal membrane 26
2.2 Edge fluctuations of a chiral membrane for various temperatures . . . 27
2.3 Semi-infinite surface with chiral edge 29
2.4 Phase diagram for flat and rippled edges of chiral membranes 32
2.5 Phase diagrams for flat and rippled chiral disks 35
2.6 Normalized power spectrum for chiral membrane 36
2.7 Fitted values of line tension and effective chirality modulus 36

3.1 Parameterization of an axisymmetric shape 40
3.2 Merging of saddles into an unduloid 43
3.3 Experimental phase diagram for membranes doped with short rods . 45
3.4 Spontaneous curvature induced by the addition of shorter rods 47
3.5 Experimental unduloid height data and theoretical profile 47
3.6 Critical Gaussian curvature modulus for unduloid formation 49
3.7 Comparison of minimal model and full liquid crystal model for unduloids 51
3.8 Force vs. extension of a membrane with the topology of a catenoid . 54
3.9 Formation of tethers in the extension of a large catenoidal membrane 56
3.10 Comparison of a catenoid and a ''flatenoid" 57
3.11 Images of a fluorescent colloidal vesicle 58
3.12 Vesicle shapes as a function of α 61
3.13 Comparison of experimental vesicle profiles and theoretical shape . . 61
3.14 A spherical cap of radius r. 62
3.15 Metastable shapes of a vesicle with a hole 64
3.16 Wrapping of a disk into an axisymmetric vesicle. 64

4.1 Stretch of disk-shaped membrane with optical tweezers 69

4.2 Force vs. extension for colloidal membranes of various radii 70
4.3 Forces acting diametrically on a disk 70
4.4 Dependence of effective spring constant on edge bending stiffness . . . 75
4.5 Energy, force, twist rate, and half-width as a function of extension . . 80
4.6 Effect of chirality on twist rate for a strip 81
4.7 Stretched chiral and achiral membranes 85
4.8 Helicoidal solution to the membrane shape equation 87
4.9 Theoretical force vs. extension curve compared to experiment 88

5.1 A larger unduloidal membrane 91

Chapter One

Introduction

1.1 Mathematical background

The mathematical modeling of membranes makes heavy use of tools from differential geometry. While geometry is a very deep and comprehensive subject, we will for the most part only require notions from one- and two-dimensions, which we outline below. For brevity, proofs are omitted; details can be found in the reference [22].

1.1.1 Geometry of curves

Curves are the simplest nontrivial manifolds to study geometrically yet are surprisingly relevant in physical models; filaments [52], flagella [11], and boundaries of open surfaces [29] are all modeled as one-dimensional nonlinear objects. Here, we review the basic definitions and results from the theory of curves.

Definition: A *curve* is a continuous function $\underline{\gamma} : I \to X$, where $I = [a, b]$ is an interval of $\mathbb{R}$ and X is a topological space. For our purposes, we will assume the curve is also differentiable and that $X = \mathbb{R}^3$. We will also assume that curves are parameterized in t.

Now we introduce the notion of distance or length along a curve, inspired by integrating the Eulerian distance formula. (A differentiable curve looks locally linear.)

Definition: The *arc length* of a curve $\underline{\gamma} : [a, b] \to \mathbb{R}^3$ is defined as $s = \int_a^b |\underline{\gamma}'(t)|dt$.

Note that the arc length of a curve is invariant under reparameterization and therefore a differential geometric property of the curve. We can define an arc length function $s(t)$ that measures the arc length of $\underline{\gamma}$ from a to a point $t \leq b$. The

monotonicity of this function allows us to define an inverse $t(s)$. This *arc length parameterization* is very natural to use because $|\underline{\gamma}'(t(s))| = 1$ (a particle traveling along $\underline{\gamma}$ has unit speed in this parameterization).

Notation: In differential form, the above integral can be summarized as $ds = |\underline{\gamma}'(t)|dt$. We will use dot notation $\dot{(\ldots)} = \frac{d(\ldots)}{ds}$ to represent the derivative with respect to arc length and the usual prime notation to represent differentiation with respect to the original parameter t.

Definition: The *tangent vector* of a curve $\underline{\gamma} : [a, b] \to \mathbb{R}^3$ is defined as $\hat{T}(s) = d\underline{\gamma}/ds$.

Definition: The *normal vector* of a curve $\underline{\gamma} : [a, b] \to \mathbb{R}^3$ is defined as $\hat{N}(s) = \dot{\hat{T}}/|\dot{\hat{T}}|$, assuming the denominator is nonzero.

Note that because of the arc length parameterization, $\hat{T}(s)$ is guaranteed to be a unit vector. Also, it is easy to show $\hat{N}$ is automatically orthonormal to $\hat{T}$ (if they exist). So, it makes sense to complete the triple:

Definition: The *binormal vector* of a curve $\underline{\gamma} : [a, b] \to \mathbb{R}^3$ is defined as $\hat{B}(s) = \hat{T}(s) \times \hat{N}(s)$.

Definition: The orthonormal basis for $\mathbb{R}^3$ formed by the triple of vectors $\{\hat{T}, \hat{N}, \hat{B}\}$ is called the *Frenet frame*.

Now we will discuss two more essential geometric properties of curves.

Definition: The *curvature* κ of a curve $\underline{\gamma} : [a, b] \to \mathbb{R}^3$ with tangent vector $\hat{T}$ is

$$\kappa(s) = \left| \frac{d\hat{T}}{ds} \right| \tag{1.1}$$

and $\rho(s) = 1/\kappa(s)$ is called the *radius of curvature* of $\underline{\gamma}$ at s. As defined here, the curvature and radius of curvature are always nonnegative.

The curvature measures the rate of rotation of the tangent vector around the binormal. Intuitively, the curvature measures the failure of a curve to be straight ($\kappa = 0$ everywhere if and only if $\underline{\gamma}$ is a straight line). If κ is small, the curve is changing direction slowly; if κ is large, the curve is turning sharply.

Definition: The *torsion* τ of a curve $\underline{\gamma} : [a, b] \to \mathbb{R}^3$ with normal $\hat{N}$ and binormal $\hat{B}$ is defined as

$$\tau(s) = -\hat{N} \cdot \frac{d\hat{B}}{ds}. \tag{1.2}$$

The torsion measures the rate of rotation of the binormal around the tangent. Intuitively, it measures the failure of a curve to be planar. A curve with a large torsion is "twisitng" out of plane heavily ($\tau = 0$ everywhere if and only if $\underline{\gamma}$ is planar). Note that the torsion is a signed quantity; the sign depends on the handedness of the twisting. Both κ and τ do not depend on the choice of parameterization, which leads into the two most important results about the geometry of curves.

Theorem: The *Frenet-Serret equations* describe how the Frenet frame varies along $\underline{\gamma}(s)$:

$$\begin{cases} \dot{\hat{T}} = \kappa \hat{N} \\ \dot{\hat{N}} = -\kappa \hat{T} + \tau \hat{B} \\ \dot{\hat{B}} = -\tau \hat{N} \end{cases} \tag{1.3}$$

Proving these equations is not difficult. The first one is a restatement of the definition of curvature and the third is a restatement of the definition of torsion. The second can be derived by differentiating the fact that $\hat{N} \cdot \hat{N} = 1$. These three equations lead us to the following

Theorem: The *Fundamental Theorem of Curves* states that given continuous functions $\kappa(s)$ and $\tau(s)$, $s > 0$, then there exists exactly one curve with arc length s, curvature $\kappa(s)$, and torsion $\tau(s)$, up to orientation and position in space.

This theorem is proved by integrating the system of ordinary differential equations given by the Frenet-Serret equations. Essentially, every curve in 3-dimensional space is uniquely determined by its curvature and torsion (up to rigid rotations and translations).

1.1.2 Geometry of surfaces

We now turn our attention to surfaces, where the goal is to measure the usual geometric quantities (lengths, areas, angles, etc.) in curved coordinates. Generally, surfaces are more complex than curves because surfaces can carry *intrinsic geometry*; that is, properties that can be measured within the surface itself and without reference to the ambient space. Here is an overview of the most important definitions and results of surfaces; again, details can be found in [22].

Definition: A *surface* S is a differentiable 2-manifold. We will assume our surface is in $\mathbb{R}^3$, connected, and sufficiently smooth. We will also assume a parametrization $\underline{r} : D \to \mathbb{R}^3$ where D is an open subset of $\mathbb{R}^2$ and is described with parameters (u^1, u^2).

Assuming such a parameterization, we can define at every point two tangent vectors $\underline{r}_1 = \partial\underline{r}/\partial u^1$ and $\underline{r}_2 = \partial\underline{r}/\partial u^2$ (subscripts denote partial differentiation with respect to u^1 or u^2). We will assume these vectors are linearly independent (but not necessarily orthogonal) and therefore span a plane at every point p on S called the *tangent space*, T_pS. From this, we define

Definition: The *first fundamental form (metric tensor)* is defined as $ds^2 = g_{11}(du^1)^2 + 2g_{12}du^1du^2 + g_{22}(du_2)^2$ where $g_{11} = \underline{r}_1 \cdot \underline{r}_1$, $g_{12} = \underline{r}_1 \cdot \underline{r}_2$, and $g_{22} = \underline{r}_2 \cdot \underline{r}_2$. In index notation, $g_{\alpha\beta} = \underline{r}_\alpha \cdot \underline{r}_\beta$ and $ds^2 = g_{\alpha\beta}du^\alpha du^\beta$. We also define $g = \sqrt{g_{11}g_{22} - g_{12}^2}$ (the determinant if the first fundamental form is written as a matrix).

Where does this come from? Suppose that a curve is lying on the surface so that the coordinates of the curve can be defined by $\gamma(t) = \underline{r}(u^1(t), u^2(t))$. By the chain rule:

$$ds = |\gamma'(t)|dt = \left|\underline{r}_1\frac{du^1}{dt} + \underline{r}_2\frac{du^2}{dt}\right| dt = \sqrt{g_{\alpha\beta}du^\alpha du^\beta} \tag{1.4}$$

So, the differential line element for the curve is given by the first fundamental form. This enables us to measure distances along curves on a surface

$$s(t_0, t_1) = \int_{t_0}^{t_1} \sqrt{g_{\alpha\beta}\frac{du^\alpha}{dt}\frac{du^\beta}{dt}}dt \tag{1.5}$$

Now we make contact with Euclidean geometry: the scalar product between vectors in the tangent space at the same point $p \in S$ looks like: $\underline{a} \cdot \underline{b} = (a^1\underline{r}_1 + a^2\underline{r}_2) \cdot (b^1\underline{r}_1 + b^2\underline{r}_2) = g_{\alpha\beta}a^\alpha b^\beta$. The magnitude of a vector is still $|\underline{a}| = \sqrt{\underline{a} \cdot \underline{a}} = \sqrt{g_{\alpha\beta}a^\alpha a^\beta}$. The angle between two vectors $\underline{a}$ and $\underline{b}$ in S can be found by computing the usual formula

$$\theta = \cos^{-1}\left(\frac{\underline{a} \cdot \underline{b}}{|\underline{a}||\underline{b}|}\right) = \frac{g_{\alpha\beta}a^\alpha b^\beta}{\sqrt{g_{\mu\nu}a^\mu b^\nu}\sqrt{g_{\sigma\tau}a^\sigma b^\tau}} \tag{1.6}$$

We can also define an area element using the fact that $g = |\underline{r}_1 \times \underline{r}_2|^2$ is related to the area of the parallelogram spanned by vectors $\underline{r}_1$ and $\underline{r}_2$.

$$dA = \sqrt{g} du^1 du^2 \tag{1.7}$$

This also allows us to define the *surface normal*, given by $\hat{n} = \underline{r}_1 \times \underline{r}_2 / \sqrt{g}$. All of these formulas reduce to the standard Euclidean formulas for flat surfaces with $(u^1, u^2) = (x, y)$.

For a curve that lies on a surface, we can define a moving frame similar to the Frenet-Serret frame but replaces the normal to the curve with the normal to the surface. Let $\underline{\gamma}$ be a curve lying in the surface S and define $\hat{e}_1 = d\underline{\gamma}/ds = \hat{T}$ and $\hat{e}_3 = \hat{n}$. The orthonormal frame, called the *Frenet-Darboux frame*, is completed by defining $\hat{e}_2 = \hat{e}_3 \times \hat{e}_1$. Note that $\hat{e}_1, \hat{e}_2 \in TS$.

One can compare the Frenet-Serret and Frenet-Darboux frames; since in both cases the tangent to the curve is the same, there is a unique angle α such that a rotation in the plane of $\hat{N}$ and $\hat{B}$ produces the pair $\hat{e}_2$ and $\hat{e}_3$.

$$\begin{bmatrix} \hat{e}_1 \\ \hat{e}_2 \\ \hat{e}_3 \end{bmatrix} = \begin{bmatrix} 1 & 0 & 0 \\ 0 & \cos\alpha & \sin\alpha \\ 0 & -\sin\alpha & \cos\alpha \end{bmatrix} \begin{bmatrix} \hat{T} \\ \hat{N} \\ \hat{B} \end{bmatrix}$$

Differentiating these equations and substituting in the Frenet-Serret equations gives the *Frenet-Darboux equations*:

$$\begin{cases} \dot{\hat{e}}_1 = \kappa_g \hat{e}_2 + \kappa_n \hat{e}_3 \\ \dot{\hat{e}}_2 = -\kappa_g \hat{e}_2 + \tau_g \hat{e}_3 \\ \dot{\hat{e}}_3 = -\kappa_n \hat{e}_1 - \tau_g \hat{e}_2 \end{cases} \tag{1.8}$$

where $\kappa_g = \kappa \sin\alpha$ is the geodesic curvature, $\kappa_n = \kappa\cos\alpha$ is the normal curvature, and $\tau_g = \tau + \dot{\alpha}$ is the geodesic torsion. Removing α, equivalent expressions can be derived:

$$\kappa_g = \hat{T} \cdot \left(\frac{d\hat{T}}{ds} \times \hat{n} \right) \tag{1.9}$$

$$\kappa_n = \hat{n} \cdot \frac{d\hat{T}}{ds} \tag{1.10}$$

$$\tau_g = \hat{T} \cdot \left(\hat{n} \times \frac{d\hat{n}}{ds} \right) \tag{1.11}$$

Now we wish to discuss the notion of curvature of a surface. Recall that the curvature of a curve was given by taking the magnitude of the second derivative (w.r.t. arc length) of the curve's coordinates. A curve lying on a surface can bend in two ways: in the plane or out of plane (which gives rise to the idea of geodesic vs. normal curvature). Since when we think of a curved surface we think of out of plane bending, we only want the component of the curvature along the surface normal: $\kappa\cos\alpha = \kappa\hat{N}\cdot\hat{n}$, where α is the angle between the normal to the curve, $\hat{N}$, and the normal to the surface, $\hat{n}$. We calculate:

$$\kappa\cos\gamma = \kappa\hat{N}\cdot\hat{n} = \underline{\ddot{r}}\cdot\hat{n} = (\underline{r}_{\alpha\beta}\dot{u}^\alpha\dot{u}^\beta + \underline{r}_\alpha\ddot{u}^\alpha)\cdot\hat{n} = (\underline{r}_{\alpha\beta}\cdot\hat{n})\dot{u}^\alpha\dot{u}^\beta$$

This tells us that the normal curvature of a surface is related to the tensor of second partials dotted with $\hat{n}$, motivating

Definition: The *second fundamental form* is defined as $b_{11}(du^1)^2 + 2b_{12}du^1du^2 + b_{22}(du^2)^2$, where $b_{11} = \underline{r}_{11}\cdot\hat{n}$, $b_{12} = \underline{r}_{12}\cdot\hat{n}$, and $b_{22} = \underline{r}_{22}\cdot\hat{n}$. In index notation, $b_{\alpha\beta} = \underline{r}_{\alpha\beta}\cdot\hat{n}$. Also define $b = \sqrt{b_{11}b_{22} - b_{12}^2}$ (the determinant of the second fundamental form written as a matrix).

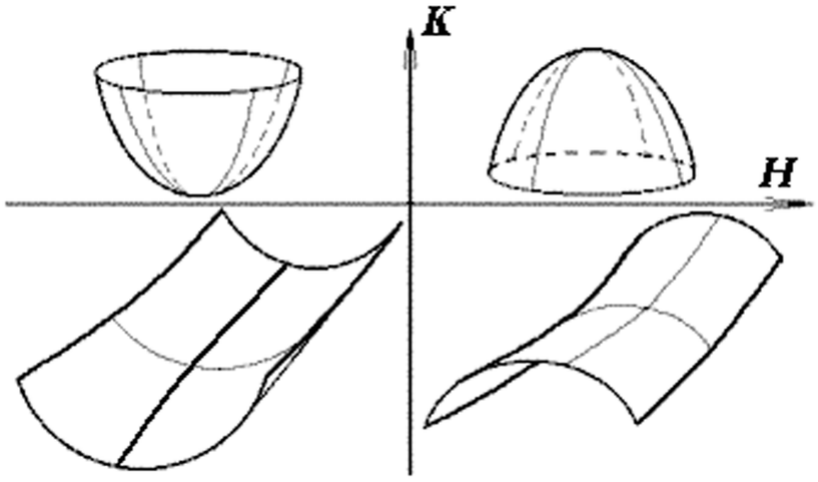

Figure 1.1: Illustrations of principal curvatures for various surfaces. Signs of mean curvature H and Gaussian curvature K are indicated by quadrant. Figure adapted from [58].

At each point p on a surface S with surface normal $\hat{n}$, we can construct infinitely many planes that contain $\hat{n}$. The intersection of each such normal plane and S forms a curve. We can ask what the minimum/maximum normal curvature at p out of all such intersections is; this question is related to the eigenvalues of $b_{\alpha\beta}$. These are called the *principal curvatures* and they provide an idea of what the surface looks like at p (i.e. is it locally parabolic, hyperbolic, flat, etc.). We note that the principal directions are always perpendicular, as a consequence of the symmetry of $b_{\alpha\beta}$. Equivalent to the two principal curvatures are the mean and Gaussian curvatures (Fig. **??**):

Definition: The *mean curvature* H of a surface S at a point p is the arithmetic average of its principal curvatures at p and is equal to $H = \frac{1}{2} b_{\alpha\beta} g^{\alpha\beta}$. A surface with $H = 0$ everywhere is called *minimal*.

Definition: The *Gaussian curvature* K of a surface S at a point p is the product of its principal curvatures at p and is equal to $K = b/g$. A surface with $K = 0$ everywhere is called *developable*.

Note that $H^2 \geq K$. As a consequence, a minimal surface necessarily has nonpositive Gaussian curvature everywhere.

We will now highlight some important theorems about surfaces.

Theorem: The *Weingarten equations* tell us how the surface normal changes along a surface. The linear map that takes a vector in the tangent space at p to the derivative of the normal in that direction is called the *shape operator*. The eigenvalues of the shape operator are the principal curvatures.

$$\frac{\partial \hat{n}}{\partial u^\alpha} = -b_\alpha^\beta \underline{r}_\beta = -g^{\sigma\beta} b_{\alpha\sigma} \underline{r}_\beta \tag{1.12}$$

Theorem: Gauss's *Theorema Egregium* states that the Gaussian curvature of a surface is an intrinsic invariant. It does not change if the surface is bent without stretching, as in the case of a rectangular piece of paper being bent into a cylinder. There is no analogue of this theorem for curves since all curves are locally isometric (via the arc length parameterization) and therefore the curvature and torsion depend strongly on the embedding of the curve in $\mathbb{R}^3$, which makes them so-called *extrinsic* quantities. Note the mean curvature is extrinsic.

Theorem: The *Gauss-Bonnet theorem* states that $\int K dA = 2\pi\chi$ for a closed surface, where χ is the Euler characteristic of the surface. Hence the integral of Gaussian curvature is a topological invariant. For open surfaces, the equality is modified to have an edge term:

$$\int K dA = 2\pi\chi - \int k_g ds. \tag{1.13}$$

Theorem: The *Bonnet theorem* states that if certain integrability conditions are satisfied (the Gauss-Godazzi equations), then given two symmetric positive definite

tensors $g_{\alpha\beta}$ and $b_{\alpha\beta}$, there exists a unique surface (up to rigid motions) with first fundamental form $g_{\alpha\beta}$ and second fundamental form $b_{\alpha\beta}$. This is the surface analogue of the Fundamental Theorem of Curves.

Finally, we wish to discuss the notion of differentiation along a surface. Consider a vector field $\underline{v} = v^j r_j$ and differentiate along a basis direction given by $\underline{r}_k$:

$$\frac{\partial \underline{v}}{\partial u^k} = \frac{\partial v^j}{\partial u_k}\underline{r}_j + v^j \frac{\partial \underline{r}_j}{\partial u^k} \tag{1.14}$$

Note that the first term lies in the tangent space but the second term might not because the basis vectors may be changing. To account for this,

Definition: The *Christoffel symbols* are defined as

$$\Gamma^k_{ij} = \frac{\partial \underline{r}_i}{\partial u^j} \cdot \underline{r}^k = \frac{\partial \underline{r}_i}{\partial u^j} \cdot g^{km}\underline{r}_m \tag{1.15}$$

and can be expressed in terms of the metric tensor and its derivatives:

$$\Gamma^i_{jk} = \frac{1}{2} g^{im}\left(\frac{\partial g_{mk}}{\partial x^l} + \frac{\partial g_{ml}}{\partial x^k} - \frac{\partial g_{kl}}{\partial x^m}\right) \tag{1.16}$$

We can then define

Definition: The *covariant derivative* of a scalar f in the direction of $\underline{r}_i$ is

$$\nabla_i f = \underline{r}_i \cdot \nabla f = \underline{r}_i \frac{\partial f}{\partial u^i} \tag{1.17}$$

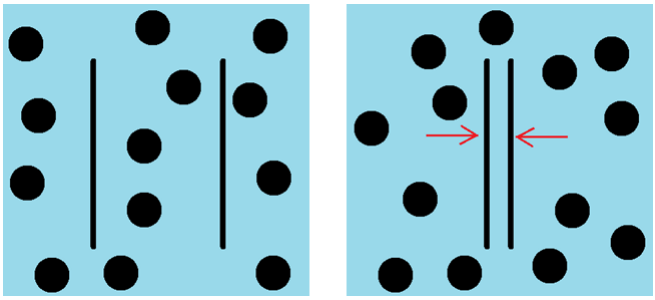

Figure 1.2: (Left) A pair of rods in a polymer solution. There is no interaction if the rods are far enough part. (Right) If the rods are close enough, polymer cannot enter the region between the rods, giving rise to an effective entropic attractive force known as the depletion force.

The *covariant derivative* of a vector $\underline{v}$ in the direction of $\underline{r}_i$ is

$$\nabla_i \underline{v} = \left(\frac{\partial v^k}{\partial u^i} + v^j \Gamma^k_{ij} \right) r_k \tag{1.18}$$

This definition can be extended to handle arbitrary directions (tangent vectors) via linearity and tensors of arbitrary type via the Leibniz rule.

1.2 Description of colloidal membranes

Surfaces that resist bending are ubiquitous in biophysics and soft condensed matter physics. The physics of enclosed cellular membranes [33, 35], organelles such as the endoplasmic reticulum [63, 31], synthetic vesicles [56], polymersomes [21], surfactant interfaces [49], and microemulsions [19] is described by a simple model that accounts for the energy cost of bending with an effective bending modulus κ [13, 33]. Furthermore, experiments have provided quantitative insight into how the bending modulus of such 2D assemblages depends on the properties of the constituent molecules [26, 53]. However, for many processes, such as vesicle fusion in exocytosis, trafficking of proteins, and the resealing of plasma membranes, the free energy associated with an exposed edge plays an equally important role [14]. In conventional

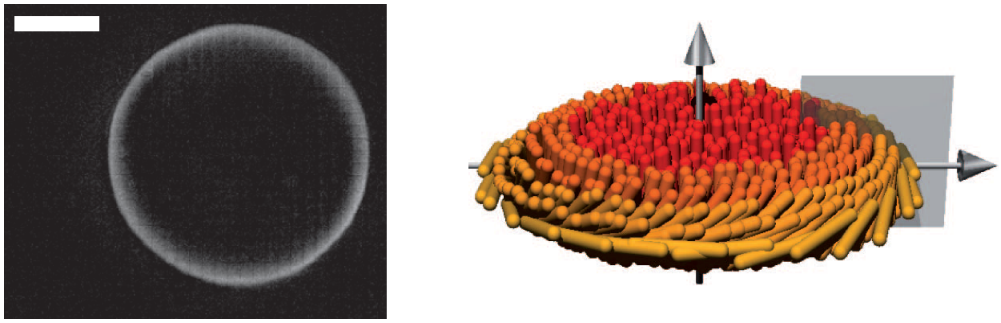

Figure 1.3: (Left)2D LC-PolScope birefringence map of a colloidal membranes. The bright band associated with the edges indicates local rod tilting. Scale bar is 5μm. (Right) Schematic of a colloidal membrane, showing rods near the edge twisting due to surface tension. Color indicates rod orientation relative to surface normal. Images from [27].

membranes edges are associated with transient states that quickly disappear as the assemblage seals itself, making it difficult to experimentally study the properties of the edges.

The colloidal membranes studied in this thesis are composed of rod-like viruses such as fd, which are roughly 880 nm in length and 6 nm in diameter [7, 6, 27, 69]. As the rods have a persistence length of $\sim$2.8 microns [23], they can be considered hard-core particles in aqueous suspension. However, when a polymer such as Dextran is added to the solution, attractive interactions between the rods are induced. Because the polymer coils are not very deformable, their centers cannot come closer than one radius of gyration from the surface of the colloidal particles, leading to a zone around each rod depleted of polymers. When the rods are close enough, the depletion zones overlap and the volume accessible to the polymers increases, leading to an effective entropic attraction between the rods (Fig. 1.2); this attraction is known as the depletion force [2].

The membranes bound by this force are one rod-length thick, fluid-like monolayers and ordinarily assemble into freely suspended disks with exposed edges. When some of the individual virus particles are labeled fluorescently, it is observed that

they rapidly diffuse freely within the membranes with a diffusion constant of $9 \times 10^{-3} \mu m^2/s$ [6], indicating that the membrane is fluid (i.e. does not support a shear). Furthermore, it is observed that the labeled rods stay in the membrane, indicating that there is no exchange of rods between the membranes and the surrounding solvent on experimental time scales. The volume compressibility modulus of these membranes has also been measured to be quite large, on the order of 10^4 pN/μm^2 [4], implying that their volume (or area in the thin membrane approximation) effectively does not change during typical experiments.

Notably, the orientation of the rods in a colloidal membrane is nonuniform, as Fig. 1.3 shows. While the rods in the bulk of the membrane point normal to the membrane surface, rods close to the edge twist to reduce the rod-solvent interface [42]. If the constituent rods are chiral, so that they prefer to align with a twist, this can also contribute to the twisting phenomenon at the edge [27]. It has been shown that the twist profile from edge to center changes exponentially [7, 51]; the length scale of this exponential decay is called the twist penetration depth λ. The twist penetration depth is typically small compared to the membrane length scale—for colloidal membranes, λ is on the order of 1 micron [7, 44, 51].

It is this unique microstructure that endows colloidal membranes with a propensity to form exotic shapes such as helical ribbons and unduloids. In the next few sections, we will take a close look at how to describe these surfaces with a simple model that still captures the essential physics.

1.3 A mathematical model for colloidal membranes

If we make the "thin membrane" approximation and treat these membranes as two-dimensional Riemannian manifolds with fixed area, then the energy has three main components: the elastic bending energy, the liquid crystal energy, and, for open membranes, the edge energy; the shapes are then calculated by finding the minima of this energy. While our analysis is primarily focused on the mechanics, entropy also plays a vital role in determining how the polymer depletants give rise to forces that affect the elastic constants. We finish by describing an effective geometric theory which is applicable when the twist penetration is small.

1.3.1 Canham-Helfrich membrane energy

In the classical theory of elasticity, energy changes in solid plates arise due to stretching, shearing, or bending. For the reasons mentioned above, stretching and shearing are not relevant modes of deformation in membranes, but thin membranes are commonly observed to bend out-of-plane, leading to substantial overall changes in material shape without applying excess stresses. To leading order (quadratic in the principal curvatures), the energy of such deformations can be modeled with the Canham-Helfrich energy functional [13, 33]:

$$E_{CH} = \frac{\kappa}{2}\int (2H - c_0)^2 dA + \bar{\kappa}\int K dA + \mu \int dA. \tag{1.19}$$

where H is the mean curvature, K is the Gaussian curvature, and c_0 is a spontaneous curvature that is nonzero for nonuniform membranes with an intrinsic preferred curvature. The integral is taken over the membrane surface, assumed to be a two-

dimensional manifold. We also introduce μ as a Lagrange multiplier enforcing the constraint of constant area; physically, μ plays the role of a surface pressure or tension that arises to balance external forces.

The modulus κ is called the bending rigidity, and the modulus $\bar{\kappa}$ is called the Gaussian curvature or saddle-splay modulus; they are properties of the material of which the membrane is made. For closed membranes (e.g. vesicles), the Gauss-Bonnet theorem 1.13 allows one to rewrite the Gaussian curvature term as a constant, so that only the first term enters the expression for energy [41, 61]. In general, however, one can rewrite this term as an integral of an edge quantity.

The Euler-Lagrange equation associated with this energy is the partial differential equation

$$\kappa(2H - c_0)(2H^2 - c_0H - 2K) + \kappa\nabla^2(2H) - 2\mu H = 0, \tag{1.20}$$

which we refer to as the shape equation [65]. The boundary conditions that arise naturally from the variation depend on the energy of the edge (see Section 1.3.4) and are summarized in Appendix A for a particular lowest-order model that we will be using. Note that when $c_0 = H = 0$ everwhere, the equation is satisfied, meaning that minimal surfaces are solutions to the shape equation. Indeed, if $2H = c_0$ everywhere, then the equation can be solved with $\mu = 0$. However, without such simplifications, this equation is very challenging to solve, as there exist very few analytical solutions beyond the ones mentioned above. Numerical methods are typically necessary to find nontrivial solutions.

For commonly encountered systems, the moduli κ and $\bar{\kappa}$ are expected to be similar in magnitude, with a bound of the form $-2 < \bar{\kappa}/\kappa < -1/2$ required to ensure the continuum elastic energy is nonnegative [50]. Early work demonstrated that the

height fluctuations of colloidal membranes scales as $1/q^3$ [6], leading to an estimate of $\kappa \approx 150\, k_B T$. However, these numbers are not accurate for colloidal membranes in polymeric suspension. Recent measurements and theoretical estimates of the Gaussian curvature modulus show that $\bar{\kappa} \approx 200\, k_{\rm B} T$ in colloidal membranes [28]. The positive value of $\bar{\kappa}$ is in striking contrast to the case of lipid bilayer membranes, where $\bar{\kappa}$ is typically negative due to the compressive stress in the head groups [36, 37, 60]. However, $\bar{\kappa}$ can be positive in smectic liquid crystals [12] and block copolymers [66].

According to recent measurements of the areal compressibility modulus (by measuring area as a function of depletant concentration) [4], $\kappa \simeq 1.5 \times 10^5 k_B T$, while theoretical esimates suggest $\bar{\kappa} \simeq 200 k_B T$ [28]. The reason for this is thought to be the presence of depletants which entropically prefer surfaces with negative Gaussian curvature; see the next section for a more thorough explanation. Since $\kappa/\bar{\kappa} \gg 1$, colloidal membranes are expected to form nearly minimal surfaces in equilibrium; indeed, this is often observed to be the case.

1.3.2 Entropy favors positive Gaussian curvature modulus

This section summarizes the argument that $\bar{\kappa} > 0$ in colloidal membranes, which first appeared in [28].

For the colloidal membranes consisting of fd virus particles and stabilized by the depletion force arising from small polymers in solution [7], membrane shapes with negative Gaussian curvature such as helicoidal ribbons and concave unduloids are commonly found. The implication is that the Gaussian curvature modulus in these systems is positive. Here we argue that the effect arises from the entropy of the polymers, since surfaces with negative Gaussian curvature have a smaller excluded

volume for the polymers.

First we consider the sphere of radius R, the simplest surface with nonzero mean and Gaussian curvatures. If we slightly thicken the sphere by allowing the radius to grow outward by a small increment $h \ll R$, then the volume V_h of the shell is

$$V_h = Ah\left(1 + \frac{h}{R} + \frac{h^2}{3R}\right) = h\int\left(1 + hH + \frac{h^2K}{3}\right)dA, \tag{1.21}$$

where $A = 4\pi R^2$ is the area of the sphere, H is the mean curvature, and K is the Gaussian curvature. The formula 1.21 can be shown to describe the volume of any surface thickened using this procedure, even if H and K are nonconstant.

The volume of the colloidal membrane from which polymer particles of diameter d are excluded, $V_{ex} = DA + V_{out} + V_{in}$, where V_{out} is the volume of the region formed by thickening the outer surface outward by a distance $d/2$, V_{in} is the volume of the region formed by thickening the inner surface inward by a distance $d/2$, D is the membrane thickness, and A is the area of the middle surface of the membrane. Note that since the outer and inner surfaces of the colloidal membrane are a distance D apart, V_{out} and V_{in} will depend on D. In terms of h, $V_{out} = V_{D/2+d/2} - V_{D/2}$, and $V_{in} = V_{-D/2} - V_{-D/2-d/2}$. Therefore,

$$V_{ex} = (D+d)\int dA + \frac{d}{4}\left(D^2 + Dd + \frac{d^2}{3}\right)\int KdA \simeq D\int dA + \frac{D^2 d}{4}\int KdA \tag{1.22}$$

where we have used the fact that $D \gg d$. The mean curvature terms have dropped out since the polymer particles have access to both sides of the membrane. Membranes with negative Gaussian curvature have a smaller excluded volume than membranes of the same area with nonnegative Gaussian curvature. Thus, there is an entropic driving force favoring negative Gaussian curvature. To estimate the contri-

bution of the depletion forces to the Gaussian curvature modulus, we follow Asakura and Oosawa [3] and let

$$Z = \int dV e^{-w/k_B T} = V - V_{ex} \tag{1.23}$$

be the single-particle partition function for the polymer particles, where w is the hard-core potential, infinitely strong in the excluded volume and vanishing elsewhere. The free energy of the polymer particles is then $F_p = -k_B T \log Z^N$, or, assuming $V_{ex} \ll V$,

$$F_p = n k_B T V_{ex} \tag{1.24}$$

where $n = N/V$ is the concentration of polymer particles. Combining 1.22 and 1.24, we see that the polymer contribution to the free energy is

$$F_p = \mu \int dA + \bar{\kappa}_p \int K dA \tag{1.25}$$

where the effective interfacial energy per area is

$$\mu = n k_B T D \tag{1.26}$$

and the effective Gaussian curvature modulus is

$$\bar{\kappa}_p = \frac{1}{4} n k_B T D^2 d \tag{1.27}$$

The polymer contribution to the Gaussian curvature modulus is positive, in accord with the reduced excluded volume for negative Gaussian curvature. There is no polymer contribution the bending stiffness. Note, however, that if the polymers can only access one side of a membrane, e.g. if there are polymers inside but not out side a closed vesicle, then the depletion forces lead to a spontaneous curvature according

to 1.21.

There is also an intrinsic contribution to the Gaussian curvature modulus, $\bar{\kappa}_m$, which is always negative [28]. $\bar{\kappa}_m$ can be computed by analyzing the internal stresses as follows. Because it is fluid, we assume that the membrane middle surface membrane does not stretch when the membrane bends (the rods can adjust around each other to accommodate a change in curvature without changing their equilibrium spacing in the midplane). However, imposing any curvature onto a membrane will induce a strain that depends on z, the distance along the membrane normal away from the midplane. This areal strain of the surface at distance z is given by $\epsilon(z) = 2Hz + Kz^2$ [54]. The corresponding lateral membrane stress is $\sigma(z) = \sigma_0(z) + Y\epsilon(z)$, where $\sigma_0(z)$ is the membrane stress when it is flat and Y is the modulus of areal compression. Because the rods are uniform along their lengths, we take Y to be independent of z. The lateral stress is isotropic because the membrane is fluid. There is a compressive stress in the membrane even when it is flat because the polymer depletants squeeze the membrane [2]. The total volume excluded to the polymers for a flat membrane of area A is $V_{0,ex} = A(D+d)$, leading to a contribution to the free energy per area $\gamma = nk_BT(D+d)$, which can also be considered an entropic tension [42]. To balance this tension, the rods must experience a compressive stress $\sigma_0(Z) = -nk_BT(D+d)/D$. We write the free energy per unit mid-surface by integrating the stress with respect to the strain as $F_m = \int_{-D/2}^{D/2} dz \int_0^{\epsilon(z)} d\epsilon' \sigma(\epsilon') = \bar{\kappa}_m K$, where $\bar{\kappa}_m = \int_{-D/2}^{D/2} dz z^2 \sigma_0(z)$ [34, 62]. We thus conclude

$$\bar{\kappa}_m = -\frac{1}{12} nk_BT(D+d)D^2. \tag{1.28}$$

The net Gaussian curvature modulus is then

$$\bar{\kappa} = \bar{\kappa}_p + \bar{\kappa}_m \simeq \frac{1}{6} nk_BTD^2d. \tag{1.29}$$

If we use $n \simeq 40$ mg/mL, $D = 880$ nm, and $d = 30$ nm for Dextran with a molecular weight of 500,000 g/mol [57], we find that $\bar{\kappa} \sim 185\ k_B T$, which agrees with experimental measurements [28]. Note that our argument for the polymer contribution is similar to the model put forward to explain negative Gaussian curvature modulus for surfactant interfaces: for a saddle-splay surface with $H = 0$, there is less room for the surfactant chains, which therefore must stretch and incur a higher free energy [49].

1.3.3 Liquid crystalline energy

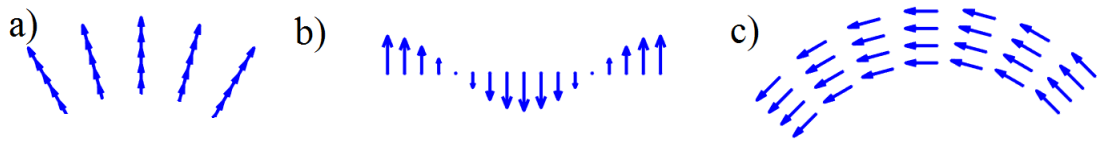

Figure 1.4: (a) Splay, (b) twist, and (c) bend deformations of a nematic liquid crystal, which increase the free energy of the system.

While the energy of membrane bending is described by the Canham-Helfrich functional, we must also account for the liquid crystalline degrees of freedom bestowed by the rod-like colloidal particles. If $\hat{n}$ is a unit vector that denotes the local rod orientation, then the Frank liquid crystal energy is

$$E_{LC} = \frac{1}{2}\int \left[K_1(\nabla \cdot \hat{n})^2 + K_2(\hat{n} \cdot \nabla \times \hat{n} + q)^2 + K_3(\hat{n} \times (\nabla \times n))^2 + \frac{C}{2}\sin^2\theta\right] dA \tag{1.30}$$

where θ is the angle between $\hat{n}$ and the surface normal, and K_1, K_2, and K_3 are the Frank elastic constants for the splay, twist, and bend, respectively [18]. If the liquid crystal is chiral (as in the case of a cholesteric), then a nonzero q represents the wavenumber of the preferred twist; note that this term, unlike the terms in the Canham-Helfrich energy, provides a way to energetically distinguish between two solutions that are "mirror images" of each other. The first three terms penalize

gradients in $\hat{n}$ (Fig. 1.4), while the second term expresses a preference of the rods to align normal to the surface. Typically K_1, K_2, and K_3 are all of the order $100k_BT$ for colloidal membranes [23] (in fact, it is common to employ the "one Frank constant approximation" $K_1 = K_2 = K_3 = K$ for isotropic materials), and C is of the order $100k_BT/\mu\text{m}^2$ [44]. The ratio of these parameters defines the previously mentioned twist penetration depth: $\lambda = \sqrt{K/C} \simeq 1\mu\text{m}$. Note also that E_{LC} must remain invariant under a $\hat{n} \to -\hat{n}$ transformation since the rods are symmetric.

1.3.4 Edge energy and effective geometric theory

Colloidal membranes are commonly found to form open surfaces with edges, and we must account for the energetic cost of having an interface. We denote the energy per unit length of edge as Γ, the line tension. For colloidal systems, Γ is a function of the temperature, chirality, and depletant concentration, and typically ranges from 100 to 1000 k_BT/μm [27, 38].

The minimal elastic energy describing colloidal membranes is the sum of the line tension energy, bending energy E_{CH}, and liquid crystal energy E_{LC}. Such an energy has been used to calculate the equilibrium width and pitch of infinitely long ribbons, as criterion for when force-free flat membrane disks undergo a transition to helicoidal ribbons [44]. (Note that it was necessary in this calculation to add a stability term quadratic in the Gaussian curvature to prevent the ribbons from twisting excessively.)

In general, calculating the full energy with Frank energy terms is cumbersome (see Appendix B for the case of an axisymmetric surface). Therefore, we propose some simplifications to the liquid crstalline energy from the previous section. In

colloidal membranes for which the twist penetration depth is small compared to the radius, it makes sense to treat the liquid crystal energy effectively by assuming the bend and twist are confined to the edge (Fig. 1.5); a closely related effective theory has been successfully used to calculate the scalloped shapes of colloidal membranes composed of a mixture of viruses of opposite handedness [28, 43]. More concretely, our assumption implies the simplifications

$$\frac{K_3}{2}\int_{\mathcal{M}}(\hat{n}\times(\nabla\times\hat{n}))^2 dV \simeq \frac{B}{2}\int_{\partial\mathcal{M}} k^2 ds, \tag{1.31}$$

$$\frac{K_2}{2}\int_{\mathcal{M}}(\hat{n}\cdot(\nabla\times\hat{n})-q)^2 dV \simeq \frac{B'}{2}\int_{\partial\mathcal{M}}(\tau_g-\tau_g^*)^2 ds, \text{ and} \tag{1.32}$$

$$\frac{K_1}{2}\int_{\mathcal{M}}(\nabla\cdot\hat{n})^2 dV \simeq 0, \tag{1.33}$$

for some appropriately defined constants B and B', where k is the curvature of the edge and τ_g is the geodesic torsion of the edge. Here, $\tau_g^* \simeq q$ is a preferred geodesic torsion for the twist. Note that since we are interested in the twist relative to the surface normal, we use the geodesic torsion instead of the usual torsion (also, the torsion is not defined for a straight line, while the geodesic torsion has the advantage of always being well-defined [22]). Eqn. 1.33 comes from the fact that splay is not typically observed in colloidal membrane systems; recent studies have demonstrated that $K_1 \gg K_2 \simeq K_3$ [67].

It is convenient to define a chirality modulus $c^* = -B'\tau_g$, so that the above Frank energy approximations, along with 1.19, yield the effective energy

$$E = \int_{\mathcal{M}}\left[\frac{\kappa}{2}(2H-c_0)^2+\bar{\kappa}K+\mu\right]dA + \int_{\partial\mathcal{M}}\left[\Gamma+\frac{B}{2}k^2+\frac{B'}{2}\tau_g^2+c^*\tau_g\right]ds, \tag{1.34}$$

which we henceforth refer to as the energy of our *minimal* or *effective model*. Note that this energy includes all of the geometric terms allowed by the symmetry of

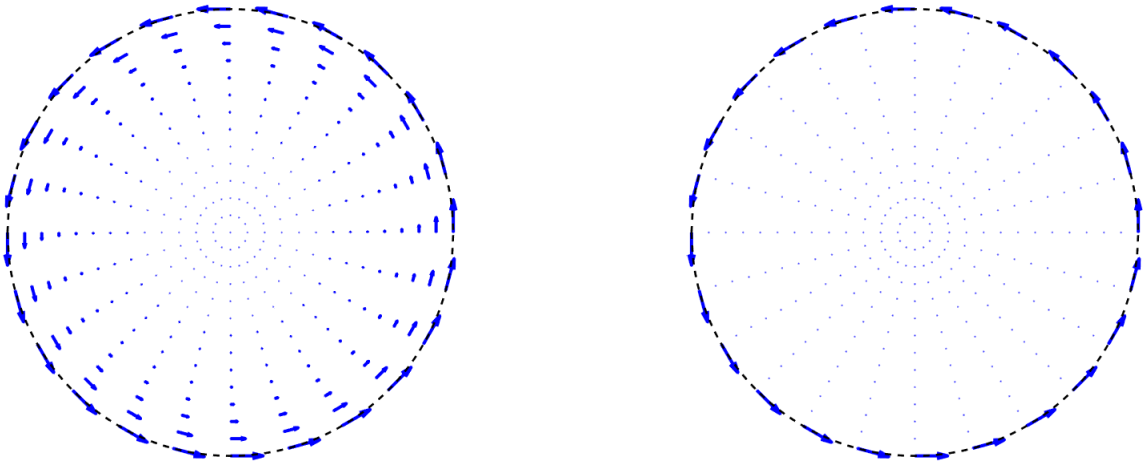

Figure 1.5: (Left) Top-down view of the director field $\hat{n}$ in a colloidal membrane. Most of the rods are pointing normal to the page, so they appear as dots. (Right) An approximation of the director field for small twist penetration depth λ, where the liquid crystalline energy is confined to the edge.

the problem, and can also be arrived at by listing all of these geometric terms, showing that this energy does not have to be derived from the more complete liquid crystal theory. From dimensional analysis, one can estimate that $B \simeq K_3\lambda$ and $c^* \simeq K_2\lambda q$, where λ is the twist penetration depth. If we make the approximation $K_2 \simeq K_3$, then $B \simeq 100\ k_BT\mu$m. From this, it is convenient to assume $B \simeq B'$ from dimensional analysis to conclude $c^* \simeq 100k_BT$, although the precise value of the chirality modulus will depend on temperature [23, 38]. In the chapters that follow, we apply the energy 1.34 to various colloidal membrane systems and model their shapes and phase transitions.

Chapter Two

Chiral Edge Fluctuations

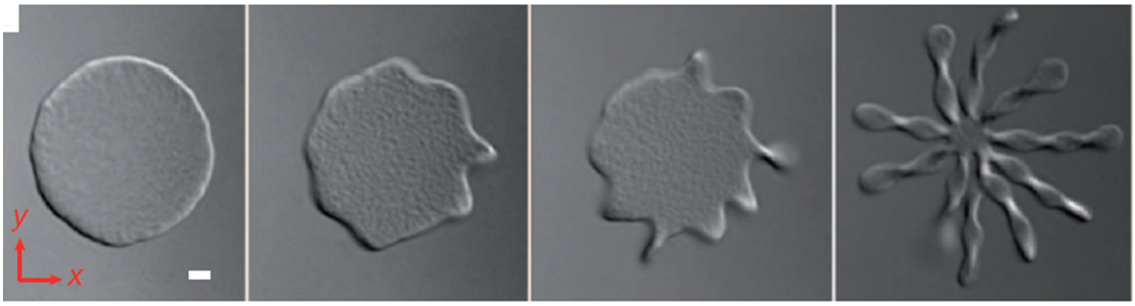

Figure 2.1: A temperature quench reduces the line tension, inducing a transition of the 2D membrane into 1D twisted ribbons. Scale bar = 2μm

2.1 Introduction

To study the unique shapes that colloidal membranes make, we developed an effective theory based on the Canham-Helfrich membrane bending energy (a function of mean and Gaussian curvatures) that also accounts for the finer liquid crystalline degrees of freedom through geometric properties of the surface boundary such as length, curvature, and geodesic torsion (Chapter 1). This effective model is most valid when the twist penetration depth of the membrane is much smaller than the radius. When chiral disk-shaped colloidal membranes are cooled from $\sim$60^{o}C to $\sim$20^{o}C, they phase transition into star-like twisted ribbons, as in Fig. 2.1. This transition manifests itself in the form of a prominent peak in the edge's fluctuation spectrum. We use stability analysis and our effective theory to derive expressions for the fluctuation spectrum near the onset of this transition. Our theory quantitatively captures the experimentally observed peak and demonstrates the importance of chirality and positive Gaussian curvature modulus in coupling in- and out-of-plane fluctuations to produce twisted shapes.

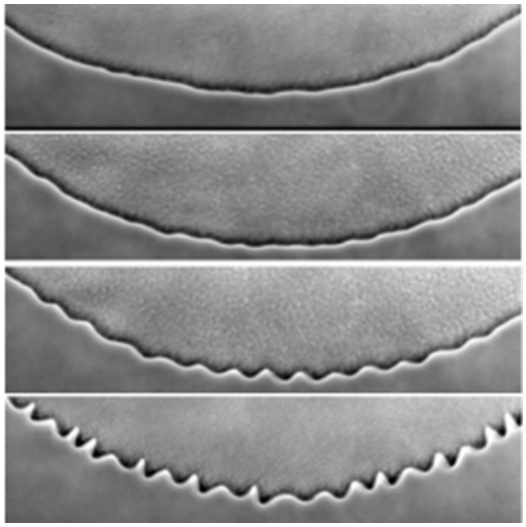

Figure 2.2: Edge of a fluctuating membrane at 60^oC, 50^oC, 40^oC, and 24^oC, showing enhancement of fluctuations due to chirality as the membrane is cooled. The membrane radius is approximately 10 μm [27].

2.2 Description of experiments

Experiments were performed by Mark Zakhary, as part of the research group of Zvonimir Dogic.

For these experiments, colloidal membranes were assembled by mixing a dilute isotropic suspension of monodisperse rod-like *fd-wt* viruses with a non-adsorbing polymer, Dextran (M.W. 500,000, 37 mg/ml) [6]. The *fd-wt* filaments are 0.88 μm long and have a diameter of $\approx$ 6 nm. The rods are parallel to the surface normal and to each other in the membrane interior, but they twist at the edge to minimize the interfacial area between the rods and the enveloping polymer depletant [7, 42]. Increasing the rod chirality raises the free energy of the interior untwisted rods and lowers the free energy of the twisted rods near the edge, leading to chiral control of edge line tension [27]. Chirality of *fd-wt* increases with decreasing temperature [23], enabling *in situ* control of the edge tension. With decreasing temperature the edge tension becomes sufficiently low that a 2D membrane becomes unstable and under-

goes a transition into 1D twisted ribbons [27] (Fig. 2.1).

Following previously published methods [70], we measured the in-plane fluctuation spectrum of an exposed colloidal membrane edge. The edge fluctuations were quantified over a range of temperatures (Fig. 2.2). For all conditions, the curves tend to a constant value at small wavenumber q and fall off as $1/q^2$ at large wavenumber, as in the previous measurements. However, for strongly chiral systems at lower temperatures, a peak develops around $q = 1\,\mu\mathrm{m}^{-1}$. We note that the measured fluctuation spectrum depends on the purity of the virus preparation as well as the depleting polymer Dextran. Certain virus preparations do not exhibit the membrane-to-ribbon transition. These samples also do not have a fluctuation spectrum with a well-defined peak. The exact nature of the contaminants in these samples has not been determined. Previous work has demonstrated that even a single actin filament exhibits a strong tendency to dissolve at the edge, and can suppress the membrane-to-ribbon transition [70]. In the remainder of this work we restrict our analysis to only those sample preparations that exhibited a well-defined ribbon-to-membrane transition and thus the anomalous peak.

2.3 Stability criteria for a flat membrane with edge

The in-plane edge fluctuations in the high-temperature achiral limit are described by a simple model, which approximates a flat, circular membrane as a semi-infinite membrane with an infinite straight edge [27]. For in-plane fluctuations, the effective energy of the edge is given by

$$E_1 = \int \mathrm{d}s \left[\Gamma + \frac{B}{2} k^2 \right], \tag{2.1}$$

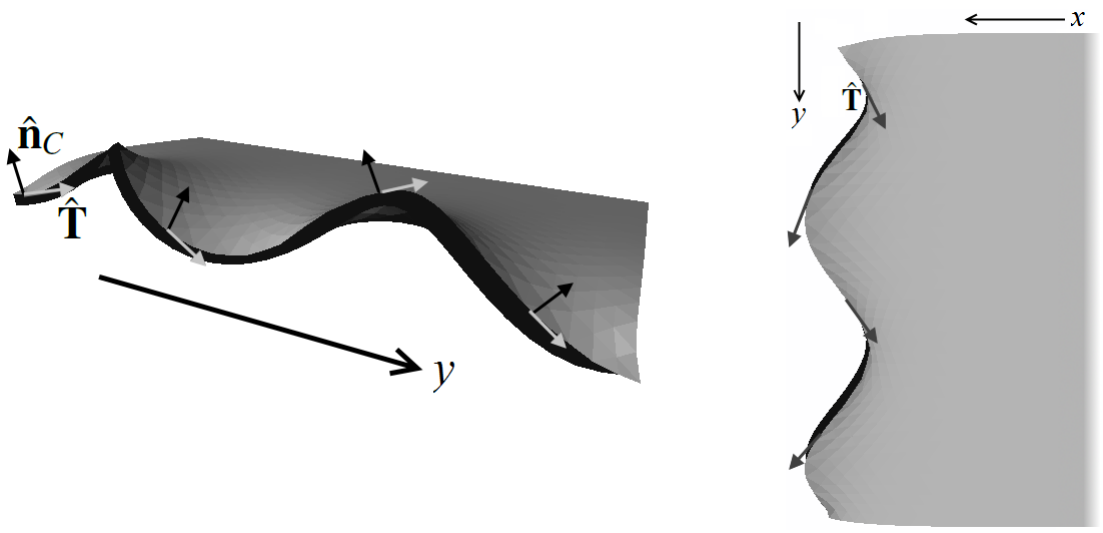

Figure 2.3: (Left) Semi-infinite surface with a helix-like boundary. (Right) Same shape viewed from above, looking down the z-axis at the xy plane

where s is the edge arclength, Γ is the line tension, B is the bending stiffness, and k is the curvature. For a flat membrane lying in the x-y plane, we describe the path of the edge by $(u(y), y, 0)$, where $u(y)$ measures the local deviation of the edge from being perfectly straight. Expanding the energy (2.1) to second order in u and applying the equipartition theorem yields

$$\langle u_q u_{-q} \rangle = \frac{k_{\mathrm{B}} T}{B q^4 + \Gamma q^2}, \tag{2.2}$$

where u_q is the Fourier amplitude defined by $u(y) = (1/\sqrt{L}) \sum_q u_q \exp \mathrm{i} q y$, with the sum running over negative and positive values of q, and we have enforced periodic boundary conditions with period L. Fitting the high-temperature spectrum of achiral rods to Eq. (2.2) yields Γ and B [27].

To study the stability of a flat membrane and the out-of-plane fluctuations of its edge, we calculate the energy of a semi-infinite membrane with a rippled edge, working to second order in the deformation. The membrane is initially flat with mid-surface at the $z = 0$ plane and occupying $x < 0$. The y-axis is the initially

straight edge. We perturb the surface by deforming the edge so that the position of points on the membrane above the coordinates in the plane (x, y) are given by $\mathbf{R}(x, y) = (x, y, \zeta(x, y))$, and with the edge given by $\mathbf{R}_C(y) = (u(y), y, v(y))$, which implies the boundary condition $\zeta(u(y), y) = v(y)$. If $u(y)$ and $v(y)$ are sinusoidal and out of phase, the edge will have a helical nature as illustrated in Fig. 2.3. Care must be taken in calculating the edge quantities since we must expand both the quantities themselves and their arguments. For example, to find the geodesic torsion at the edge we expand the argument of the normal at the edge, $\mathbf{n}_C(u(y), y) \approx \mathbf{n}(0, y) + u\partial\mathbf{n}_C/\partial x|_{x=0}$.

Expanding the energy to second order, we find the total energy $E = E_1 + E_2 + E^*$,

$$\begin{aligned} E &= \int \mathrm{d}x\mathrm{d}y \left\{ \frac{\kappa}{2}(\nabla^2\zeta)^2 + \bar{\kappa}\left[\frac{\partial^2\zeta}{\partial x^2}\frac{\partial^2\zeta}{\partial y^2} - \left(\frac{\partial^2\zeta}{\partial x \partial y}\right)^2 \right] \right\} \\ &+ \int \mathrm{d}y \left[\frac{\Gamma}{2}\left(u'^2 + v'^2\right) + \frac{B}{2}\left(u''^2 + v''^2\right) \right] \\ &+ \int \mathrm{d}y \left[\frac{B}{2}\left(\frac{\partial^2\zeta}{\partial x \partial y}\right)^2_{x=0} + c^* u' v'' \right], \end{aligned} \tag{2.3}$$

where the prime denotes the derivative with respect to y, e.g. $u' = \mathrm{d}u/\mathrm{d}y$. To first order the Euler-Lagrange equation for the energy (2.3) is $(\nabla^2)^2\zeta = 0$. Since the horizontal and vertical positions of the edge are prescribed, we do not enforce the force boundary conditions at the edge. The condition of zero bending moment at the boundary to first order [46] is $\kappa\nabla^2\zeta + \bar{\kappa}\partial^2\zeta/\partial y^2 = 0$ at $x = 0$. The solution to the Euler-Lagrange equations that satisfies this boundary condition and $\zeta(u(y), y) = v(y)$ is

$$\zeta(x, y) = \frac{1}{\sqrt{L}} \sum_q v_q \left(1 + \frac{\bar{\kappa}}{2\kappa}|q|x\right) \exp\left(|q|x + \mathrm{i}qy\right). \tag{2.4}$$

Note that when $\kappa \gg \bar{\kappa}$, the surface becomes a minimal surface. To keep the area fixed, the whole surface must shift in the negative x-direction; however, this shift is

second order in the v_q and does not affect the energy to leading order.

Inserting the Fourier expansions of $\zeta(x,y)$, $u(y)$, and $v(y)$ into the total energy yields

$$E = \sum_q \left[\left(-\bar{\kappa}|q|^3 \frac{4\kappa+\bar{\kappa}}{4\kappa} + \frac{\Gamma}{2}q^2 + \frac{B}{2}\left(\frac{2\kappa+\bar{\kappa}}{2\kappa}\right)^2 q^4 \right) |v_q|^2 + \left(\frac{\Gamma}{2}q^2 + \frac{B}{2}q^4 \right) |u_q|^2 - \frac{\mathrm{i}}{2}c^* q^3 \left(u_q v_{-q} - u_{-q} v_q\right) \right]. \tag{2.5}$$

Using the expression for the energy (2.5) we can study the stability of a flat semi-infinite membrane. We first consider the achiral case, $c^* = 0$, which applies at high temperatures ($T \gtrsim 60^\circ$ C). The horizontal and vertical fluctuations of the edge are decoupled, and ripples u_q in the plane of the membrane always increase the energy. However, when the Gaussian curvature modulus is larger than $\bar{\kappa}_\mathrm{c}$, where $\bar{\kappa}_\mathrm{c}$ solves $\bar{\kappa}_\mathrm{c}(4\kappa+\bar{\kappa}_\mathrm{c}) = \sqrt{\Gamma B}\,(4\kappa+2\bar{\kappa}_\mathrm{c})$, then it is energetically favorable for ripples v_q in the vertical (positive z-) direction to form. Using the typical values for B and κ quoted above, and the value $\Gamma \approx 300\,k_\mathrm{B}T$ we find from fitting the fluctuation spectrum at high temperature (see below and Fig. 2.7), we estimate $\bar{\kappa}_\mathrm{c} \approx 50\,k_\mathrm{B}T$. The wavenumber of the ripple that forms just at the critical condition $\bar{\kappa} = \bar{\kappa}_\mathrm{c}$ is $q_\mathrm{c} = \sqrt{\Gamma/B}/(1+\bar{\kappa}_\mathrm{c}/2\kappa) \approx 1\,\mu\mathrm{m}^{-1}$.

In the chiral case, we study the stability of the flat membrane with an edge by writing $E = \sum_q (u_q, v_q) M_q (u_{-q}, v_{-q})^\mathrm{T}/2$ and diagonalizing M_q to find its eigenvalues $\sigma_\pm = \Gamma q^2 + Bq^4[1+(1+\bar{\kappa}/2\kappa)^2]/2 - |q|^3[\bar{\kappa}\,(1+\bar{\kappa}/4\kappa) \mp \sqrt{c^{*2} + \bar{\kappa}^2\,(1+\bar{\kappa}/4\kappa)^2\,(B|q|/2\kappa - 1)^2}]$. In this case, either chirality or the Gaussian curvature modulus can drive an instability. The condition for a rippled edge is $\sigma_- \geq 0$, and the critical values for the Gaussian modulus $\bar{\kappa}_\mathrm{c}$ and marginally unstable wavenumber q_c are determined by the conditions $\sigma_- = 0$ and $\partial\sigma_-/\partial q = 0$. These equations lead to complicated expressions

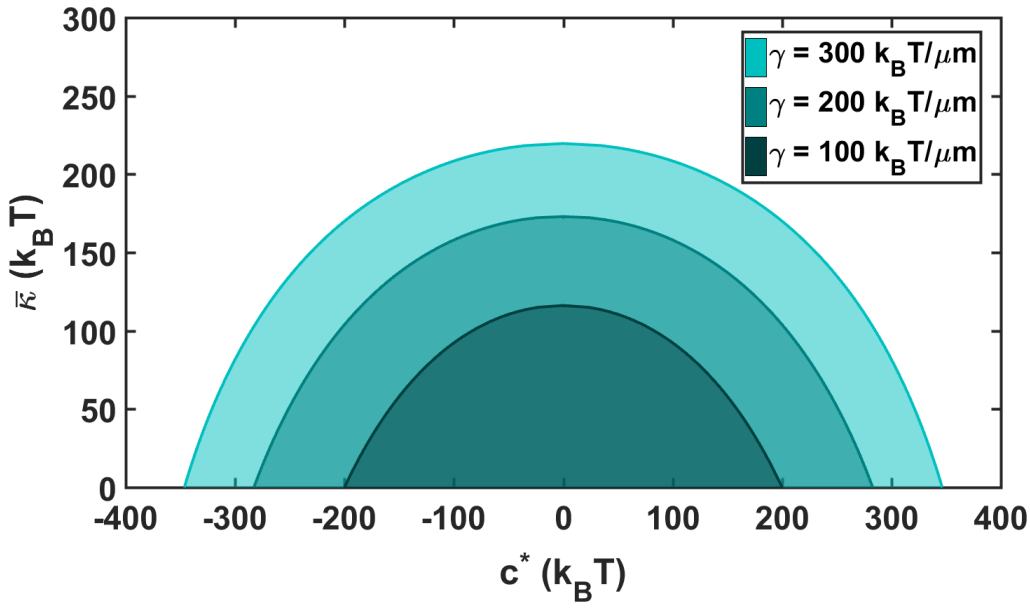

Figure 2.4: Phase diagram for flat and rippled edges of chiral membranes as a function of Gaussian curvature modulus $\bar{\kappa}$ and chiral modulus c^* for various values of line tension Γ, $B = 100\,k_{\mathrm{B}}T\mu$m, and $\kappa = 150\,k_{\mathrm{B}}T$. The flat edge is stable in the shaded area.

for q_{c} and the critical values of $\bar{\kappa}$ and c^*, which are plotted in Figure 2.4. However, the expressions simplify in the limit $B \gg B'$, where the critical wavenumber is $q_{\mathrm{c}} = \sqrt{\Gamma/B}$, and the critical values of $\bar{\kappa}$ and c^* satisfy

$$\bar{\kappa}\left(\frac{4\kappa+\bar{\kappa}}{4\kappa}\right) + \sqrt{c^{*2} + \bar{\kappa}^2\left(\frac{4\kappa+\bar{\kappa}}{4\kappa}\right)^2} = 2\sqrt{\Gamma B}. \tag{2.6}$$

Note that the factor of ic^* in the off-diagonal components of M_q leads to a phase difference between the x- and z- components of the eigenvectors of M_q, and thus a preferred handedness to the edge depending on the sign of c^*.

2.4 Stability criteria for a disk

Although we approximated the disk as a semi-infinite plane in the previous section, this is not strictly necessary. Here we outline the analysis assuming without making

this assumption and show that we recover the same conditions for stability in the limit of large radius.

Consider a disk with a helical ripple, so that the curve is described by $\underline{r}(\theta) = (a\cos\theta, a\sin\theta, 0) + h(\cos m\theta\cos\theta, \cos m\theta\sin\theta, \sin m\theta)$, where m is an integer. The height of the fluctuation h is assumed to be much smaller than the disk radius a. As above, in order to keep the area fixed, the projection of the edge moves inward by some amount δa, but the effect of μ is to exactly cancel this change in area, so we need not compute it.

We proceed to calculate

$$\Gamma \int ds = 2\pi\Gamma a + \Gamma\pi\frac{h^2m^2}{a} \tag{2.7}$$

$$c^* \int \tau_g ds = c^*\pi\frac{h^2m(m^2-1)}{a^2} \tag{2.8}$$

$$\frac{B}{2}\int k^2 ds = \frac{B\pi}{a} + \frac{B}{2}\frac{1-4m^2+2m^4}{a^3}\pi h^2 \tag{2.9}$$

(here, we are assuming $B' \ll B$).

Now we consider the surface terms from the Canham-Helfrich energy. To first order, the shape equation is

$$\Delta^2\zeta - \frac{\mu}{\kappa}\Delta\zeta = 0 \tag{2.10}$$

and the solution is

$$\zeta(r,\theta) = [c_0 r^m + c_1 J_m(r/\lambda)]\sin m\theta \tag{2.11}$$

where $\lambda = \sqrt{\kappa/\mu}$. The constants c_0 and c_1 are obtained from the boundary conditions $\zeta(a,\theta) = h\sin m\theta$ and $\kappa(2H) + \bar{\kappa}k_n = 0$ (we have made the approximation that

the projected area is a circle). From this, we obtain the system of equations

$$\begin{cases} c_0 a^m + c_1 J_m(a/\lambda) = h \\ -\kappa \frac{c_1}{\lambda^2} J_m(a/\lambda) + \frac{\bar{\kappa}}{a}\left[c_0 m a^{m-1} + \frac{c_1}{\lambda} J'_m(a/\lambda)\right] - \bar{\kappa}\frac{m^2}{a^2} h = 0 \end{cases} \tag{2.12}$$

whose solution is

$$c_0 = \frac{h}{a^m} \frac{a\bar{\kappa}\lambda J_{m-1}(a/\lambda) - (a^2\kappa + \bar{\kappa}\lambda^2 m(m+1)) J_m(a/\lambda)}{a\bar{\kappa}\lambda J_{m-1}(a/\lambda) - (a^2\kappa + 2\bar{\kappa}m\lambda^2) J_m(a/\lambda)} \tag{2.13}$$

$$c_1 = \frac{h\bar{\kappa}m(m-1)\lambda^2}{a\bar{\kappa}\lambda J_{m-1}(a/\lambda) - (a^2\kappa + 2\bar{\kappa}m\lambda^2) J_m(a/\lambda)} \tag{2.14}$$

Note that when $m = 1$, $c_0 = h/a^m$ and $c_1 = 0$ so that $\zeta = \frac{hr}{a}\sin\theta$, which is a rigid rotation. The change in bending energy to highest order is thus the sum of

$$\frac{\kappa}{2}\int dA(2H)^2 = \kappa \frac{c_1^2}{\lambda^4}\frac{\pi}{4} a^2 \left[J_m^2(a/\lambda) - J_{m-1}(a/\lambda) J_{m+1}(a/\lambda)\right] \tag{2.15}$$

$$\bar{\kappa}\int dAK = -2\pi a\bar{\kappa}h^2 \frac{2\lambda^2(m-1)m^2 - a\frac{c_1}{h}J_{m+1}\left(\frac{a}{\lambda}\right)\left(a\frac{c_1}{h}J_{m+1}\left(\frac{a}{\lambda}\right) + 2\lambda m(m-1)\right)}{4a^3\lambda^2} \tag{2.16}$$

The total change in energy for the chiral perturbation compared to the flat disk is the complicated expression

$$\begin{aligned} \delta E = \pi h^2 \Bigg(& \Gamma\frac{m^2}{a} + \frac{B}{2a^3}(1 - 4m^2 + 2m^4) + \frac{c^*}{a^2} m(m^2-1) \\ & + \frac{\kappa c_1^2 a^2}{4h^2\lambda^4}\left[J_m^2\left(\frac{a}{\lambda}\right) - J_{m-1}\left(\frac{a}{\lambda}\right) J_{m+1}\left(\frac{a}{\lambda}\right)\right] \\ & - \frac{\bar{\kappa}}{2a^2\lambda^2}\left[2\lambda^2(m-1)m^2 - a\frac{c_1}{h}J_{m+1}\left(\frac{a}{\lambda}\right)\left(a\frac{c_1}{h}J_{m+1}\left(\frac{a}{\lambda}\right) + 2\lambda m(m-1)\right)\right]\Bigg) \end{aligned} \tag{2.17}$$

Fig. 2.5 shows the phase boundaries between the flat and rippled states for membranes of radius $a = 5\mu$m and $a = 50\mu$m. The agreement between the disk and

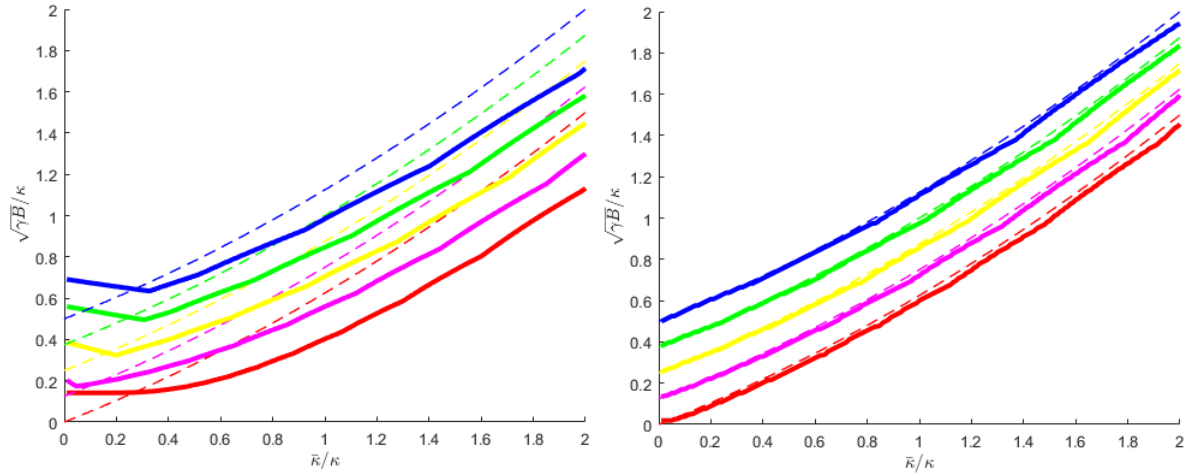

Figure 2.5: Phase boundaries for a membrane of radius $a = 5\mu$m (left) and $a = 50\mu$m (right). Different colors indicate different values of $|c^*|/\kappa$. From lowest curve to highest: 0 (red), 0.25 (magenta), 0.5 (yellow), 0.75 (green), 1 (blue). Dashed line indicates phase boundary for half-plane; solid line indicates phase boundary for disk. For large radius we recover the stability condition for a chiral half-plane (Eqn. 2.6) as indicated by the overlap of the solid and dashed lines. We assume $B' \ll B$.

sem-infinite plane cases converges quickly, so the approximation is justified (and welcome, considering the complexity of Eqn. 2.17).

2.5 Expressions for the fluctuation spectrum

The energy (2.5) along with the equipartition theorem yields the power spectrum for in-plane and out-of-plane edge fluctuations, which is valid for stable flat states:

$$\langle u_q u_{-q} \rangle = \frac{k_B T}{Bq^4 + \Gamma q^2 - c^{*2} q^4/\Delta(q)} \tag{2.18}$$

$$\langle v_q v_{-q} \rangle = \frac{k_B T}{\Delta(q) - c^{*2} q^4/(Bq^2 + \Gamma)}, \tag{2.19}$$

where $\Delta(q) = Bq^4\{1 + [1 + \bar{\kappa}/(2\kappa)]^2\} + \Gamma q^2 - 2\bar{\kappa}|q|^3[1 + \bar{\kappa}/(4\kappa)]$.

Note that c^*, κ, and $\bar{\kappa}$ only affect the fluctuations for intermediate q; the large and

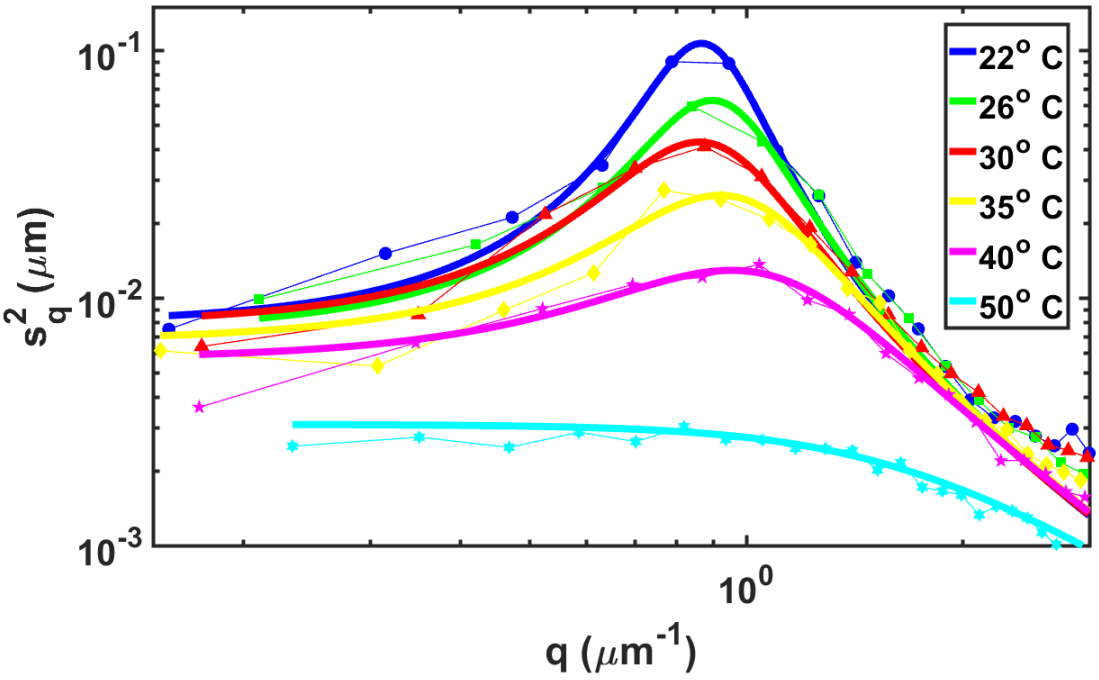

Figure 2.6: (a) Normalized power spectrum $s_q^2 \equiv q^2\langle u_q u_{-q}\rangle$ in which c^* (in units of k_BT) and Γ (in units of k_BT/μm) are fit to the data, with $\kappa/\bar{\kappa} \to \infty$, $B = 100\,k_BT\mu$m, and $\bar{\kappa} = 50\,k_BT$. The value of B used was found by fitting the $T = 60°$ C data to the achiral formula, Eq. (2.2)

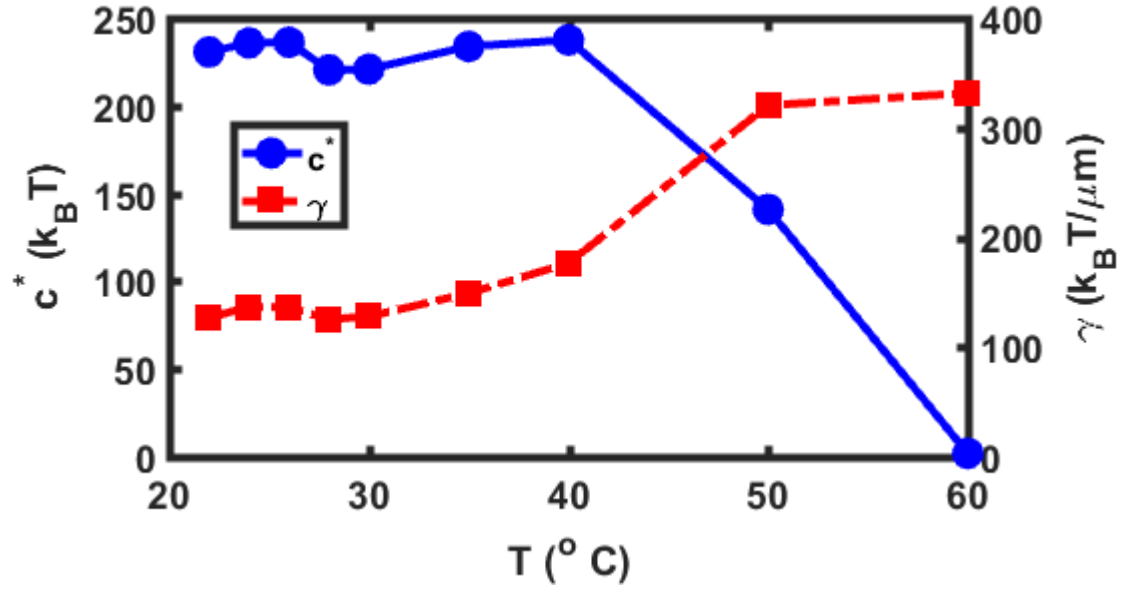

Figure 2.7: Values of c^* obtained from fitting (left vertical axis), and values of Γ obtained from fitting (right vertical axis)

small q behavior is controlled by the bending stiffness and line tension, respectively, just as in the case of an achiral membrane. Note also that the out-of-plane fluctuations of the edge of an achiral membrane have a distinctly different q-dependence than the in-plane fluctuations of Eq. (2.2): $\langle v_q v_{-q} \rangle = k_{\mathrm{B}}T/\Delta(q)$ when $c^* = 0$.

As the temperature is lowered, the value of Γ decreases while chirality and thus c^* increases. The system therefore comes closer to fulfilling the condition (2.6) for ripples to form, leading to a peak near q_{c}. Figure 2.6 shows fits of the theoretical expression (2.18) for $s_q^2 \equiv q^2 \langle u_q u_{-q} \rangle$ assuming $\kappa = 150\, k_{\mathrm{B}}T$, $B = 100\, k_{\mathrm{B}}T\, \mu$m, and $\bar{\kappa} = 50\, k_{\mathrm{B}}T$, along with the values of Γ and c^* obtained from fitting each curve. The value of B used was found by fitting the $T = 60^\circ$ C data to the achiral formula, Eq. (2.2). Because B does not change appreciably with T, all curves collapse onto a single line in the large q limit. Similarly, $\bar{\kappa}$ is not expected to depend significantly on T and was fixed for fitting. Because both $\bar{\kappa}$ and c^* control the size of the peak, fixing $\bar{\kappa}$ also allows the effect of c^* to be assessed more accurately. The magnitude of the $\bar{\kappa}$ used in our fits is smaller than but still comparable in magnitude with the recent experimental measurements and theoretical estimates that yield $\bar{\kappa} \approx 200\, k_{\mathrm{B}}T$ [28].

The values of Γ and c^* from the fitting have the expected order of magnitude and obey the expected trend of Γ increasing and c^* decreasing to zero as the temperature increases (Fig. 2.7). Although the fits capture the shape of the peak well, there is some discrepancy with the experimental data at the smallest measured values of q. There are two main reasons for this discrepancy. First, the characteristic widths of the peaks are fairly large, and there are not enough data points taken at small enough q to escape the influence of the peak. Second, when q decreases, the fluctuation relaxation time increases rapidly. The longer relaxation time leads to poor statistics, since it reduces the number of configurations over which the data can be averaged. Consequently, the fits tend to underestimate Γ when the temperature

is low.

To conclude, we have measured the small-amplitude fluctuations of the edge of a colloidal membrane, and found that as the chirality increases, a peak forms at a characteristic wavelength. Our effective geometric theory captures the important features of the measurement such as the formation of the peak, and shows how the Gaussian curvature modulus affects the fluctuations when chirality couples the undulations of the edge in and out of the plane of the membrane. We have also calculated the power spectrum for out-of-plane fluctuations of the edge, which would be especially interesting to measure in the achiral case, as it offers another method of estimating the Gaussian curvature modulus $\bar{\kappa}$.

Chapter Three

Axisymmetric Membranes

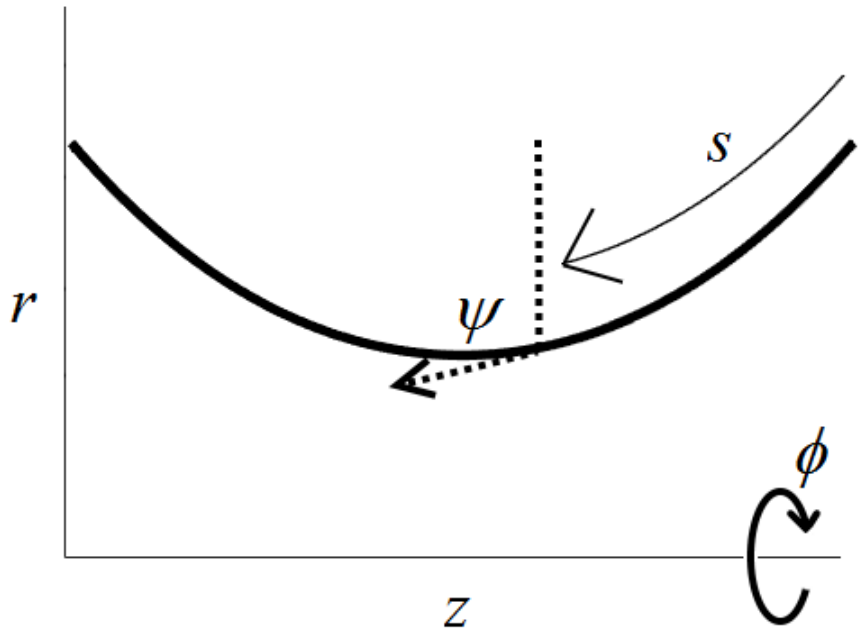

Figure 3.1: Parameterization of an axisymmetric shape. The z-axis is the axis of revolution, ϕ is the angle of revolution, and r is the radial coordinate. Arclength is denoted by s while ψ denotes the angle between the tangent vector and the r axis. Note that $s = 0$ corresponds the the rightmost endpoint.

3.1 Introduction

The shape equation (Eqn. 1.20), a nonlinear partial differential equation, is notoriously difficult to solve for a general system. However, by assuming axisymmetry and our effective model that accounts for the elastic energy via edge quantities (Eqn. 1.34), we can simplify the shape equation into a system of ordinary differential equations that is easier to analyze. In this chapter, we detail various axisymmetric colloidal membrane systems and the successes and shortcomings of our effective theory in modeling them.

3.2 Arclength parameterization

To analyze axisymmetric membrane problems, we first express the effective energy 1.34 in a convenient coordinate system [56, 39]. Let the surface be given in $\mathbb{R}^3$ by $\underline{X}(s,\phi) = (r(s)\cos\phi, r(s)\sin\phi, z(s))$, where s is the arclength starting at the rightmost point and ending at $z = 0$. It is convenient to write the tangent vector along a meridian as $\hat{T}(s) = (r_s, z_s) = (\cos\psi, -\sin\psi)$, where $\psi(s)$ is the angle between $\hat{T}$ and the vertical axis (Fig. 3.1). Notice that this implies the constraint

$$r_s^2 + z_s^2 = 1. \tag{3.1}$$

From this, one can calculate that the metric tensor is

$$g_{ij} = \underline{X}_i \cdot \underline{X}_j = \begin{bmatrix} 1 & 0 \\ 0 & r^2 \end{bmatrix}, \tag{3.2}$$

the unit normal of the surface is

$$\hat{N} = (\sin\psi\cos\phi, \sin\psi\cos\phi, \cos\psi), \tag{3.3}$$

and the second fundamental form is

$$b_{ij} = \hat{N} \cdot \underline{X}_{ij} = \begin{bmatrix} -\psi_s & 0 \\ 0 & -r\sin\psi \end{bmatrix}. \tag{3.4}$$

Together, these imply that the principal curvatures are ψ_s and $\sin\psi/r$.

Since the boundaries of an open axismmetric surface are just a pair of circles, the geodesic torsion at the edge vanishes, and chirality is not expected to play a role in

determining axisymmetric surfaces using the effective energy 1.34. Meanwhile, the geodesic and normal curvatures at the edge reduce to

$$k_g = \frac{\cos\psi}{r} \text{ and } k_n = -\frac{\sin\psi}{r}. \tag{3.5}$$

In Appendix B, we derive the Euler-Lagrange ordinary differential equations and no force/torque boundary conditions associated with this coordinate system for both the full liquid crystal energy and the minimal model. These equations are then solved numerically using MATLAB's `bvp4c` routine (a boundary value problem solver) for a variety of systems, which are detailed below.

3.3 Coalesence of saddles into unduloids

In experiments where colloidal membranes were doped with shorter rods of the same width but roughly 75% the length of the usual fd viruses, the membranes were observed to form metastable saddle shapes (Fig. 3.2). For low enough long rod fractions, when two of these saddles come into contact, the membrane takes on an axisymmetric shape with two holes. We estimate the resulting spontaneous curvature and argue that the axisymmetric surfaces formed are the classic unduloids often studied in the theory of droplets [45, 32, 25]. We then use our minimal model and full liquid crystal energy models to confirm their shape.

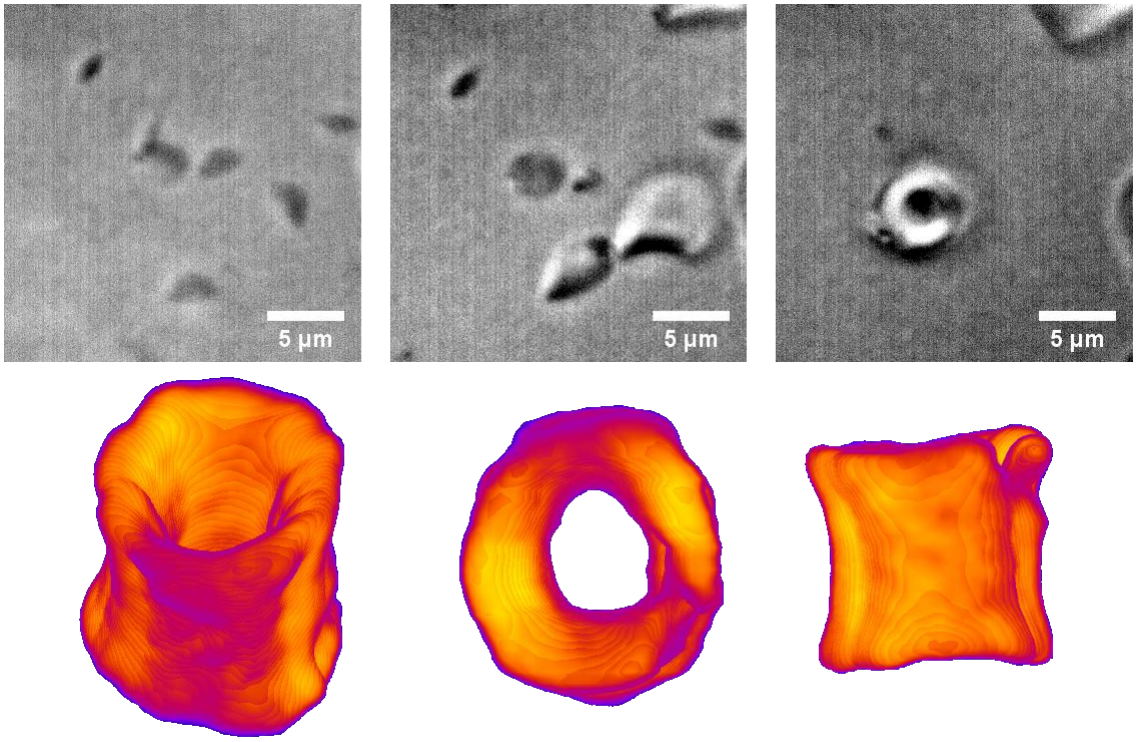

Figure 3.2: (Top) Experimental formation of an unduloid from a pair of saddle-shaped membranes doped with short rods. Left, center, and right images were taken at approximately 1 minute, 5 minutes, and 10 minutes into the experiment, respectively. (Bottom) Computer generated render of the final axisymmetric equilibrium surface.

3.3.1 Experimental methods

Experiments were performed by Andrew Balchunas as part of the research lab of Zvonimir Dogic.

The two types of bacteriophage virus used in this experiment were M13-wt (wild type) and its mutant M13-KO7, which is identical in all aspects except contour length. M13-wt has a contour length of 880 nm, while M13-KO7 has a contour length of 1200nm, approximately 37% longer than its unmutated relative. In order to form the membranes, dextran (molecular weight 500,000) was used a a polymer depletant. Uniformly mixed membranes are observed at low osmotic pressure, while phase separation between short and long rods is observed at high osmotic pressure (Fig. 3.3). The osmotic pressure in the system is related to the dextran concentration. An "unduloid" phase arises from mixing M13-wt and M13-KO7 at specific stoichiometric ratios and intermediate osmotic pressures. All samples were prepared in Tris-HCl buffer (20 mM, pH 8.0) with 100 mM NaCl added to screen electrostatic repulsion between the viruses. The final virus concentration was at 0.5 mg mL^{-1} regardless of the overall number ratio.

Line tension data was acquired using darkfield microscopy of the edge fluctuations of the membrane. The line tension of the membranes in this system was measured to be $570 k_B T/\mu$m. The edge bending stiffness has been previously measured to be around $100 k_B T \mu$m and is the same for both species of virus, as they share the same cholesteric pitch [30].

The total area of the membranes that coalesced was measured to be approximately $40 \mu\mathrm{m}^2$. The modulus κ has been reported to be roughly $1.5 \times 10^5 k_B T$ [4], while the Gaussian curvature modulus has been theoretically estimated at $\bar{\kappa} \simeq$

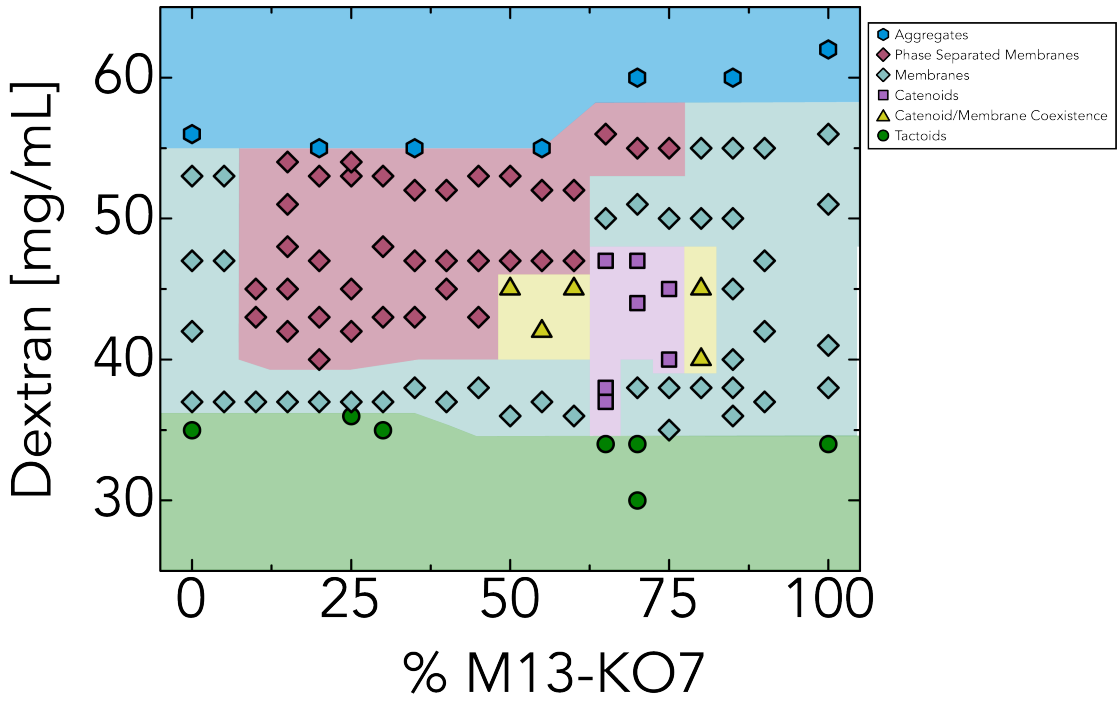

Figure 3.3: Experimental phase diagram for membranes that have been doped with shorter rods. The horizontal axis is long rod fraction and the vertical axis is depletant concentration. Unduloids are observed to start forming around 75% long rod fraction. Below 50% long rod fraction, the short and long rods prefer to phase separated membranes.

$200k_BT$ [28].

3.3.2 Spontaneous curvature as a function of long rod fraction

We use a simple geometric argument to estimate the value of c_0 in these unduloids. Suppose the membrane consists of N_l long rods and N_s short rods. Recall that the long rods have length $L = 1200$ nm and a radius of roughly $d = 3$ nm (although d does not explicitly enter our model).

For simplicity, assume that the bilayer is wrapped into a spherical vesicle so that the inner radius is R_i and the outer radius is R_o, as in Fig. 3.4; it is thought that the

short rods have this type of configuration by comparison with observations of similar systems [4]. On the outer surface, if the rods are all normal to the surface, we have $N_l + N_s$ circles packed onto the surface of a sphere. However, on the inner surface there are only N_l circles. If we denote the packing fractions of the inner and outer surfaces ϕ_i and ϕ_o, respectively, the surface areas of the outer and inner spheres are

$$A_o = \frac{\pi d^2 (N_l + N_s)}{4\phi_o} \text{ and } A_i = \frac{\pi d^2 N_l}{4\phi_i} \tag{3.6}$$

Furthermore, we also know the separation between the radii is $R_o - R_i = L$, so putting these together gives

$$R_i = \frac{L}{\sqrt{\frac{N_l+N_s}{N_l}\frac{\phi_i}{\phi_o}} - 1} \tag{3.7}$$

In the case where $\phi_i \simeq \phi_o$, this expression simplifies further to

$$R_i = \frac{L}{\sqrt{1/\phi_L} - 1} \tag{3.8}$$

where ϕ_L is the long rod fraction. The spontaneous curvature can then be estimated as $c_0 = 2H \simeq 2/R_i$. In the case where the membrane contains no short rods, $\phi_L = 1$, and $R_i \to \infty$, i.e. the membane has no spontaneous curvature. For 65% long rod fraction where unduloids are observed to form, this yields a spontaneous curvature of $c_0 \simeq 0.4\ \mu\text{m}^{-1}$.

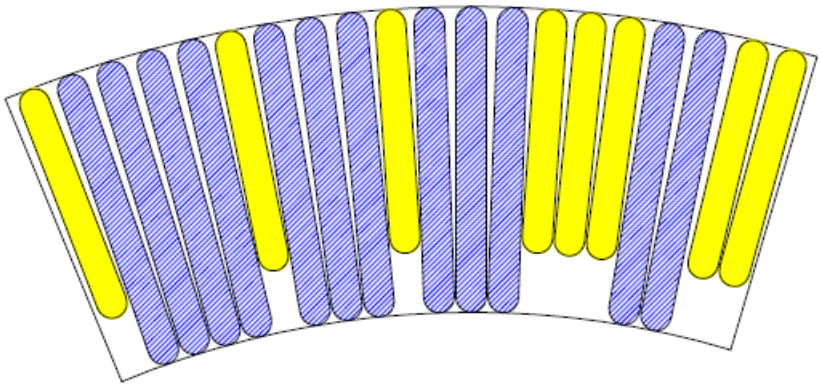

Figure 3.4: Induction of spontaneous curvature by doping a membrane composed of longer rods (blue) with shorter rods (yellow). The upper surface is an arc with radius R_o and the bottom surface is an arc with radius R_i. The distance between the surfaces is the length of one long rod, L.

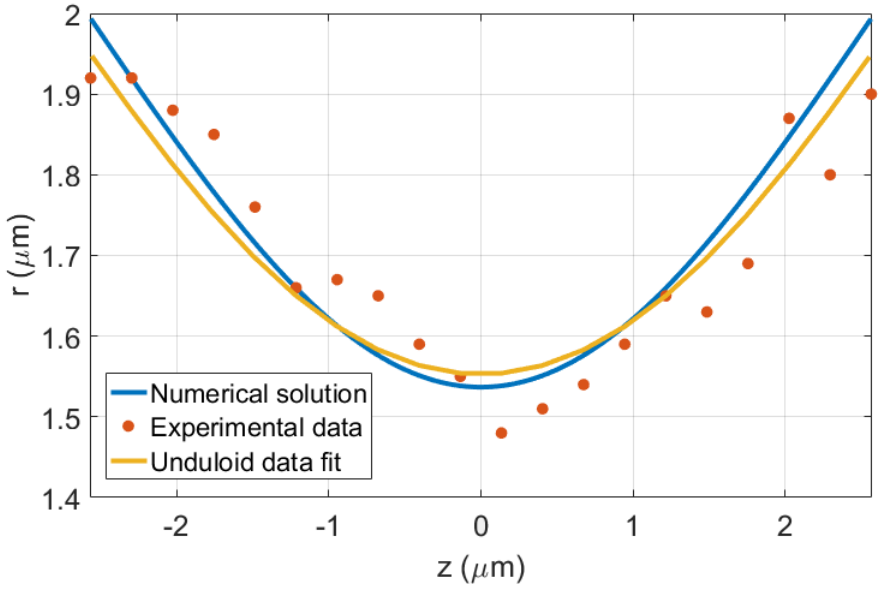

Figure 3.5: Comparison of experimental unduloid data with theoretical profile and data fit using c_0 and the neck as free parameters. The spontaneous curvature for the blue line is $c_0 = 0.4\mu\text{m}^{-1}$, the bending stiffness is $\kappa = 1.5 \times 10^5 k_B T$, $\bar{\kappa} = 200 k_B T$, $B = 100 k_B T \mu\text{m}$, $\gamma = 570 k_B T/\mu m$. The area is $55\mu\text{m}^2$.

3.3.3 Delaunay surfaces

We use the effective energy 1.34 with c^* and B' set to zero, since there is no geodesic torsion at the edge of an axisymmetric surface.

$$E_{und} = \frac{\kappa}{2}\int (2H - c_0)^2 dA + \bar{\kappa}\int K dA + \mu\int dA + \Gamma\int ds + \frac{B}{2}\int k^2 ds \qquad (3.9)$$

In terms of our minimal model Eqn. 3.9, the nonuniform concentration difference of short rods throughout the monolayer can be modeled as a spontaneous curvature c_0. However, the large bending stiffness of the membrane implies the mean curvature globally cannot deviate from this preferred value. The result is that the saddles merge into a single axisymmetric shape with constant mean curvature. (Note that we have checked that 2 saddles/Enneper's surfaces each with area $A/2$ is always less energy than the unduloid.)

From the classical geometric theory of surfaces, the only axisymmetric nonplanar constant mean curvature surfaces are the sphere, cylinder, catenoid, unduloid, and nodoid, known as the Delaunay surfaces [20, 9, 25]. We emphasize that the observed surfaces cannot be catenoids because they have a nonzero mean curvature while catenoids are minimal surfaces. From the remaining choices, it is a matter of selecting the shape that minimizes the Gaussian curvature and edge energy; for an area of $\sim 40\mu m^2$, this turns out to be the unduloid. Fig. 3.5 shows a comparison of the unduloid with spontaneous curvature calculated from the model in the previous section and an experimental height profile. The theoretical membrane profile is computed by numerically solving the Euler-Lagrange equations associated with Eqn. 3.9 subect to no-force and no-torque boundary conditions; details can be found in Appendix B, Sections 1 and 2.

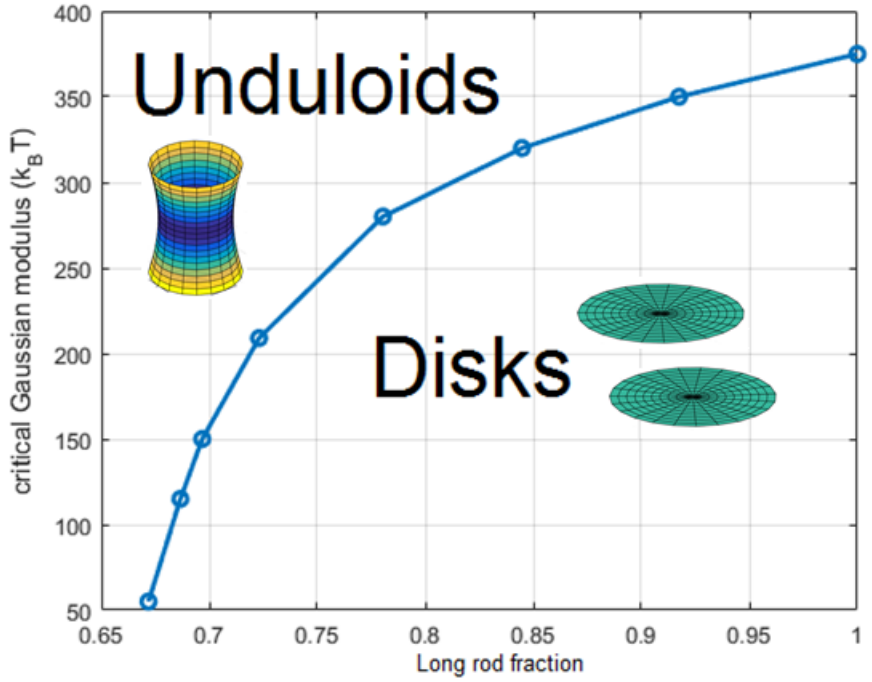

Figure 3.6: Critical Gaussian curvature modulus needed for unduloid formation as a function of long rod fraction. The bending stiffness is $\kappa = 1.5 \times 10^5 k_B T$, $B = 100 k_B T \mu$m, $\gamma = 570 k_B T/\mu m$. The area is $40\mu\text{m}^2$.

Although we use the terminology "unduloid" to refer to these axisymmetric shapes with genus 2, the shapes are mathematically not unduloids, as they disagree slightly due effects at the boundary; consequently, the mean curvature is nearly $c_0/2$ everywhere but not *exactly* $c_0/2$. Indeed, it has been shown that there do not exist "pure" constant mean curvature solutions of the shape equation when B and $\bar{\kappa}$ are zero [64]. As the discrepancy between a pure unduloid and the observed membrane shape is small on the scale of the membrane radius (Fig. 3.5), we will proceed with this slight abuse of terminology.

3.3.4 Critical Gaussian curvature modulus for unduloid formation

As the integral of the Gaussian curvature modulus is a topological invariant for closed surfaces, $\bar{\kappa}$ is notoriously difficult to measure for membranes. For colloidal membranes, which tend to assume open surfaces, theoretical estimates based on the increase of excluded volume for the depletants for surfaces with negative Gaussian curvature place the value of $\bar{\kappa}$ around $200k_BT$ [28]. Here, we will examine the critical Gaussian curvature modulus necessary to make unduloid formation more favorable than two disks as a function of long rod fraction, which provides another way to estimate $\bar{\kappa}$.

The energy of a disk with area $A/2$ is

$$E_{disk} = \sqrt{2\pi A}\left(\Gamma + \frac{B\pi}{A}\right) \tag{3.10}$$

To find the critical value of $\bar{\kappa}$, we must identify when $E_{und} = 2E_{disk}$ for various values of c_0, which we have related to the long rod fraction through Eqn. 3.8. Fig. 3.6 summarizes this data. Note that according to Fig. 3.3, unduloids start appearing around 75% long rods. The corresponding critical $\bar{\kappa}$ is $\sim 250k_BT$, which is close to the previously estimated value.

3.3.5 Comparison with full liquid crystal energy

The minimal model Eqn. 1.34 relies on the assumption that the liquid crystalline energy contributes primarily at the edges of the surface, which is most true when twist penetration depth λ is much smaller than the membrane width w. However, with $\lambda \sim$

1μm [51], this is not quite the case for unduloids, as evidenced by Fig 3.5. Therefore, it is worth checking whether or not the full liquid crystal energy gives results that differ from the ones obtained above using the minimal model. In Appendix B sections 3 and 4, we derive the Euler-Lagrange equations and no-force/no-torque boundary conditions with the full liquid crystal energy terms, using an angle θ to represent the tilt of the director relative to the surface normal. The equations are then solved using MATLAB's `bvp4c` in a procedure very similar to the one outlined above. Fig 3.7 shows the minimizers of the two different energy models for the same parameters. The difference between the profiles is very small, mostly due to the fact that $\kappa \gg \bar{\kappa}$ poses a severe constraint on the shape and forces the membrane into an unduloid-like geometry. We emphasize that the minimal model is considerably more tractable while giving up very little in the way of accuracy, making it the preferred energy model whenever $\lambda \ll w$.

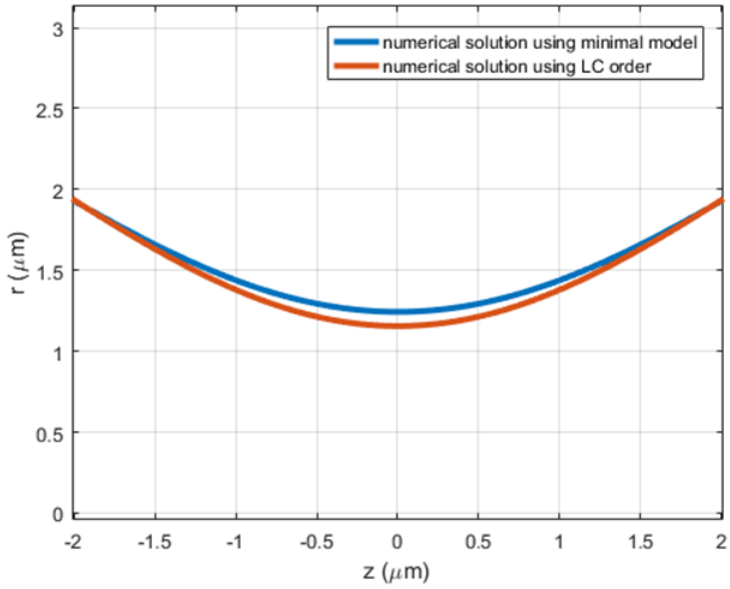

Figure 3.7: Comparison of the minimizer of the minimal model (blue) with the minimizer of the energy with full liquid crystalline order. The bending stiffness was $\kappa = 1.5 \times 10^5 k_B T$, $\bar{\kappa} = 200 k_B T$, $K = 100 k_B T$, $C = 100 k_B T/\mu\text{m}^2$, $q = 1\mu\text{m}^{-1}$, $A = 40\mu\text{m}^2$, $c_0 = 0.4\mu\text{m}^{-1}$, and $\Gamma = 570 k_B T$. For the blue line, $B = 100 k_B T \mu m$ and for the red line, $B = 0.1 k_B T \mu m$

.

3.4 Willmore surfaces with fixed area

In mathematical literature, the Canham-Helfrich energy with $\mu = 0$ and $\bar{\kappa} = 0$ is known as the Willmore functional, and its stationary immersions are known as Willmore surfaces [68], of which minimal surfaces are a subclass. While Willmore surfaces with Dirichlet boundary conditions (i.e. fixed ring radius and zero torque at the boundary) have been studied [10, 16, 17], here we will study the problem with an additional area constraint. Physically, this models the force necessary to hold an incompressible membrane with the topology of a catenoid at a given extension.

To begin, we first consider $\bar{\kappa} = 0$ and study axisymmetric minimizers of the energy

$$E/2\pi = \frac{1}{2}\int (2H)^2 r ds + \mu \int r ds + \int \gamma(s)(r_s - \cos\psi) ds + \int \eta(s)(z_s + \sin\psi) ds \quad (3.11)$$

where we have dimensionlessized by κ. The Lagrange multipliers $\gamma(s)$ and $\eta(s)$ allow the variations in r, ψ, and z to be taken independently. The boundary conditions are the fixed distance between the rings Z and the fixed ring radius, which has been set to 1 (in principle, this radius is set by the line tension Γ and edge bending stiffness B). We will assume the area is fixed at $A_0 = 2\pi$ (the area enclosed by the rings) and μ is a Lagrange multiplier enforcing this constraint.

The Euler-Lagrange equation in z leads to the realization that η is constant, while the variations in ψ and r lead to the ordinary differential equations

$$\psi_{ss} = \frac{1}{r}\left[-\psi\cos\psi + \frac{\cos\psi\sin\psi}{r} + \gamma\sin\psi + \eta\cos\psi\right] \quad (3.12)$$

and

$$\gamma_s = \frac{1}{2}\psi_s^2 - \frac{\sin^2\psi}{r^2} + \mu \tag{3.13}$$

We have fixed endpoints, but ψ is free, so we enforce natural boundary condtions:

$$\left.\frac{\partial \mathcal{L}}{\partial \psi_s}\right|_{s=0,L} = 2H|_{s=0,L} = 0 \tag{3.14}$$

where $2H = \psi_s + \frac{\sin\psi}{r}$ is twice the mean curvature. Physically, this is the requirement that no external bending moments are applied.

Note that the total arclength L is still unknown. Our first-order system thus contains the nine variables $r, z, \psi, \psi_s, \eta, A, \mu, \gamma$ and L and requires an equal number of boundary conditions to solve. Let $t = s/L$, with $t = 0$ representing the right endpoint and $t = 1$ representing the left endpoint. Our boundary conditions are

$$r(t=0) = 1 \ , \ z(t=0) = Z \ , \ H(t=0) = 0 \ , \ A(t=0) = 0$$
$$r(t=1) = 1 \ , \ z(t=1) = -Z \ , \ H(t=1) = 0 \ , \ A(t=1) = 2\pi$$

By virtue of the integrand $\mathcal{L}$ not depending on s explicitly, we find a conserved quantity $\mathcal{H} = \mathcal{L} - \psi_s \frac{\partial \mathcal{L}}{\partial \psi_s} - r_s \frac{\partial \mathcal{L}}{\partial r_s} - z_s \frac{\partial \mathcal{L}}{\partial z_s}$. The transversality condition implies that $\mathcal{H} = 0$ (see Appendix B), so that

$$0 = -\frac{r}{2}\left(\psi_s^2 - \frac{\sin^2\psi}{r^2}\right) + \mu r - \gamma\cos\psi + \eta\sin\psi \tag{3.15}$$

can be used as the ninth boundary condition. Note that at the midpoint of the surface, $\psi = \pi/2$ and one can show that,

$$F/2\pi = -\eta = -\frac{b}{2}\left[\psi_s(s = L/2)^2 - \frac{1}{b^2}\right] + \mu b \tag{3.16}$$

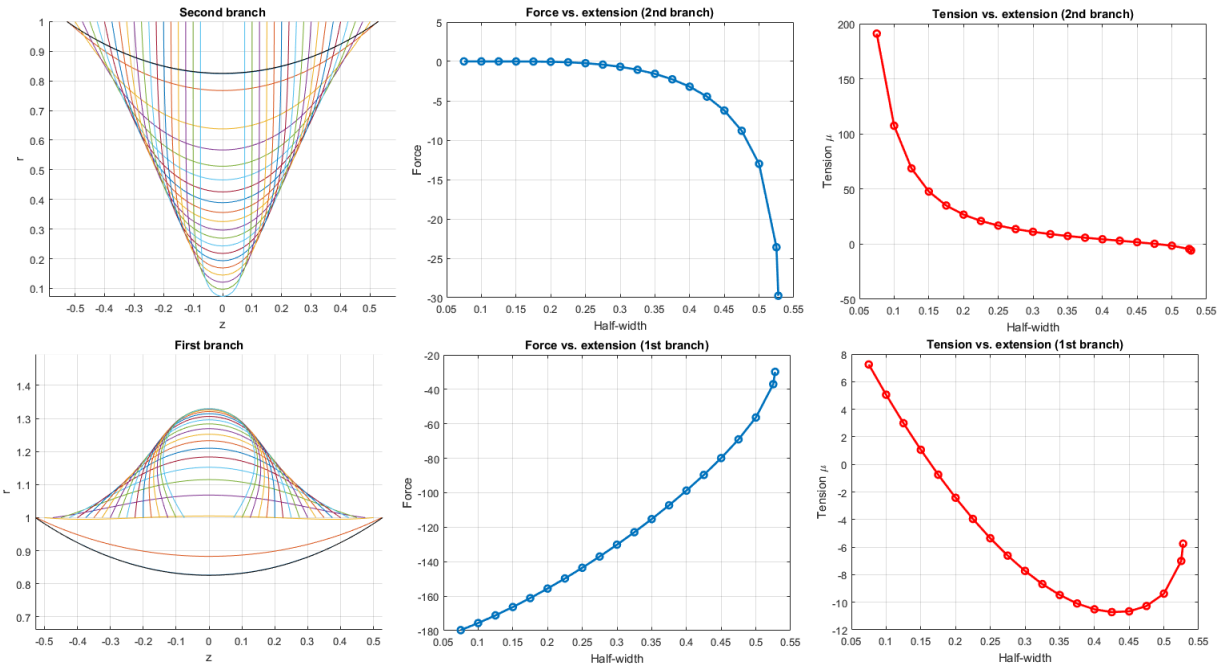

Figure 3.8: Force vs. extension of a membrane with the topology of a catenoid. (Left) Various shapes of the membrane for a given extension. The black line is a catenoid with area 2π and ring radius 1 and represents the shape with maximum extension. (Middle) The blue line is the dimensionless force required to hold the ends at a given half-width (note that negative force means compression). (Right) The red line is the dimensionless surface tension μ.

where b is the neck (radius at the midpoint) and F is the force applied at the boundaries (here we take $F > 0$ to mean an extensile force).

Fig. 3.8 shows the various minimal energy shapes, whose surfaces of revolution are Willmore surfaces with area equal to 2π. Note that there is a maximum extension; the corresponding shape at this extension is a catenoid, whose ring radius is 1.

However, if we increase the area, then there is no maximum extension; the membrane has enough area to form a cylindrical "tether" that can connect the two nearly flat rings (Fig. 3.10). The force consequently looks linear at large extensions. We can explain this result by estimating the shape of the membrane as two circles of area π connected by a cylinder of radius b:

$$A \simeq 2\pi + 4\pi bz. \tag{3.17}$$

which leads to the fact that $z \simeq (A - 2\pi)/4\pi b$. From the membrane shape equation (Eqn. 1.20) and the fact that $H = 1/2b$ and $K = 0$ for a cylinder, we get

$$2H^3 = \mu H \implies \mu \simeq \frac{1}{2b^2} \tag{3.18}$$

The area constraint Eqn. 3.17 provides a way to estimate μ as a function of the extension; $\mu = O(z^2)$ when $z \gg 1$. The force can be found using Eqn. 3.16 and the fact that the cylinder is flat at the neck:

$$F = \frac{\pi}{b} + 2\pi\mu b = O(z) \tag{3.19}$$

As Fig. 3.10 shows, it is possible for a membrane with the topology of a catenoid to have zero force and zero torque. Such a free-standing surface is typically quite flat, with only a small variation in radius from end-to-end. For this reason, we gave these shapes the nickname "flatenoids;" although they have not yet been observed in experiments, they are nonetheless possible in theory, as long as $\kappa/\bar{\kappa}$ is not large. Otherwise, the membrane will prefer to form a catenoid as the catenoid is the only axisymmetric nonplanar minimal surface.

3.5 Colloidal vesicles

Due to their extraordinarily high bending rigidity, colloidal membranes were long thought to be unable to wrap up into vesicles as lipid bilayer membranes commonly do. But recent experiments have shown that this is indeed possible for larger, less stiff membranes composed of a shorter species of virus. The shapes of these sagging vesicles are parameterized by a single dimensionless constant: a ratio of elastic bend-

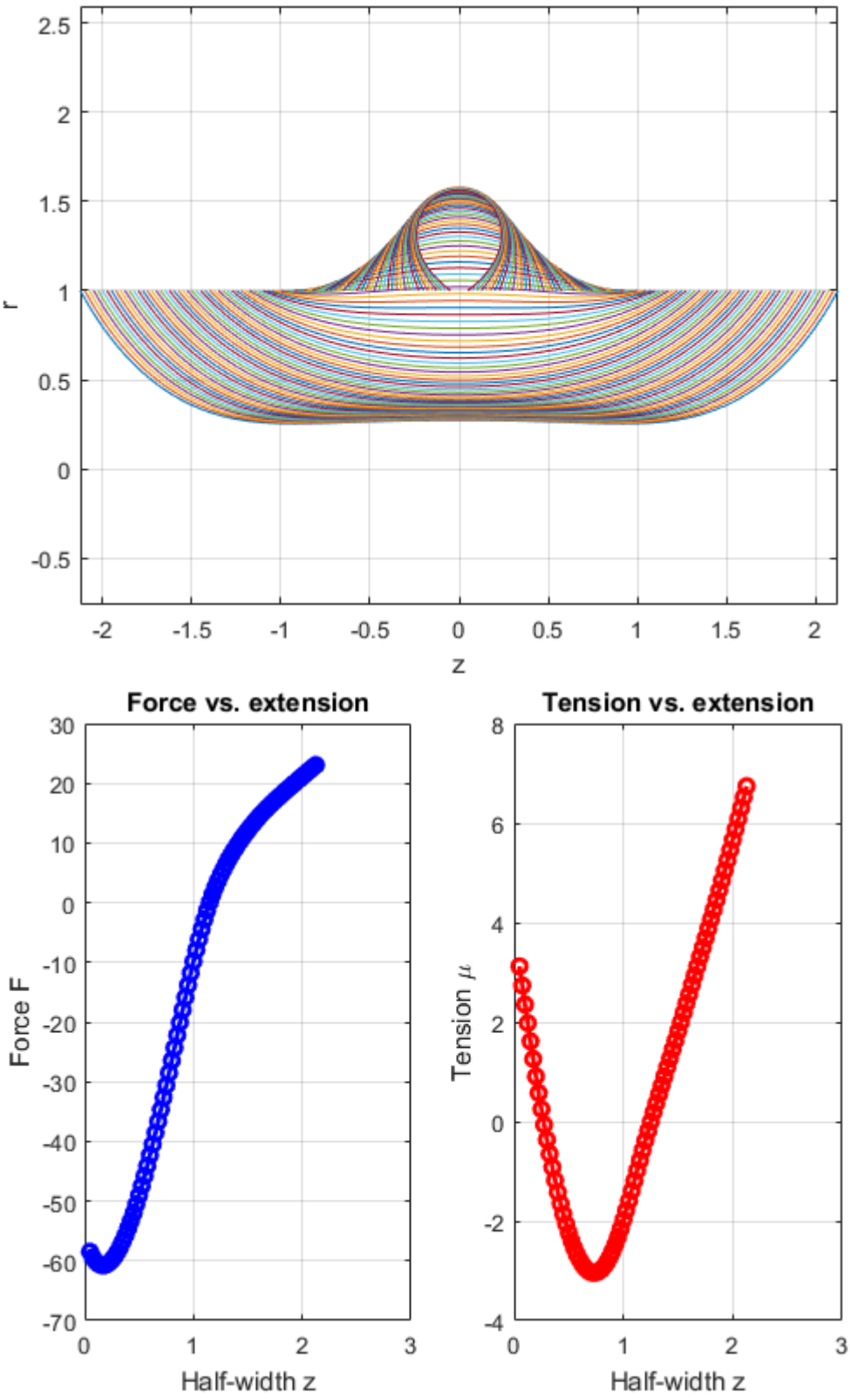

Figure 3.9: (Top) Formation of tethers for a membrane with larger area. The area is 4π. (Bottom) The force vs. extension is linear at large z and there is no maximal extension. The tension μ vs. extension is quadratic.

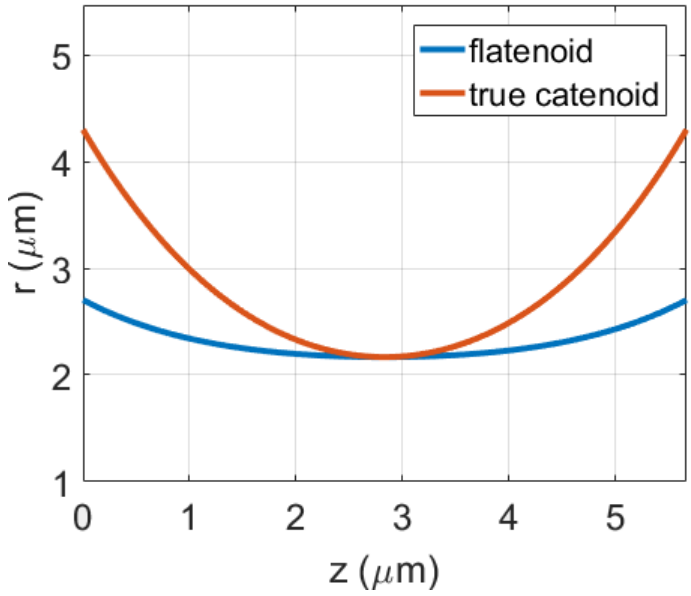

Figure 3.10: An example of a ''flatenoid" (blue) which is a force-free axisymmetric equilibrium surface. The catenoid with the same neck (red) has much larger curvature.

ing energy to gravitational energy, allowing us to estimate the bending rigidity of these membranes. We have also begun to analyze the "vesicle with a hole" problem in the hopes of gaining a better understanding of the process through which a large disk wraps up into a vesicle. Tentative results indicate there is no energetic barrier to vesicle formation if the area is large.

3.5.1 Experimental methods

Experimental procedures were done and data was collected by Joanna Robaszewski and biological materials were provided by Mahsa Siavashpouri as part of Zvonimir Dogic's research group. Filamentous bacteriophage with a length of $\sim 380\mu$m was grown and purified following previously established biological protocols [55]. The viruses were fluorescently labeled with Dylight 550 NHS ester dye using previously described methods [48]. The labeled viruses were suspended in tris-HCl buffer and mixed with dextran to induce attractive depletion forces and cause condensation of

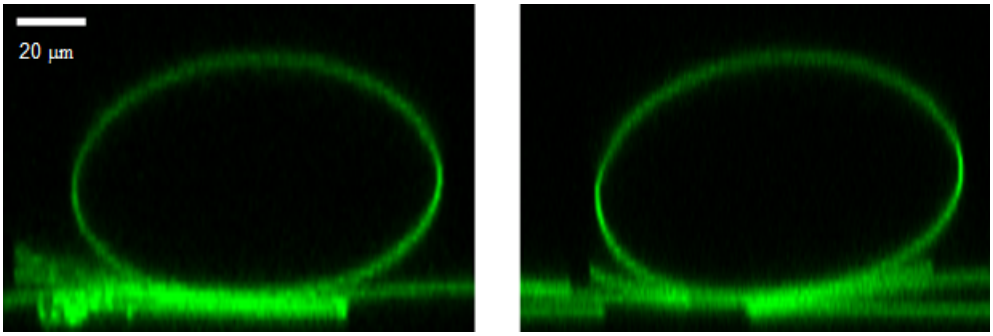

Figure 3.11: (Left) Image of a fully closed colloidal vesicle sagging in a gravitational field (xy-plane). (Right) Same vesicle seen from the side (yz-plane). Scale bar is 20μm.

the viruses into monolayer membranes, along with sodium azide (NaN3) to eliminate bacteria from the sample. Membrane growth and subsequent vesicle formation were visualized using a confocal laser scanning microscope (Leica TCS SP8). Z-stack images were taken of the vesicles after they formed their equilibrium structures. The z-stacks were then used to reconstruct the three dimensional structure of the vesicles with Leica Application Suite X software.

3.5.2 Minimal model for vesicles

Colloidal vesicles are much larger than ordinary colloidal membranes, with a radius of ~ 50 microns, and thus sag due to gravity (Fig 3.11). In order to analyze these shapes, we add a gravitational term to our minimal energy. Note that the Gaussian curvature term does not influence the energy of a closed vesicle due to the Gauss-Bonnet theorem (Eqn. 1.13). Since the rod length is much smaller than the vesicle radius, we continue to treat the membrane as an axisymmetric two-dimensional shell, with areal mass density σ. If z is the height above the floor and r is the radial

component, then in total we have

$$E = \frac{\kappa}{2}\int (2H)^2 dA + \sigma g \int z dA + \mu \int dA + \int \gamma(s)(r_s - \cos\psi)ds + \int \eta(s)(z_s + \sin\psi)ds \tag{3.20}$$

where $g = 9.8 \times 10^6 \mu\text{m}/s^2$ is the acceleration due to gravity and $\gamma(s)$ and $\eta(s)$ are functional Lagrange multipliers that enforce geometric constraints at each s. Unlike lipid bilayer vesicles, the volume is not conserved as the membrane is permeable to water. However, we continue to assume that the total surface area is fixed.

While most of the Euler-Lagrange equations are unchanged by the addition of the gravitational term and can be found in Appendix B, the inclusion of a term that depends on z introduces a new equation for $\eta(s)$:

$$\eta_s = \sigma g z. \tag{3.21}$$

Thus, η is the elastic response force in the z direction. Letting $t = s/L$, the nine boundary conditions are

$$\begin{aligned} &\psi(t=1) = 0 \ , \ \psi(t=0) = \pi, \\ &r(t=1) = R \ , \ r(t=0) = 0, \\ &A(t=0) = 0 \ , \ A(t=1) = A - \pi R^2, \\ &z(t=1) = 0 \ , \ \eta(0) = 0, \\ &\mathcal{H}(t=0) = 0 \end{aligned} \tag{3.22}$$

i.e. we assume that the surface profile is continuously differentiable and that the vesicle is in contact with the floor with an area of contact πR^2. As before, we also use that the Hamiltonian is zero (the transversality condition, Section B.3), which is a consequence of the shape having unknown length. The radius R at the floor is

fixed but arbitrary and must be minimized to find the true vesicle shape; however, care must be taken to ensure that the solution does not penetrate the floor:

$$R = \text{argmin}_{\bar{R}\geq 0}\{E(\bar{R}) : \min_s z(s) \geq 0\}. \tag{3.23}$$

Note that there is no energy of adhesion with the floor because the vesicle is supported by a polymer brush in experiments. Also, the energy is singular at $t = 0$ due to the boundary condtion there; in practice, one sets $r(t = 0) = 0.001$ or some other positive number small enough to not impact the solution.

The sole characteristic length scale in the problem is

$$l_0 = \left(\frac{\kappa}{\sigma g}\right)^{1/3}. \tag{3.24}$$

From this, we define the dimensionless parameter

$$\alpha = A/l_0^2 = A\left(\frac{\sigma g}{\kappa}\right)^{2/3}. \tag{3.25}$$

Dimensional analysis implies that the vesicle shape is solely a function of α. The vesicle shapes for a variety of values of α are plotted in Fig. 3.12. The spherical vesicle, $\alpha = 0$, correponds to the case where there is no gravity. For $\alpha \lesssim 50$, the membrane is convex but sags due to gravity. When $\alpha \simeq 93$, the membrane becomes tangent to itself, indicating a complete collapse.

3.5.3 Estimating the bending rigidity

We now estimate the parameters in Eqn. 3.25 in order to estimate the bending rigidity κ. While the viruses have a density of 1.4g/cm^3, the membrane is roughly

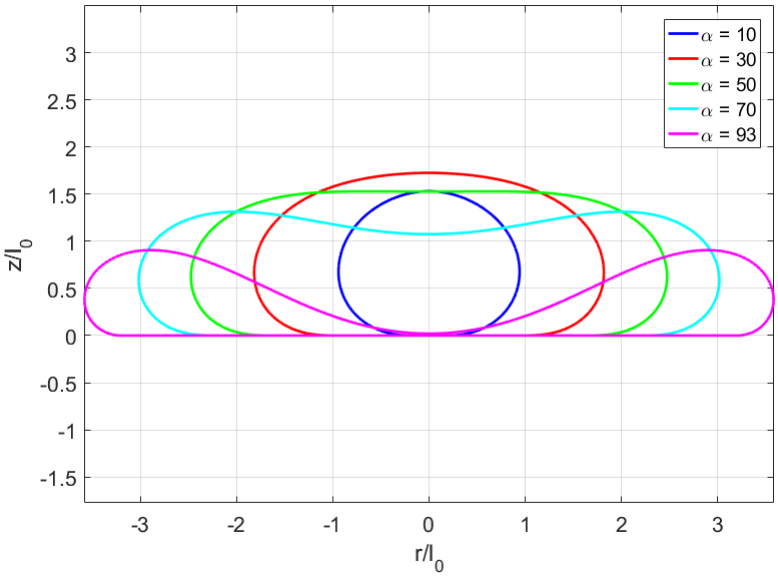

Figure 3.12: Dimensionless vesicle shapes as a function of α. The membrane develops a concave center when $\alpha \simeq 50$. At $\alpha \simeq 93$, the membrane collapses completely.

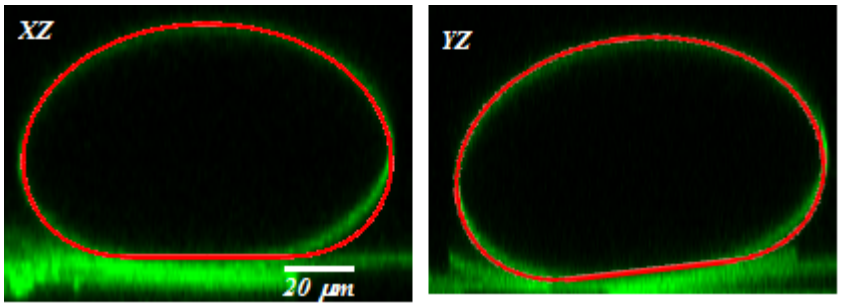

Figure 3.13: Vesicle profiles with theoretical $\alpha = 18$ curve superimposed. Scale bar is 20μm.

80% water by mass, leaving the density difference with the background fluid closer to $\Delta\rho = 0.08\text{g/cm}^3$. To find the areal density, we multiply $\sigma = \Delta\rho d$, where d is the membrane thickness, estimated as $d = 380\text{nm}$.

The area of the vesicle in Fig. 3.11 was measured to be around $3.3 \times 10^4 \mu\text{m}^2$. From fitting the shape of the membrane, $\alpha \simeq 18$ (Fig. 3.13). Using these numbers gives the value of $\kappa \simeq 6000 k_B T$. Our estimate is the correct order of magnitude as one would obtain from using the fact that $\kappa \sim d^3$ and the measured bending rigidity of the 880 nm viruses is around $1.5 \times 10^5 k_B T$.

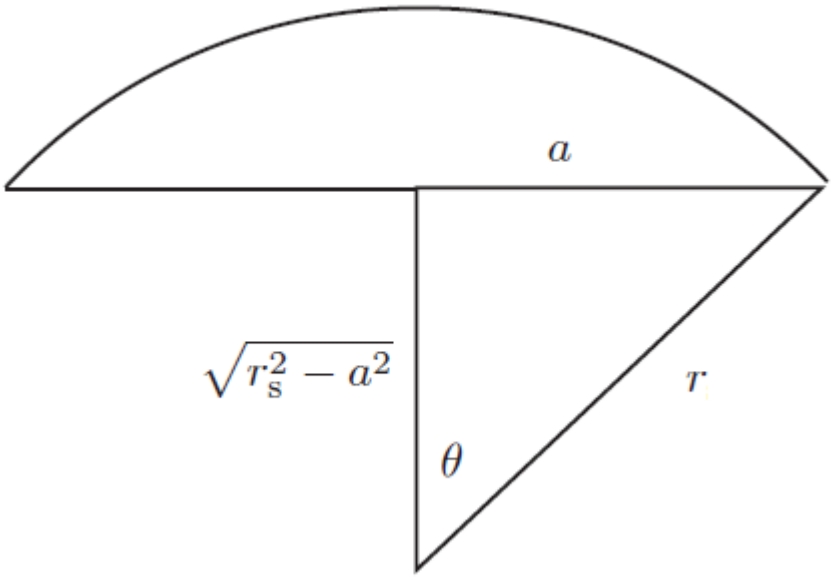

Figure 3.14: A spherical cap of radius r, bounded by a circle of radius a.

3.5.4 Vesicle with a hole

The formation of colloidal vesicles from disks is a relatively recent phenomenon, and it is not quite clear how they transition from disks to closed surfaces. The exact nature of the wrapping process is an open problem even for lipid bilayer membranes and is believed to involve parameters of the background fluid such as viscosity as fluid is expelled as the vesicle seals itself. While we do not have the tools to study this dynamical problem in full detail, we can nonetheless study vesicle wrapping by examining two simple questions: what is the energy barrier if we assume the membrane is shaped like a spherical cap and are there axisymmetric equilibrium solutions of Eqn. 3.20 with a hole?

To answer the first question, suppose that a is the radius of the boundary of the cap (Fig. 3.14). If the cap subtends a polar angle θ, then the area of the cap is given by $A = 2\pi r^2(1 - \cos\theta)$, where $\cos\theta = \sqrt{r^2 - a^2}r$ for $0 < \theta < \pi/2$ and the negative

for $\pi/2 < \theta < \pi$. Solving for a in terms for r yields

$$a = \sqrt{\frac{A}{\pi}\left(1 - \frac{A}{4\pi r^2}\right)}. \tag{3.26}$$

The energy of the cap is then

$$E = (2\kappa + \bar{\kappa})\frac{A}{r^2} + 2\pi\left(\Gamma a + \frac{B}{2a}\right) \tag{3.27}$$

where we have ignored the effect of gravity. By combining Eqns. 3.26 and 3.27, one can verify that for large enough areas, there is no barrier to vesicle formation other than the barrier of closing the hole.

We now discuss the possibility of axisymmetric shapes that are open on one end, as a proxy for the shape of the membrane just before it wraps into a vesicle. In this scenario, the Euler-Lagrange equations and general algorithm are the same as before, but the boundary conditions will be different; now, one side will have a hole where no-force and no-torque conditions are imposed (see Appendix B). As we saw in the case of unduloids, the line tension Γ and edge bending stiffness B set the width of the hole; Fig. 3.15 shows this behavior.

Notably, the radius satisfying 3.23 is essentially the same function of α for both closed vesicles and vesicles with a hole. The energies of the minimizers of the two problems are also comparable; we find $E_{vesicle} \simeq E_{hole} - E_{edge}$. With edge energy, however, $E_{vesicle} < E_{hole}$, suggesting there is no energetic barrier to vesicle formation from this equilibirum shape obtained by minimizing R.

Thus, in total, our crude results suggest the "lotus" wrapping pathway (Fig. 3.16), where a disk with enough area and line tension wraps itself into one of the shapes in

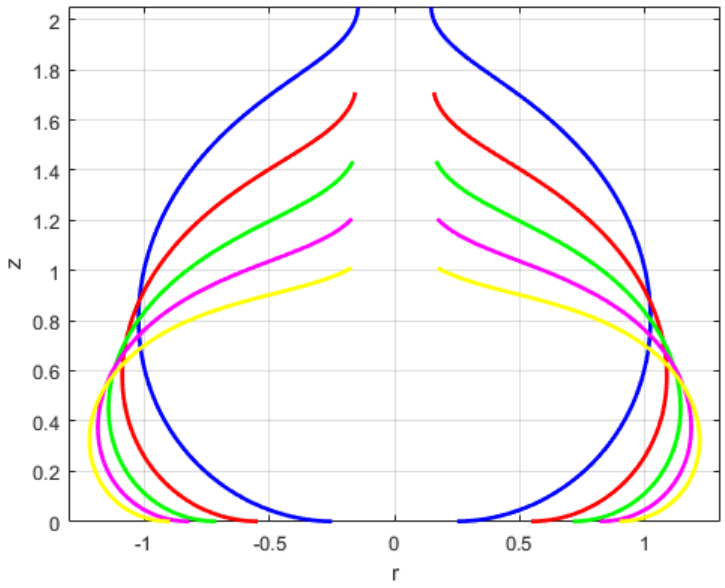

Figure 3.15: Metastable states of a vesicle with a hole. For all shapes $A = 4\pi$, $\kappa = 1$, $\gamma = 1$, $B = 0.1$, $\bar{\kappa} = 0$. The shape parameter α varies from 10 (blue) to 50 (yellow) in increments of 10.

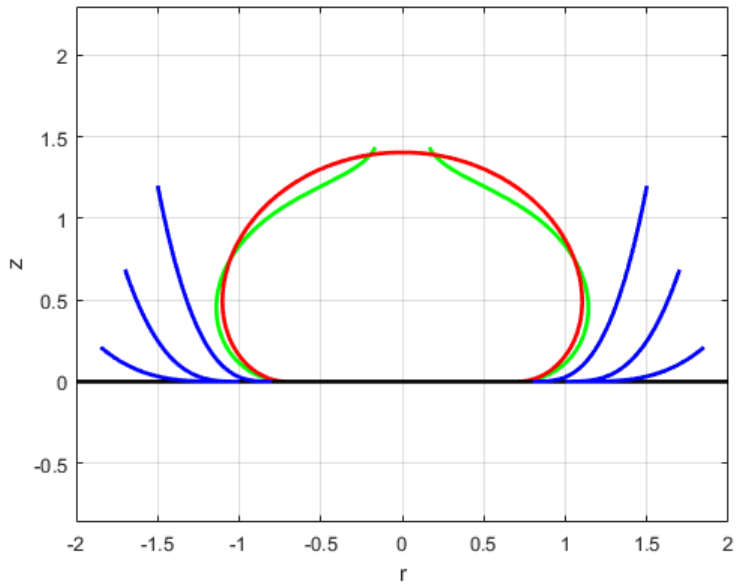

Figure 3.16: Theoretical pathway for the wrapping of a disk into a vesicle. The black line indicates the flat disk. The blue line indicates spherical cap-type shapes. The green line is the metastable state with a hole, and the red line is the final vesicle with the hole sealed.

Fig. 3.15 by transitioning through a series of cap-like shapes, then closes its hole at the last moment. While our model predicts a divergence of the energy as the hole size decreases, the closing of the hole likely occurs in a regime where our assumptions of liquid crystalline order do not apply, and so our current model cannot accurately describe this.

Chapter Four

Force vs. Extension of Ribbons

4.1 Introduction

In another set of experiments, optical tweezers were used to impart a stretching force on antipodal points of a disk-shaped colloidal membrane. Under the application of this force, the membrane not only elongates but also develops twists akin to a helicoidal ribbon. With our effective theory, we capture the correct shape of the nonlinear force vs. extension curve and find that chirality is necessary to transition to the twisted phase. The effective theory works best for small deflections when the membrane is still flat but becomes less accurate for large extensions. This is due to the thinning of the ribbon as it is pulled, which makes the width comparable to the twist penetration depth.

4.2 Experimental methods

Experiments were performed by Andrew Balchunas and Mark Zakhary as part of the research laboratory of Zvonimir Dogic.

Sample Preparation. Filamentous bacteriophages fd-wt, M13-wt, and M13-KO7 were isolated from the supernatant of infected E. Coli ER2738 cells and were purified by PEG precipitation [6, 55]. M13-KO7 is a mutant of M13-wt in which the contour length has been altered, and has been given a gene encoding for Kanamycin resistance. M13-KO7 has more copies of the major coat protein (pVIII) than M13-wt, leading to a 37% increase in length over its parent bacteriophage [24]. All other properties of the virus are left unchanged through the mutation.

Mixing viruses with a non-adsorbing polymer, dextran (MW 500,000, Sigma-

Aldrich), leads to the self assembly of 2D colloidal membranes [5]. Changing the concentration of dextran in the suspension affects the strength of virus-virus attraction and can lead to other equilibrium structures such as quasi 1D colloidal twisted ribbons [27]. All samples were prepared in Tris-HCl buffer (20 mM, pH 8.0) with 100 mM NaCl added to screen electrostatic repulsion between the viruses. The virus and polymer suspensions were injected into homemade chambers made from a glass microscope slide, coverslip (Gold Seal, Fischer) and unstretched Parafilm wax as previously published [6]. The glass slide and coverslip were coated with a poly-acrylamide brush prior to use to prevent non-specific adsorption [47].

For stretching experiments, a chamber resembling a T was made. The virus and polymer mixture was injected into the vertical stem of the T-junction and the assemblage was stored overnight in a humid environment in order to allow sufficient time for membranes to form without allowing the sample to evaporate. Just prior to starting an experiment, a suspension of fluorescent, biotinylated bacterial flagella (SJW 1660, straight morphology [8]) and streptavidin coated silica beads was injected into the horizontal arm of the junction. The bacterial flagella were fluorescently labeled with an amine reactive dye (NHS-Rhodamine). The sample was then sealed using glue that cures under ultraviolet light (Norland Optical).

Optical Microscopy. Experiments were performed using an inverted microscope (Nikon Eclipse Te2000-u) outfitted with a high magnification, high N.A., oil immersion objective (Nikon, PlanFluor, 100x, N.A. 1.3). Images were recorded using a cooled CCD camera (CAMERA MANUFACTURER). An LED light source (SOLA Light Engine, Lumencor) was used to excite the fluorescent dye, and a dichroic filter cube (Semrock) was used to collect the emitted light from the flagella.

Laser Tweezers. Focusing a high-powered 1,064 nm laser (Coherent Compass) on

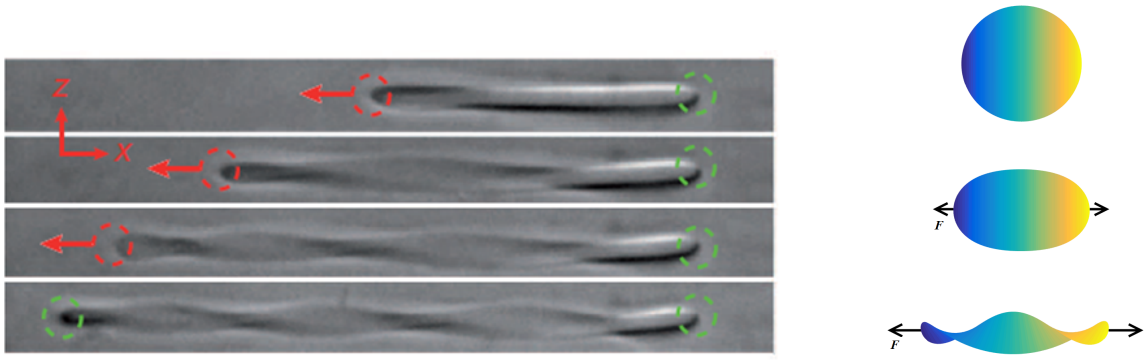

Figure 4.1: (Left) Optical tweezers are used to impart a diametric stretching force on a disk-shaped colloildal mmebrane. The disk diameter is initially 5μm; the length of the ribbon in the bottom figure is $\sim 20\mu$m. (Right) Schematic of top-down view.

the focal plane of an inverted microscope (Nikon Eclipse Te2000-u), through a high magnification, high N.A. oil immersion objective (Nikon, PlanFluor, 100x, N.A. 1.3), produced an optical tweezer that could be used to manipulate colloidal particles. An acousto-optical deflector (AOD) (IntraAction-276HD) was used to simultaneously trap multiple beads. The AOD time shares a single beam across multiple positions so quickly that the trapping appears simultaneous. The traps were controlled using a homemade LabVIEW subroutine and motorized stage.

Position of the detection bead was measured using back focal plane interferometry and a quadrant photodiode. A second 830 nm laser (Point Source Iflex2000) was incorporated into the setup as the detection beam. Trap stiffness was calibrated by analyzing the power spectrum of the bead position [1].

4.3 Small extensions of a flat membrane

It has been observed that for small extensions, the membranes do not twist, and the force as a function of extension is approximately linear. Here, we will estimate the spring constant k_s of this linear relation.

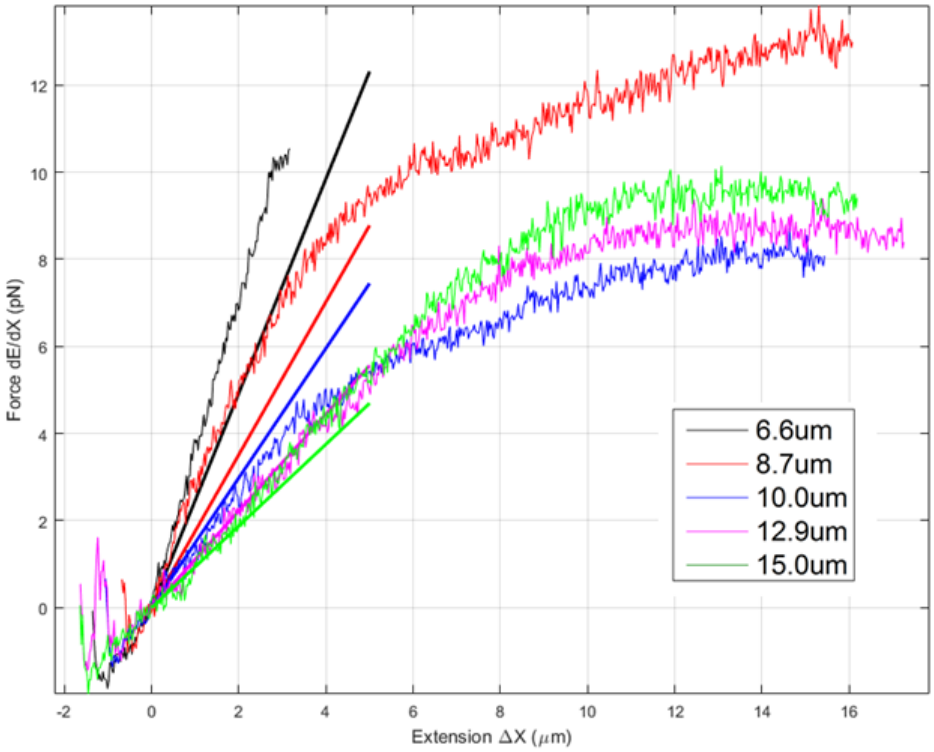

Figure 4.2: Force vs. extension for colloidal membranes of various radii, along with theoretical small stretch linear lines (see Section 4.3).

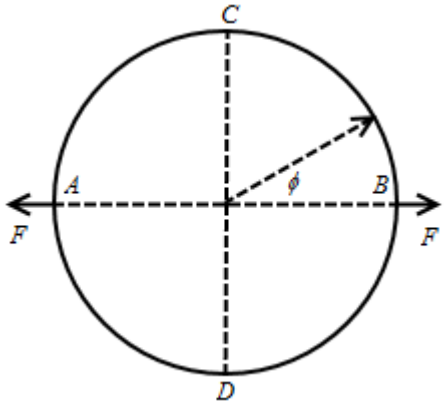

Figure 4.3: Equal and opposite forces of magnitude F acting diametrically on a membrane at locations A and B. We assume $F > 0$ for outward forces as shown.

Consider an incompressible flat membrane subject to equal and opposite external forces, as in the figure, except we will take positive force F to be outward rather than inward. Also, we will use F for the dimensional force, and f for dimensionless force, as described below. The membrane has an area πa^2 in the absence of forces, and line tension Γ. We will also assign a bending stiffness B to the edge of the membrane; this stiffness represents the contribution from the bend of the tilted virus particles to the Frank free energy. We will not consider the conformation of the virus particles, but instead use the simpler theory of an incompressible membrane with edge tension and edge bending stiffness. Approximating the energy in this way is appropriate when the twist is confined to a thin annulus at the edge of the membrane.

The problem is to find the deformation of the membrane for small forces, $F \ll \Gamma$; denoting by x the total displacement of B relative to A (Fig. 4.3), we seek to calculate the spring constant $k_s = F/x$. To find the governing equations, we first dimensionlessize by measuring length in units of a, and force in units of Γ. The shape is given by the radius $r(\phi) = 1 + \zeta(\phi)$, where $\zeta(\phi) \ll 1$ and $-\pi < \phi < \pi$. The configuration of the membrane is found by minimizing

$$W = \int \mathrm{d}s + \frac{b}{2}\int \mathrm{d}s k^2 - pA - f\zeta(0) - f\zeta(\pi), \tag{4.1}$$

where the total energy W is measured in units of λa, s is the arc length of the edge, k is the dimensionless curvature of the edge, $b \equiv B/(\lambda a^2)$, p is the Lagrange multiplier enforcing the area constraint, A is the area, and $f \equiv F/\Gamma$. Next, we expand W to second order in ζ and then find the variation. We use

$$\mathrm{d}s = \sqrt{\frac{\mathrm{d}\mathbf{r}}{\mathrm{d}\phi}\cdot\frac{\mathrm{d}\mathbf{r}}{\mathrm{d}\phi}}\mathrm{d}\phi, \tag{4.2}$$

where $\mathbf{r} = (1+\zeta)\hat{\boldsymbol{\rho}}$ and $\hat{\boldsymbol{\rho}} = (\cos\phi, \sin\phi)$ is the unit radial vector. Also, the curvature

k is given in terms of the tangent vector $\hat{\mathbf{T}} = \mathrm{d}\mathbf{r}/\mathrm{d}s$ by

$$k^2 = \frac{\mathrm{d}\hat{\mathbf{T}}}{\mathrm{d}s} \cdot \frac{\mathrm{d}\hat{\mathbf{T}}}{\mathrm{d}s}. \tag{4.3}$$

Expanding to $\mathcal{O}(\zeta^2)$ yields

$$\begin{aligned} W = & \int \mathrm{d}\phi \left(1 + \zeta + \frac{1}{2}\zeta'^2\right) + \frac{b}{2}\int \mathrm{d}\phi \left(1 - \zeta + \zeta^2 + \frac{3}{2}\zeta'^2 - 2\zeta'' + 4\zeta\zeta'' + \zeta''^2\right) \\ & - \frac{p}{2}\int \mathrm{d}\phi \,(1+\zeta)^2 - f\int \mathrm{d}\phi \,(\delta(\phi) + \delta(\phi - \pi)) \,. \end{aligned} \tag{4.4}$$

Computing the variation yields

$$\begin{aligned} \delta W = & \int \mathrm{d}\phi\delta\zeta \left[b\left(\zeta^{(\mathrm{iv})} + \frac{5}{2}\zeta'' + \zeta - \frac{1}{2}\right) + (1 - \zeta'') - p\,(1+\zeta) - f\,(\delta(\phi) + \delta(\phi - \pi))\right] \\ & + \left[\delta\zeta\,(-b\zeta''' - b\zeta'/2 + \zeta')\right]_{\phi_0}^{\phi_1} + \left[\delta\zeta' b\,(\zeta'' + 2\zeta - 1)\right]_{\phi_0}^{\phi_1}, \end{aligned} \tag{4.5}$$

where ϕ_0 and ϕ_1 are the lower and upper endpoints of the region of integration, respectively. From these boundary terms we deduce the first-order shearing force

$$f_{\mathrm{shear}} = -b\zeta''' - b\zeta'/2 + \zeta' \tag{4.6}$$

and the first-order bending moment

$$m = b(\zeta'' + 2\zeta - 1). \tag{4.7}$$

Demanding $\delta W = 0$ yields

$$b\left(\zeta^{(\mathrm{iv})} + \frac{5}{2}\zeta'' + \zeta - \frac{1}{2}\right) + (1 - \zeta'') - p\,(1+\zeta) - f\,[\delta(\phi) + \delta(\phi - \pi)] = 0. \tag{4.8}$$

The pressure p is determined by the condition $A = \pi$, which to first order in ζ is

$\int \mathrm{d}\phi\zeta = 0$. Integrating Eqn. (4.8) over the circle yields

$$p = -\frac{f}{\pi} + 1 - \frac{b}{2}. \tag{4.9}$$

Note that we have skipped over a subtlety here. The shearing force is not continuous at point A and B, so it might not be immediately clear that the integral of the fourth derivative of ζ vanishes. To see that it does, we can either (a) smooth out the delta functions, so that none of the derivatives of ζ are discontinuous, or (b) keep track of each of the jumps in ζ''' at 0 and $\pm\pi$. Either procedure shows that $\oint \mathrm{d}\phi\zeta^{(\mathrm{iv})} = 0$.

Inserting the expression (4.9) into Eqn. (4.8) yields

$$b\left(\zeta^{(\mathrm{iv})} + \frac{5}{2}\zeta'' + \frac{3}{2}\zeta\right) - (\zeta'' + \zeta) + \frac{f}{\pi} + f\left[\delta(\phi) + \delta(\phi - \pi)\right] = 0. \tag{4.10}$$

We can find boundary conditions on ζ''', ζ'' and ζ' by integrating (4.10) against 1, ϕ, and ϕ^2, respectively. Or we can simply say that the shear force must jump by f at A and B but the moment is continuous along with ζ and ζ' (the latter because otherwise we would have an infinite energy cost for a corner). To simplify the solution of (4.10), we impose mirror-reflection symmetry about AB and CD (Fig. 4.3). Since there will be discontinuities in third derivatives, let

$$\zeta = \begin{cases} \zeta_+ & \text{if } 0 < \phi < \pi \\ \zeta_- & \text{if } -\pi < \phi < 0, \end{cases} \tag{4.11}$$

where

$$\zeta_+ = \frac{2f}{(2-3b)\pi} + c_1 \sin\phi + c_2\left[\sinh\left(\phi\sqrt{\frac{1}{b} - \frac{3}{2}}\right) + \sinh\left((\pi - \phi)\sqrt{\frac{1}{b} - \frac{3}{2}}\right)\right] \tag{4.12}$$

$$\zeta_- = \frac{2f}{(2-3b)\pi} - c_1 \sin\phi - c_2\left[\sinh\left(\phi\sqrt{\frac{1}{b} - \frac{3}{2}}\right) - \sinh\left((\pi + \phi)\sqrt{\frac{1}{b} - \frac{3}{2}}\right)\right] \tag{4.13}$$

We might worry that we need to turn the hyperbolic functions into circular functions when $b > 2/3$, but there will be compensating roots in c_2 that prevent ζ from being complex. Imposing continuity of ζ' at $\phi = 0$ and the jump in the shearing force

$$[b\zeta''']_{0_-}^{0^+} = f \tag{4.14}$$

yields

$$c_1 = \frac{f}{b-2} \tag{4.15}$$

$$c_2 = \frac{f}{(b-2)\sqrt{\frac{1}{b}-\frac{3}{2}}\left[\cosh\left(\pi\sqrt{\frac{1}{b}-\frac{3}{2}}\right)-1\right]}. \tag{4.16}$$

Note that even though the coefficients diverge at certain values of b, the fundamental solutions have compensating zeros that keep ζ finite, i.e.

$$\lim_{b\to 1}\zeta_+ = -\frac{f}{2\pi} + \frac{f}{16}(\pi - 2\phi)\cos\phi + \frac{f}{8}\sin\phi \tag{4.17}$$

$$\lim_{b\to \frac{2}{3}}\zeta_+ = f\left(\frac{3}{2\pi} - \frac{\pi}{8}\right) + \frac{3f\phi}{4}\left(1 - \frac{\phi}{\pi}\right) - \frac{3f}{4}\sin\phi; \tag{4.18}$$

or, the diverging parts are killed by rapidly vanishing parts:

$$\lim_{b\to 0}\zeta_+ = f\left(\frac{1}{\pi} - \frac{1}{2}\sin\phi\right). \tag{4.19}$$

The total displacement of B relative to A is given by $x = \zeta(0) + \zeta(\pi)$, and the spring constant k_s for the deformation is given by

$$k_\mathrm{s} = f/x. \tag{4.20}$$

We find

$$k_{\rm s} = \frac{\pi(2-b)(2-3b)}{8-4b-2\pi\sqrt{4-6b}\sqrt{b}\coth\left(\frac{\pi\sqrt{1-\frac{3b}{2}}}{2\sqrt{b}}\right)}. \tag{4.21}$$

For small b, we have

$$k_{\rm s} = \frac{\pi}{2} + \frac{\pi^2\sqrt{b}}{4} + \mathcal{O}(b), \tag{4.22}$$

where we have dropped exponentially small terms such as $\exp(-1/b)$. In dimensional form, the spring constant for $B \ll \Gamma a^2$ is

$$k_{\rm s} = \frac{\pi\Gamma}{2a} + \frac{\pi^2}{4}\sqrt{\frac{\Gamma B}{a^4}} + \cdots \tag{4.23}$$

For large b, the spring constant is

$$k_{\rm s} = -\frac{3\pi b}{4+2\sqrt{6}\pi\cot\left(\frac{1}{2}\sqrt{\frac{3}{2}}\pi\right)} + \mathcal{O}(1) \tag{4.24}$$

$$k_{\rm s} \approx 5.641b, \tag{4.25}$$

Or $k_{\rm s} \approx 5.641B/a^3$ when $B \gg \Gamma a^2$.

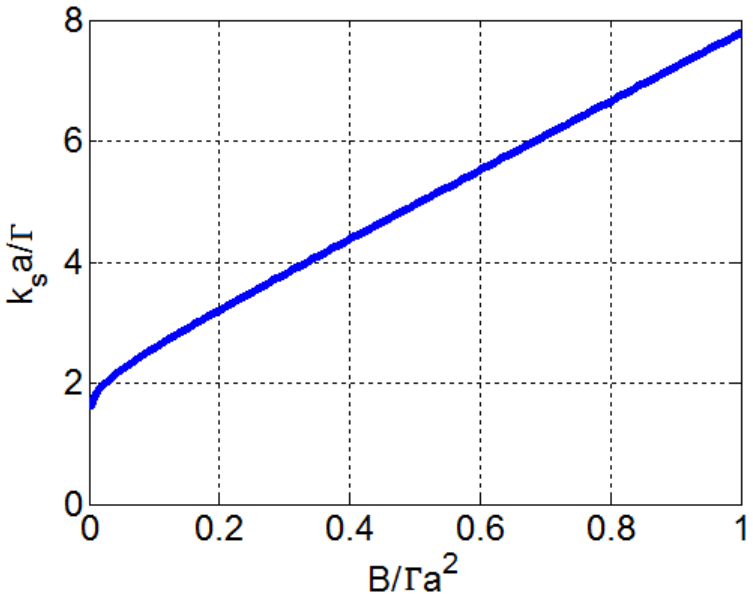

Figure 4.4: Plot of dimensionless spring constant vs dimensionless edge bending stiffness.

Plotting the spring constant vs edge bending stiffness (4.21) shows that the dependence of k_s on b is linear except for the smallest values of b (Fig. 4.4). Let's make some estimates using numbers from Mark Zakhary. For a membrane of radius $a = 2.2\,\mu$m, with $B = 150 k_B T\,\mu$m, and $\Gamma = 250 k_B T/\mu$m, we get $b = B/(\Gamma a^2) \approx 0.124$, and $k_s \approx 2.73\Gamma/a$, which is significantly different from the $b = 0$ value of $k_s = (\pi/2)(\Gamma/a) \approx 1.57\Gamma/a$. Fig. 4.2 compares the theoretical small stretch slopes with experimental data.

4.4 A simplified strip model

As a first step to understanding the force for larger extensions, we can approximate the membrane as a helicoid with fixed width (i.e. a twisted rectangular ribbon). Our energy is

$$E = \bar{\kappa}\int K\mathrm{d}A + \kappa\int (2H)^2\mathrm{d}A + \gamma\int \mathrm{d}s + \frac{B}{2}\int \mathrm{d}s k^2 \tag{4.26}$$

where we have set $B' = 0$ and $c^* = 0$ (Eqn. 1.34) for now. The surface is assumed to have a helicoidal shape with length z, width ρ, and rotation rate α:

$$\underline{Y}(\bar{\rho},\bar{z}) = (\bar{\rho}\cos(\alpha\bar{z}), \bar{\rho}\sin(\alpha\bar{z}), \bar{z})\ ,\ \bar{\rho}\in[-\rho,\rho]\ ,\ \bar{z}\in[0,z], \tag{4.27}$$

so that $H = 0$. Using this parameterization to evaluate the integrals, we find

$$E(\rho,\alpha,z) = 4\gamma\rho + 2\gamma z\sqrt{1+\alpha^2\rho^2} - 2\bar{\kappa}z\frac{\alpha^2\rho}{\sqrt{1+\alpha^2\rho^2}} + Bz\frac{\alpha^4\rho^2}{(1+\alpha^2\rho^2)^{3/2}} \tag{4.28}$$

Throughout the stretching of the membrane, the helicoid is subject to the constraint of constant area: its surface area equals that of a disk of radius a. The constraint

looks like

$$\pi a^2 = z\left[\frac{1}{\alpha}\sinh^{-1}(\alpha\rho) + \rho\sqrt{1+\alpha^2\rho^2}\right] \tag{4.29}$$

Note that $E_{flat} = 4\rho\gamma + 2\gamma z$ and $A_{flat} = 2\rho z$. The energy 4.28 must be minimized subject to the constraint 4.29. We treat the extension z as fixed but arbitrary. We then find $\rho = \rho(\alpha, z)$ using 4.29. We plug this expression into 4.28 so that $E = E(\alpha, z)$ and then perform a one-dimensional minimization of the energy over $\alpha = \alpha(z)$. Plugging this value of α back into E leaves $E = E(z)$, so that the force may be computed numerically as $F = dE/dz$.

4.4.1 Asymptotic formulas for large extension

Note that the area constraint implies the bound $0 \leq \rho z \leq \pi a^2$, so that if z is large, ρ is necessarily small. We will thus perform an expansion of the constraint in terms of ρ. Note that in doing this, we are assuming α to be sufficiently small so $\alpha\rho << 1$ (in general, α depends on z and could be large). We will see later that this step is justified.

$$\frac{\pi a^2}{z} = \frac{1}{\alpha}\left(\rho\alpha - \frac{(\rho\alpha)^3}{6} + \dots\right) + \rho\left(1 + \frac{(\alpha\rho)^2}{2} + \dots\right) = 2\rho + \frac{1}{3}\alpha^2\rho^3 + \dots \tag{4.30}$$

Inverting this series to get ρ in terms of π/z gives

$$\rho = \frac{\pi a^2}{2z}\left[1 - \frac{\alpha^2}{24}\left(\frac{\pi a^2}{z}\right)^2 + \frac{13\alpha^4}{1920}\left(\frac{\pi a^2}{z}\right)^4 + \dots\right] \tag{4.31}$$

For $\alpha\rho << 1$, the energy may be expanded as

$$E \simeq 4\gamma\rho + 2\gamma z\left(1+\frac{1}{2}\alpha^2\rho^2\right) - 2\bar{\kappa}\alpha^2\rho z\left(1-\frac{1}{2}\alpha^2\rho^2\right) + Bz\alpha^4\rho^2\left(1-\frac{3}{2}\alpha^2\rho^2\right) \quad (4.32)$$

with $\rho \simeq \pi/2z$. The approximate solution for α to leading order is

$$\alpha^2 = \frac{2\bar{\kappa}z}{B\pi a^2} + O(1) \quad (4.33)$$

So, $\alpha = O(\sqrt{z})$, which confirms that $\alpha\rho \ll 1$ for $z \gg a$. Also note that α has both positive and negative roots, since the result is the same independent the chirality of the helicoid. Adding the torsion term $c^* \int ds\tau_g$ into the energy would break this degeneracy and give preference to one root over the other. Expanding the energy in $\alpha\rho$ and plugging in, we have to leading order

$$E = \left(2\gamma - \frac{\bar{\kappa}^2}{b}\right)z + O(1) \implies F = \frac{dE}{dz} = 2\gamma - \frac{\bar{\kappa}^2}{B} + O\left(\frac{1}{z^2}\right) \quad (4.34)$$

So, the force at large z is expected to saturate to a constant value depending on γ, $\bar{\kappa}$, and B (but is independent of the original radius a). In the case of a membrane that is constrained to remain flat, $\bar{\kappa} = 0$ and we recover the $F \to 2\gamma$ limit.

4.4.2 Second order strip-to-ribbon transition

From plots, we can see that the twist rate α remains zero up to a critical extension z_c. We can calculate this critical extension analytically with a Landau-type expansion: assume the energy has a critical z_c for which $\alpha = 0$ when $z \leq z_c$ and $\alpha > 0$ when $z > z_c$ and that this transition is continuous in z. Near the transition length, the helicoid is still essentially flat so that the area constraint is that of a strip: $\pi a^2 = 2\rho z$.

Expand the energy the 2nd order in α since α is small near $z = z_c$:

$$\begin{aligned} E_{helicoid} &\simeq 4\gamma\rho + 2\gamma z\left(1 + \frac{1}{2}\alpha^2\rho^2\right) - 2\bar{\kappa}z\alpha^2\rho\left(1 - \frac{1}{2}\alpha^2\rho^2\right) + \dots \\ &\simeq 4\gamma\rho + 2\gamma z + \gamma z\alpha^2\left(\frac{\pi a^2}{2z}\right)^2 - \bar{\kappa}\pi a^2\alpha^2 + \dots \\ &= E_{strip} + \alpha^2\pi a^2\left(\gamma\frac{\pi a^2}{4z} - \bar{\kappa}\right) + \dots \end{aligned}$$

The minimum energy is attained when

$$z_c = \frac{\pi a^2\gamma}{4\bar{\kappa}}. \tag{4.35}$$

Note that for a typical disk, $a = 5\mu$m, $\gamma = 1000k_BT/\mu$m, and $\bar{\kappa} = 200k_BT$ so that $z_c \simeq 10a$; in other words, an achiral membrane is not predicted to twist in this model unless it is pulled very far. The edge bending stiffness B does not enter this expression because it is higher order in α. This was all done assuming $c^* = 0$; see below for comments about chiral ribbons.

Fig. 4.5 shows the energy E, force F, twist rate α, and half-width ρ as a function of the extension z, as well as the asymptotic expressions. Notably, the force is decreasing for $z > z_c$. This is an indication of an instability; the ribbon wants to wrap up indefinitely on its own to create more negative Gaussian curvature. In order to stabilize this behavior, one could consider adding a higher order term of the form $\epsilon\int K^2 dA$, $\epsilon \ll \bar{\kappa}a^2$, which discourages infinite twist.

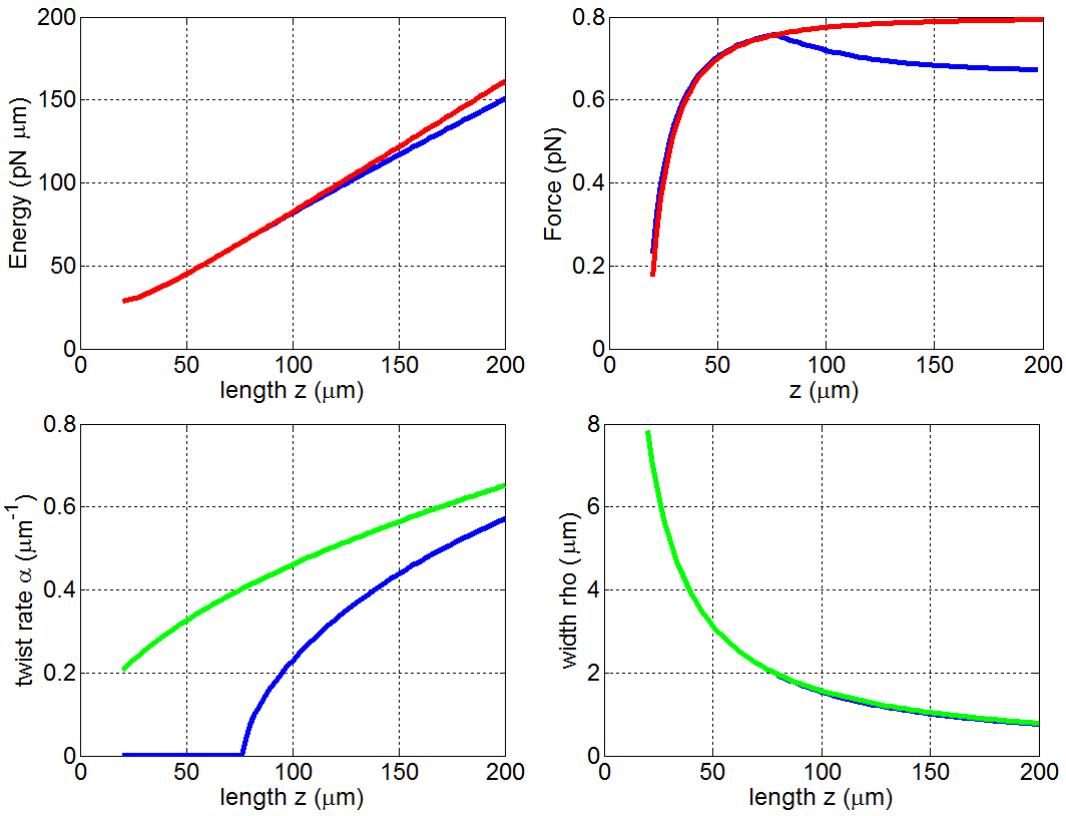

Figure 4.5: Energy E, Force F, twist rate α, and half-width ρ as a function of extension z. The green curves represent asymptotic expressions 4.31 and 4.33. In the top two plots, red indicates values for the strip while blue indicates values for the twisted ribbon.

4.4.3 Adding a chiral term

For a helicoid, the geodesic torsion is equal to the torsion. Thus,

$$c^* \int \tau_g ds = 2c^* \frac{\alpha z}{\sqrt{1+\alpha^2\rho^2}} \tag{4.36}$$

This term is linear in α, which breaks the $\pm\alpha$ symmetry and selects out a ribbon handedness as expected. However, it also invalidates the argument in the previous section; now ribbons start twisting immediately after any nonero extension, and they twist more than they do in the achiral case, as Fig 4.6 shows. This demonstrates the importance of chirality in getting ribbons to twist without having to pull to extreme lengths.

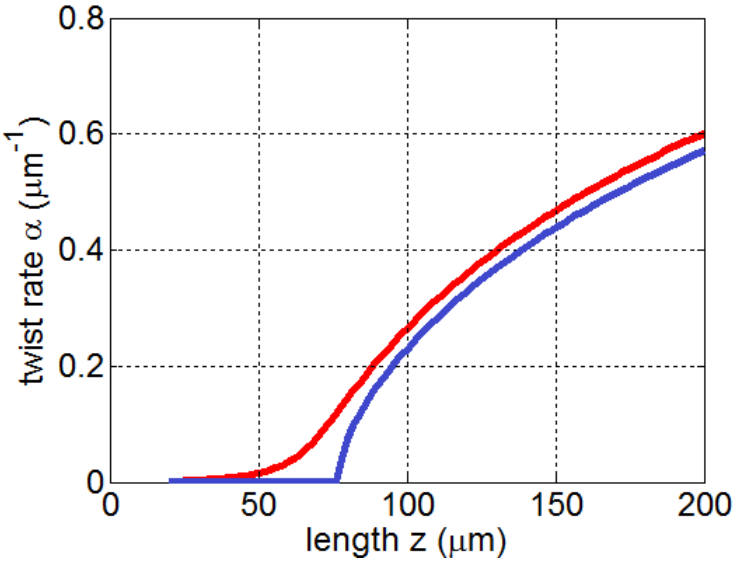

Figure 4.6: Comparison of twist rates for chiral and achiral ribbons. For the red curve (chiral), $c^* = -5k_BT$. For the blue curve (achiral), $c^* = 0$. For both curves, $a = 10\mu$m, $\bar{\kappa} = 100k_BT$, $B = 300k_BT\mu$m, and $\gamma = 100k_BT/\mu$m.

4.5 Effective model for a helicoid

Armed with an understanding of some simpler cases, we now analyze the problem of a stretched membrane that is allowed to twist. Our primary assumption will be that the surface at all extensions is a helicoid with unknown width which depends on the length coordinate, z. This assumption is justified by the expectation that the mean curvature is small in light of Section 1.3 and the only family of surfaces of the form $\underline{Y}(u,\theta) = (r(u)\cos\theta, r(u)\sin\theta, p(\theta)\theta)$ with vanishing mean curvature everywhere is the one with $p(\theta)$ constant (i.e. the pitch of the helicoid must be constant). Note that the disk with zero force applied is also a "helicoid" with infinite pitch and circular boundary.

4.5.1 Energy and Euler-Lagrange equations

Our surface thus takes the form

$$\underline{Y}(r,\theta) = (r\cos\theta, r\sin\theta, p\theta)\ ,\ 0 \le r \le R(\theta), 0 \le \theta \le Z/p \tag{4.37}$$

where c is the helicoid pitch and Z is the length of the stretched shape. Note that the surface boundary $R(\theta)$ has still not been determined. We will solve for the shape of the boundary of the surface, which is the curve $\underline{X}(\theta) = (R(\theta)\cos\theta, R(\theta)\sin\theta, p\theta)$, such that the boundary conditions in Appendix A.2 are satisfied. The pitch p will be fixed but arbitrary; a numerical optimization will be used to determine the optimal value of p;

$$p = \text{argmin}_{\bar{p}>0} E(\bar{p}, Z), \tag{4.38}$$

where $E(p, Z)$ is the full minimal model energy 1.34 without the mean curvature term:

$$E(p,Z) = \int_{\mathcal{M}} \left[\bar{\kappa}K + \mu\right] dA + \int_{\partial\mathcal{M}} \left[\gamma + \frac{B}{2}k^2 + \frac{B'}{2}\tau_g^2 + c^*\tau_g\right] ds. \tag{4.39}$$

If we use the Gauss-Bonnet theorem (Eqn. 1.13), we can write

$$E(p,Z) = \int_{\mathcal{M}} \mu dA + \int_{\partial\mathcal{M}} \left[\gamma - \bar{\kappa}k_g + \frac{B}{2}k^2 + \frac{B'}{2}\tau_g^2 + c^*\tau_g\right] ds \tag{4.40}$$

where we have ignored the constant term. It remains to write the area element in terms of ds. To this end, we calculate the metric tensor

$$g_{ij} = \underline{Y}_i \cdot \underline{Y}_j = \begin{bmatrix} 1 & 0 \\ 0 & r^2 + p^2 \end{bmatrix} \tag{4.41}$$

which gives

$$dA = \sqrt{r^2 + p^2} dr d\theta \tag{4.42}$$

Therefore, we can write

$$\int dA = \int_0^{Z/p} \int_0^{R(\theta)} \sqrt{r^2 + p^2} dr d\theta = \int_0^{X/p} \frac{1}{2} \left[R\sqrt{p^2 + R^2} + p^2 \log \left(\frac{R + \sqrt{p^2 + R^2}}{p} \right) \right] d\theta \tag{4.43}$$

The unit tangent of $\underline{X}(\theta)$ is

$$\hat{T} = (R_s \cos\theta - R \sin\theta\theta_s, R_s \sin\theta + R\cos\theta\theta_s, z_s) \tag{4.44}$$

where we have used $z = c\theta$. The identity $\hat{T} \cdot \hat{T} = 1$ yields the constraint

$$R_s^2 + z_s^2 \left(1 + \frac{R^2}{p^2} \right) = 1 \tag{4.45}$$

In analogy with the ψ from axisymmetric problems, if we define ψ to be the angle between $\hat{T}$ and the r axis, then we hve

$$d\theta = \frac{z_s}{p} ds = \frac{\sin\psi}{\sqrt{p^2 + R^2}} ds \tag{4.46}$$

Our energy thus takes the form

$$E(p, Z) = \int_{\partial\mathcal{M}} \left[\frac{\mu}{2} \left(R\sqrt{p^2 + R^2} + p^2 \log \left(\frac{R + \sqrt{p^2 + R^2}}{p} \right) \right) \frac{\sin\psi}{\sqrt{p^2 + R^2}} \right. \tag{4.47}$$

$$\left. + \Gamma - \bar{\kappa} k_g + \frac{B}{2} k^2 + \frac{B'}{2} \tau_g^2 + c^* \tau_g + \gamma(s)(r_s - \cos\psi) \right] ds \tag{4.48}$$

where we have added a local Lagrange multiplier $\gamma(s)$ in order to treat the variations in r and ψ independently, just as in previous calculations. We can then calculate

various geometric quantities:

$$\hat{n} = \left(\frac{p\sin(z/p)}{\sqrt{p^2+R^2}}, -\frac{p\cos(z/p)}{\sqrt{p^2+R^2}}, \frac{R}{\sqrt{p^2+R^2}} \right) \tag{4.49}$$

$$k_g = \hat{T} \cdot \left(\frac{d\hat{T}}{ds} \times \hat{n} \right) = \psi_s + \frac{R\sin\psi}{p^2+R^2} \tag{4.50}$$

$$k_n = \frac{d\hat{T}}{ds} \cdot \hat{n} = -\frac{p\sin 2\psi}{p^2+R^2} \tag{4.51}$$

$$k^2 = k_g^2 + k_n^2 \tag{4.52}$$

$$\tau_g = \hat{T} \cdot \left(\hat{n} \times \frac{d\hat{n}}{ds} \right) = \frac{p(1-2\cos^2\psi)}{p^2+R^2}, \tag{4.53}$$

which yield the Euler-Lagrange equations

$$\begin{aligned}
&\frac{\mu}{2}\left[1 - \frac{Rp^2}{(p^2+R^2)^{3/2}}\log\left(\frac{R+\sqrt{p^2+R^2}}{p}\right) + \frac{p^2}{p^2+R^2}\right]\sin\psi - \bar{\kappa}\sin\psi\frac{p^2-R^2}{(p^2+R^2)^2} \\
&- \frac{B\sin\psi}{(p^2+R^2)^3}\left[R(p^2(3+4\cos 2\psi)+R^2)\sin\psi + (-p^4+R^4)\psi_s\right] \\
&- \frac{B'}{2}\left[\frac{4Rp^2\cos^2(2\psi)}{(p^2+R^2)^3}\right] + c^*\frac{2pR\cos 2\psi}{p^2+R^2} - \gamma_s = 0
\end{aligned}$$

and

$$\begin{aligned}
&\frac{\mu}{2}\cos\psi\left[R + \frac{1}{\sqrt{p^2+R^2}}\log\left(\frac{R+\sqrt{p^2+R^2}}{p}\right)\right] - \bar{\kappa}\frac{R\cos\psi}{p^2+R^2} \\
&+ \frac{B}{2}\left[\frac{(p^2(-1+4\cos 2\psi)+2R^2)\sin 2\psi}{(p^2+R^2)^2} - 2\psi_{ss}\right] + \gamma\sin\psi \\
&+ c^*\frac{2p\sin 2\psi}{p^2+R^2} - B'\frac{2p^2\sin 4\psi}{(p^2+R^2)^2} = 0
\end{aligned}$$

Since the energy 4.48 was written exclusively in terms of edge quantities, the Euler-Lagrange equations are all ordinary differential equations, and they can be solved using a numerical boundary value problem solver similar to the one presented in previous chapters (see Appendix B). The eight boundary conditions that must be

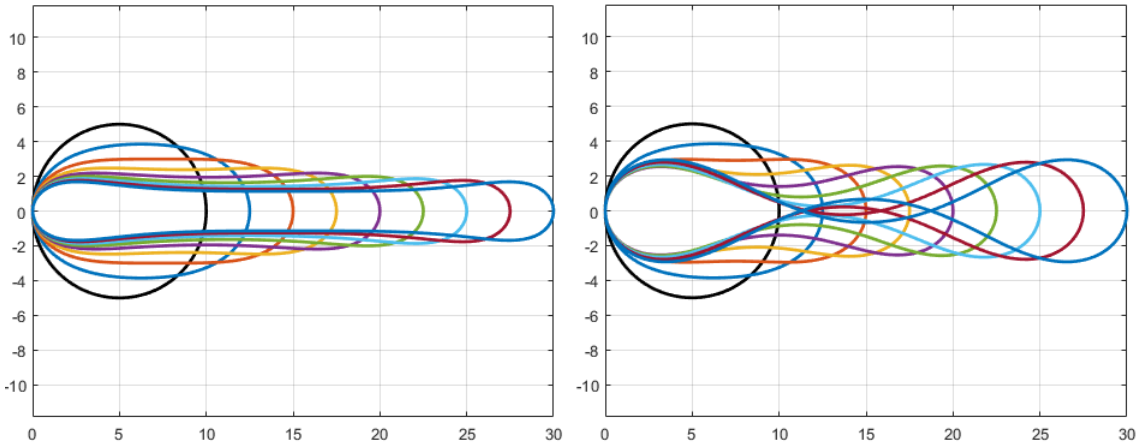

Figure 4.7: Stretched chiral (left, $c^* = 0$) and achiral (right, $c^* = -100k_BT$) membranes. In both images, ribbon has been "unwound" so that it looks flat. Achiral membranes tend to concentrate area at the ends while chiral membranes are more uniform and strip-like. For achiral membranes, it is possible (although unphysical) for the top and bottom boundaries to cross.

enforced are:

$$r(t=0)=0, r(t=1)=0, z(t=0)=Z, z(t=1)=0,$$
$$\psi(t=0)=0, \psi(t=1)=\pi, A(t=0)=0, A(t=1)=\pi a^2/2$$

where $t \equiv s/L \in [0,1]$ is the reduced arclength coordinate. In words, we have fixed endpoints, a no-torque condition at the endpoints, and the area of the helicoid must match the area of the force-free disk.

Using the numerically computed shape, we calculate $E(Z)$ by minimizing over the pitch p for fixed Z. The force needed to hold the ribbon at a given extension Z is then given by

$$F(Z) = \frac{dE}{dZ}. \tag{4.54}$$

We plot F vs. Z and compare with experiments below.

4.5.2 Achiral vs chiral ribbons

In the case where $c^* = 0$, the stretched membrane has two distinct phases: a flat phase and a twisted phase. The membrane second-order phase transitions from the flat to the twisted phase after a critical extension is reached. Much like the case for a strip, this critical stretch is quite large and not expected to be attained in typical experiments.

However, the membrane shape does not resemble a strip; most of the area is concentrated near the ends, and the waist is quite thin. For large stretches, it is even possible for the top and bottom boundaries to intersect each other, as in Fig. 4.7; note that in these images, the helicoids have been "unwound" so that the surfaces are flat. This is because nothing in the minimal model prevents the membrane from becoming infinitely thin in the middle. In the full liquid crystal energy, the large rotation of the director from one end to the other is discouraged by the twist term; in other words, our assumptions about the twist being confined to the edge break down in this regime.

On the other hand, when $c^* \neq 0$, twisting occurs after any nonzero stretch. The unraveled membrane shape closely resembles the strip since there is now a preferred geodesic torsion from the c^* term. We also see that the force is somewhat lower in the chiral case (Fig. 4.9), since the twisting means that the force is balanced by one component of the line tension in the large stretch limit.

Our results thus show the importance of chirality in the disk-to-ribbon transition. Stretching experiments on achiral ribbons have yet to be performed but would be a good way to check this result.

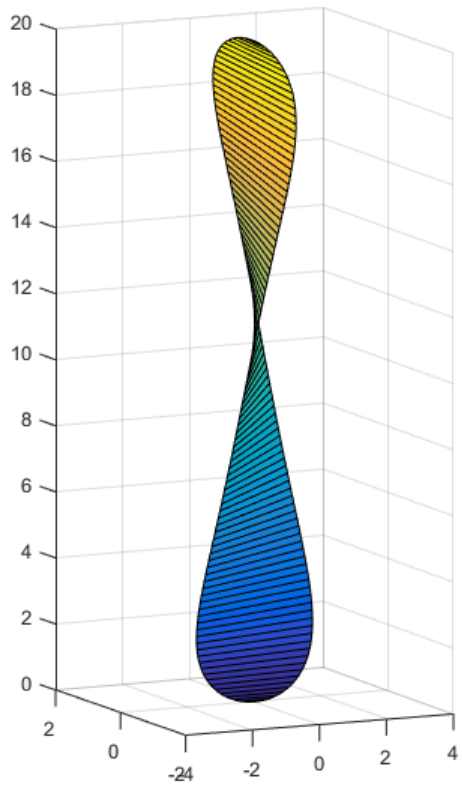

Figure 4.8: Helicoidal solution to the membrane shape equation. Chirality is needed to get twisting. Line tension $\Gamma = 1000 k_B T/\mu$n, $B = 100 k_B T \mu$m, Gaussian curvature modulus $\bar{\kappa} = 200 k_B T$, chirality modulus $c^* = 100 k_B T$, initial radus $a = 5\mu$m.

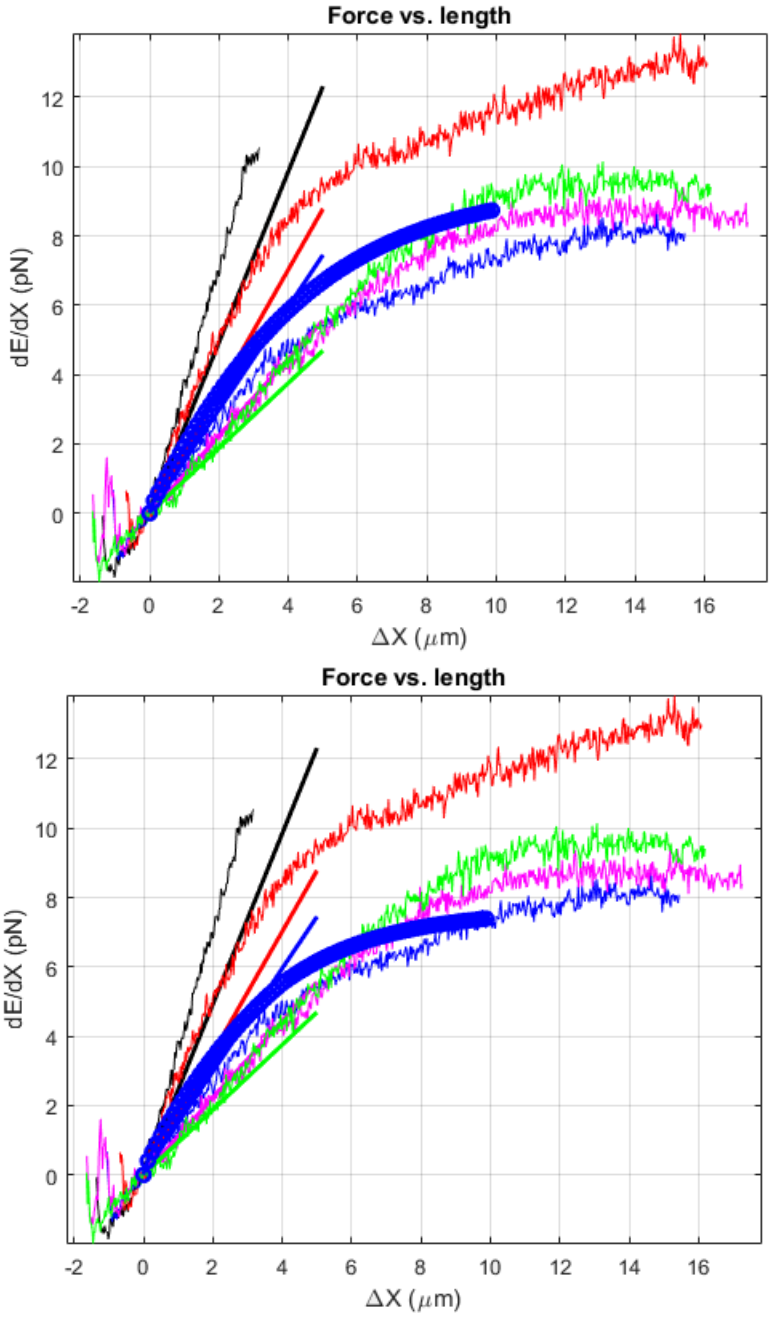

Figure 4.9: Theoretical force vs. extension curve compared to experiment. $a = 5\mu m$, $B = B' = 100k_BT\mu$m, $\bar{\kappa} = 200k_BT$, $\Gamma = 1000k_BT/\mu$m. For the top image, the membrane is achiral $c^* = 0$. For the bottom image, $c^* = -100k_BT$.

Chapter Five

Conclusion

5.1 Summary

Broadly speaking, our goal has been to investigate the diverse phases of colloidal membranes and characterize the conditions under which they appear. We have seen how a geometric minimal model based on the Canham-Helfrich membrane bending energy combined with a simplified treatment of liquid crystalline order can be used to effectively describe these shapes and transitions in membranes whose twist penetration depth is small compared to the membrane length scales. In particular, we have explored

- the role of chirality and positive Gaussian curvature modulus in producing disk-to-ribbon transitions in colloidal membranes
- the importance of chirality in making stretched membranes twist and edge bending stiffness in accurately predicting small deformation spring constants
- the highly nonlinear force vs. extension curve of a catenoidal membrane with fixed area
- the sagging of a large semipermeable colloidal vesicle in the presence of a gravitational field
- the self-assembly of axisymmetric constant mean curvature surfaces with novel topologies

Such is but a sparse sampling of the richness of phenomena that colloidal membranes demonstrate and, in fact, permeate the field of soft condensed matter physics.

5.2 Future work

There is still plenty to explore about colloidal membranes. As mentioned above, it would be interesting to study the dynamics of vesicle wrapping, the time- and lengthscales of which are too small to accurately observe for lipid bilayer vesicles. Our examination of the shapes of colloidal vesicles has hopefully laid the groundwork for this problem.

Another question is whether or not other surfaces we theoretically predict like nodoids, "flatenoids," or convex unduloids (Fig. 5.1) are physically realizable. Or, can we reach beyond axisymmetric shapes to create triunduloids or other constant mean curvature surfaces of higher genus? Preliminary experiments in this area have shown progress in the formation of these shapes, but more work is needed to determine the conditions under which they become energetically favorable compared to unduloids. Once our understanding of these shapes is improved, the next step could be to try to manufacture surfaces wth prescribed curvatures and topologies.

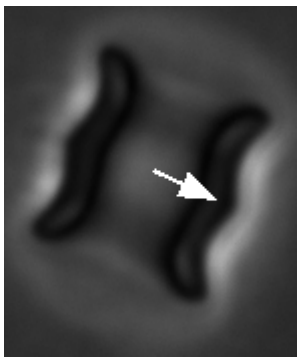

Figure 5.1: A larger unduloidal membrane formed by doping a long rod membrane with a small fraction of shorter rods. More work is needed to determine whether or not there is a defect at the location indicated by the arrow. Figure courtesy of Prerna Sharma (Indian Institute of Science).

While the colloidal membranes we have discussed are made of rod-shaped virus particles, other colloidal membranes composed of shorter DNA origami bundles have been studied as well. Interestingly, the two kinds of colloidal membranes share

different properties (e.g. parts of their phase diagrams are reversed), for reasons that are still unknown [59].

In the longer term, our understanding of these membranes is relevant to biological physics, where geometry governs many ubiquitous yet not fully understood processes like tissue formation, mitosis, cell packing, and protein folding. The theories of self-assembly that we have elucidated here could also to be applied to the engineering of complex soft materials. By continuing to study the mechanics of these membranes, we will ascertain elastic response principles that may go on to inform the design of revolutionary "living materials" capable of self-assembly and self-healing.

It is this author's hope that the research in this thesis will have contributed, even if only in some infinitesimal way, to paving the road to the answers to these questions and more. What more could I ask?

Appendix A

Force- and Torque-Free Boundary Conditions for the Minimal Model

A.1 The membrane shape equation

The minimal model analyzed in most of this document takes the form

$$E = \int_{\mathcal{M}} \left[\frac{\kappa}{2}(2H - c_0)^2 + \bar{\kappa} K + \mu \right] dA + \int_{\partial \mathcal{M}} \left[\Gamma + \frac{B}{2} k^2 + \frac{B'}{2} \tau_g^2 + c^* \tau_g \right] ds, \quad \text{(A.1)}$$

where $\kappa, \bar{\kappa}$ are elastic moduli, μ is a Lagrange multiplier enforcing the constraint of constant area, c_0 is the spontaneous curvature (zero in problems where the membrane has a uniform composition), Γ is the line tension of the edge, B is the edge bending stiffness, B' is the edge torsional stiffness, and c^* is the chirality modulus (zero for achiral rods).

The partial differential equation governing the membrane shape is the Euler-Lagrange equation associated with this energy:

$$\kappa(2H - c_0)(2H^2 - c_0 H - 2K) + \kappa \nabla^2 (2H) - 2\mu H = 0 \quad \text{(A.2)}$$

where terms at the edge only enter in the boundary conditions (see next section). The details of this calculation can be found in [65]. Note that the Gaussian curvature modulus does not appear in the shape equation because its variation vanishes.

A derivation of the membrane shape equation for the special case of axisymmetric surfaces using the coordinate system in Section 3.2 can be found in Appendix B. In the next section, we summarize the no-force and no-torque boundary conditions that naturally arise from taking the variation.

A.2 Natural boundary conditions

To find the natural boundary conditions associated with the membrane shape equation, we extend the coordinate-free variational calculuations of [65] to our energy A.1. Our notation will be the same; we assume the Frenet-Darboux frame $\{\hat{e}_1, \hat{e}_2, \hat{e}_3\}$ where $\hat{e}_1$ is the tangent vector of the boundary curve and $\hat{e}_3$ is the surface normal. The boundary curve is assumed to be parameterized with respect to arclength s. As the derivation of these relations relies heavily on the language of differential forms, which we opt not to review here, we simply state the three boundary conditions without proof.

For the edge energy

$$E_{edge} = \int_{\partial\mathcal{M}} \left[\Gamma + \frac{B}{2}k^2 + \frac{B'}{2}\tau_g^2 + c^*\tau_g\right] ds, \tag{A.3}$$

where Γ is a line tension, B is the edge bending stiffness, B' is the edge torsional stiffness, c^* is the effective chirality modulus, k_n is the normal curvature, k_g is the geodesic torsion, $k^2 = k_n^2 + k_g^2$, and τ_g is the geodesic curvature, the three boundary differential equations are

- Normal force balance:

$$B\left[\frac{d^2k_n}{ds^2} + k_n\left(\frac{k_n^2}{2} - \tau_g^2\right) + \tau_g\frac{dk_g}{ds} + \frac{d(\tau_g k_g)}{ds}\right] + \kappa\hat{e}_2\cdot\nabla(2H) - \bar{\kappa}\frac{d\tau_g}{ds} - \Gamma k_n$$
$$+c^*\left(2\tau_g k_n - \frac{dk_g}{ds}\right) + B'\left(2\tau_g^2 k_n - \frac{d}{ds}(\tau_g k_g)\right) = 0 \tag{A.4}$$

- In-plane force balance:

$$B\left[\frac{d^2k_g}{ds^2}+k_g\left(\frac{k^2}{2}-\tau_g^2\right)-\tau_g\frac{dk_n}{ds}-\frac{d(\tau_g k_n)}{ds}\right]-2\left(2\kappa H^2+\bar{\kappa}K+\mu+\Gamma k_g\right)$$
$$+c^*\left(\frac{dk_n}{ds}+2k_g\tau_g\right)+B'\left[(k_n-2H)\frac{d\tau_g}{ds}+\frac{d}{ds}(k_n\tau_g)+2k_g\tau_g^2\right]=0 \tag{A.5}$$

- Bending moment balance:

$$2\kappa H+\bar{\kappa}k_n-B'\frac{d\tau_g}{ds}=0 \tag{A.6}$$

where H is the mean curvature, K is the Gaussian curvature, κ is the bending rigidity, $\bar{\kappa}$ is the Gaussian curvature modulus, and μ is the surface tension. All quantities are assumed to be evaluated at the edge.

Appendix B

Euler-Lagrange Equations for an Axisymmetric Membrane

B.1 Euler-Lagrange equations for the minimal model

We will derive the Euler-Lagrange equations associated with the minimal model

$$E = \int_{\mathcal{M}} \left[\frac{\kappa}{2}(2H - c_0)^2 + \bar{\kappa}K + \mu\right] dA + \int_{\partial\mathcal{M}} \left[\Gamma + \frac{B}{2}k^2 + \frac{B'}{2}\tau_g^2 + c^*\tau_g\right] ds, \quad \text{(B.1)}$$

in the axisymmetric case. Denote by E_{CH} the surface integral (Canham-Helfrich energy) and E_{edge} the line integral. Here, Γ is the line tension, B is the edge bending stiffness, B' is the edge torsional stiffness, and c^* is the chirality modulus. Note that for an axisymmetric surface, the boundary curves are circles and τ_g is zero, so we need not include the c^* or B' terms. The edge energy can thus be rewritten

$$E_{edge} = 2\left(2\pi\Gamma R + \frac{B\pi}{R}\right) \quad \text{(B.2)}$$

where R is the radius of the boundary circles (here we have assumed the surface is symmetric so the boundary circles are of equal size).

Using the coordinate system outlined in Section 3.2, the area element can be rewritten as $dA = rdsd\phi$; integrating over ϕ yields a factor of 2π due to axisymmetry, which we omit.

$$E = \int_{\mathcal{M}} \left[\frac{\kappa}{2}\left(\psi_s + \frac{\sin\psi}{r} - c_0\right)^2 + \bar{\kappa}\psi_s\frac{\sin\psi}{r} + \mu\right] rds + E_{edge}, \quad \text{(B.3)}$$

However, there is one complication. The variables r and ψ are not independent; they are related by the constraint $r_s = \cos\psi$. We can resolve this difficulty by adding a Lagrange multiplier $\gamma(s)$ that enforces this constraint:

$$\int \gamma(s)(r_s - \cos\psi)ds \quad \text{(B.4)}$$

Note that $\gamma(s)$ is a function, not a constant, as the constraint needs to be enforced locally as opposed to globally.

We now proceed to take the variation in ψ to derive the Euler-Lagrange equation:

$$\begin{aligned}
\delta F_H &= \int \left[\kappa r \left(\psi_s + \frac{\sin\psi}{r} - c_0 \right) \left(\delta\psi_s + \frac{\cos\psi}{r}\delta\psi \right) + \bar{\kappa}(\delta\psi_s \sin\psi + \psi_s \cos\psi\delta\psi) + \gamma \sin\psi\delta\psi \right] ds \\
&= \int \left[-\kappa \left[r \left(\psi_s + \frac{\sin\psi}{r} - c_0 \right) \right]_s + \kappa \left(\psi_s + \frac{\sin\psi}{r} - c_0 \right) \cos\psi + \gamma \sin\psi \right] \delta\psi ds \\
&= \int \left[-\kappa r_s \left(\psi_s + \frac{\sin\psi}{r} - c_0 \right) - \kappa r \left(\psi_s + \frac{\sin\psi}{r} \right)_s + \kappa \left(\psi_s + \frac{\sin\psi}{r} - c_0 \right) \cos\psi + \gamma \sin\psi \right] \delta\psi d \\
&= \int \left[-\kappa r \psi_{ss} - \kappa \cos\psi\psi_s + \kappa \frac{\sin\psi\cos\psi}{r} + \gamma \sin\psi \right] \delta\psi ds
\end{aligned}$$

The variation in r is:

$$\begin{aligned}
\delta F_H &= \int \left[\frac{\kappa}{2} \left(\psi_s + \frac{\sin\psi}{r} - c_0 \right)^2 \delta r + \kappa r \left(\psi_s + \frac{\sin\psi}{r} - c_0 \right) \left(\frac{-\sin\psi}{r^2}\delta r \right) + \mu\delta r + \gamma\delta r_s \right] ds \\
&= \int \left[\frac{\kappa}{2} (\psi_s - c_0)^2 - \frac{\kappa}{2}\frac{\sin^2\psi}{r^2} + \mu - \gamma_s \right] \delta r ds
\end{aligned}$$

Thus, the Euler-Lagrange equations for an axisymmetric surface (the shape equation expressed in in r and ψ) are

$$-\kappa r \psi_{ss} - \kappa \cos\psi\psi_s + \kappa \frac{\sin\psi\cos\psi}{r} + \gamma \sin\psi = 0 \tag{B.5}$$

$$\frac{\kappa}{2} (\psi_s - c_0)^2 - \frac{\kappa}{2}\frac{\sin^2\psi}{r^2} + \mu - \gamma_s = 0 \tag{B.6}$$

$$r_s = \cos\psi \tag{B.7}$$

B.2 Force- and Torque-free boundary conditions for the minimal model

The aforementioned `bvp4c` method requires the system to be written as a system of first order ordinary differential equations, so we need an equal number of boundary conditions.

From the variation in ψ in the previous section, we see that

$$\kappa(2H) + \bar{\kappa}\frac{\sin\psi}{r}\bigg|_{s=0,L} = 0 \tag{B.8}$$

which is the condition of vanishing bending moment at the edge (note that the normal curvature of the boundary ring is $\sin\psi/r$, so this coincides with what is given in [65]). On the other hand, force balance in the r-direction at the edge yields the equation

$$\Gamma + \gamma - \frac{B}{2r^2}\bigg|_{s=0,L} = 0 \tag{B.9}$$

The area constraint implies that

$$A(s=0) = 0 \tag{B.10}$$

$$A(s=L) = A_0 \tag{B.11}$$

where A_0 is the area of the membrane and we have defined the cumulative area function for an axisymmetric surface as

$$A(s) = 2\pi\int_0^s r(v)dv. \tag{B.12}$$

The above boundary conditions are assumed to be evaluated at the edge.

B.3 The transversality condition for problems with unknown length

If the total length of the curve L is unknown, as it commonly is when using the arclength parameterization, then the length can be solved for by including it as a variable in the system of ordinary differential equations. Define the reduced arclength $t = s/L$. We add a new equation

$$L_t = 0 \tag{B.13}$$

which necessitates a new boundary condition. The extra boundary condition needed to close this system is the transversality condition in the case of zero external force. If we vary the geometric quantities in Eqn. B.3 [40]:

$$\begin{aligned} \psi(s) &= \psi_0(s) + \delta\psi(s), \\ r(s) &= r_0(s) + \delta\psi(s), \\ \gamma(s) &= \gamma_0(s) + \delta\gamma(s), \\ s_1 &= s_{1,0} + \delta s_1, \\ s_2 &= s_{2,0} + \delta s_2, \end{aligned} \tag{B.14}$$

then the variation of E is

$$\begin{aligned} \delta E = \int_{s_1}^{s_2} ds \left[\left(\frac{\partial \mathcal{L}}{\partial \psi} - \frac{d}{ds}\frac{\partial \mathcal{L}}{\partial \psi_s} \right) \delta\psi + \left(\frac{\partial \mathcal{L}}{\partial r} - \frac{d}{ds}\frac{\partial \mathcal{L}}{\partial r_s} \right) \delta r + \frac{\partial \mathcal{L}}{\partial \gamma}\delta\gamma \right] \\ - \mathcal{H}\delta s\big|_{s_1}^{s_2} + \frac{\partial \mathcal{L}}{\partial \psi_s}\delta\psi\bigg|_{s_1}^{s_2} + \frac{\partial \mathcal{L}}{\partial r_s}\delta r\bigg|_{s_1}^{s_2} \end{aligned} \tag{B.15}$$

where the "Lagrangian" $\mathcal{L}$ is the integrand of E_{CH}, as written out in Eqn. B.3, and $\mathcal{H}$ is the corresponding Hamiltonian

$$\mathcal{H} = -\mathcal{L} + \psi_s \frac{\partial \mathcal{L}}{\partial \psi_s} + r_s \frac{\partial \mathcal{L}}{\partial r_s}. \tag{B.16}$$

Physically, $\mathcal{H}$ represents the force in the z-direction. The fact that the Hamiltonian is constant throughout the membrane is a consequence of the energy not depending explicitly on the variable s; in other words, $\mathcal{H}$ is the Noether invariant associated with this symmetry and has the physical interpretation of the force in the z-direction. In the absence of external forces, Eqn. B.15 yields the condition

$$\mathcal{H} = 0, \tag{B.17}$$

which is also known as a transversailty condition in the terminology of calculus of variations [15].

Reworking the s equations B.5- B.7 into the t variable, so that the first point corresponds to $t = 0$ and the last point of the curve corresponds to $t = 1$, the seven unknowns are

$$u_1 = \psi, u_2 = \psi_s, u_3 = r, u_4 = \gamma, u_5 = A, u_6 = \mu, u_7 = L, \tag{B.18}$$

satisfying the seven first order autonomous ordinary differential equations

$$\begin{aligned}
\frac{du_1}{dt} &= u_7 u_2 \\
\frac{du_2}{dt} &= \frac{u_7}{\kappa u_3}\left[\kappa u_2 \cos u_1 + \kappa \frac{\sin u_1 \cos u_1}{u_3} + u_4 \sin u_1\right] \\
\frac{du_3}{dt} &= u_7 \cos u_1 \\
\frac{du_4}{dt} &= u_7\left[\frac{\kappa}{2}(u_2 - c_0)^2 - \frac{\kappa}{2}\frac{\sin^2 u_1}{u_3^2} + u_6\right] \\
\frac{du_5}{dt} &= 2\pi u_7 u_3 \\
\frac{du_6}{dt} &= 0 \\
\frac{du_7}{dt} &= 0
\end{aligned} \tag{B.19}$$

The seven boundary conditions are Eqns. B.8- B.11, along with B.17. One can then use a computational routine such as MATLAB's `bvp4c` to solve the system B.19 numerically.

B.4 Euler-Lagrange equations for the full liquid crystal energy

We now derive the Euler-Lagrange equations for the more general problem, without making the simplifications of the liquid crystalline order being confined to the edge. If we use the Frank-deGennes energy to model the liquid crystalline interaction, we need to find an equation for θ, the tilt angle of the rods relative to the surface normal, as well as the contributions due to θ to the normal force balance, leading to modifications of the membrane shape equation. Let the shape of the meridian be defined as $r(z)$, $z \in [-R, R]$ with angle of rotation $\phi \in [0, 2\pi)$.

Suppose the central axis the z-axis so that we can parameterize the surface as $\underline{Y}(s,\phi) = (r(z(s))\cos\phi, r(z(s))\sin\phi, z(s))$, where $s \in [0, s_0]$ is the arclength of the meridian. The relevant geometric quantities are the tangent vectors

$$\underline{Y}_1 = \hat{e}_1 = \partial_s \underline{Y} = (r_s \cos\phi, r_s \sin\phi, z_s) \tag{B.20}$$

$$\underline{Y}_2 = f\hat{e}_2 = \partial_s \underline{Y} = (-r\sin\phi, r\cos\phi, 0), \tag{B.21}$$

the first fundamental form

$$g_{ij} = \begin{bmatrix} \underline{Y}_1 \cdot \underline{Y}_1 & \underline{Y}_1 \cdot \underline{Y}_2 \\ \underline{Y}_1 \cdot \underline{Y}_2 & \underline{Y}_2 \cdot \underline{Y}_2 \end{bmatrix} = \begin{bmatrix} 1 & 0 \\ 0 & r^2 \end{bmatrix} \implies g = r^2, \tag{B.22}$$

where $z_s = 1/\sqrt{1 + r'(z)^2}$. Since s is arclength, we note we have a constraint $z_s^2 + r_s^2 = 1$.

Next, we calculate the Christoffel symbols (the formulas are simplified because g_{ij} is diagonal):

$$\Gamma^1_{11} = g^{11}\underline{Y}_{11} \cdot \underline{Y}_1 = r_s r_{ss} + z_s z_{ss} = 0 \tag{B.23}$$

$$\Gamma^1_{12} = g^{11}\underline{Y}_{12} \cdot \underline{Y}_1 = 0 \tag{B.24}$$

$$\Gamma^1_{22} = g^{11}\underline{Y}_{22} \cdot \underline{Y}_1 = -r r_s \tag{B.25}$$

$$\Gamma^2_{11} = g^{22}\underline{Y}_{11} \cdot \underline{Y}_2 = 0 \tag{B.26}$$

$$\Gamma^2_{12} = g^{22}\underline{Y}_{12} \cdot \underline{Y}_2 = r_s/r \tag{B.27}$$

$$\Gamma^2_{22} = g^{22}\underline{Y}_{22} \cdot \underline{Y}_2 = 0 \tag{B.28}$$

The outward unit surface normal vector is $\hat{N} = -(\underline{Y}_1 \times \underline{Y}_2)/\sqrt{g} = (z_s \cos\phi, z_s \sin\phi, -r_s)$.

This gives the second fundamental form

$$b_{ij} = \begin{bmatrix} \underline{Y}_{11} \cdot \hat{N} & \underline{Y}_{12} \cdot \hat{N} \\ \underline{Y}_{12} \cdot \hat{N} & \underline{Y}_{22} \cdot \hat{N} \end{bmatrix} = \begin{bmatrix} r_{ss} z_s - z_{ss} r_s & 0 \\ 0 & -r z_s \end{bmatrix} = \begin{bmatrix} r_{ss}/z_s & 0 \\ 0 & -r z_s \end{bmatrix} \implies b = -r r_{ss} \tag{B.29}$$

since $z_s z_{ss} + r_s r_{ss} = 0$.

Using B.22 and B.29, we find the mean and Gaussian curvatures

$$H = \frac{1}{2} L_{ij} g^{ij} = (r r_{ss} z_s - z_{ss} r r_s - z_s)/2r = \frac{1}{2}\left(\frac{r_{ss}}{z_s} - \frac{z_s}{r}\right) \tag{B.30}$$

$$K_G = b/g = -r_{ss}/r. \tag{B.31}$$

Now, we calculate the terms that appear in the Frank energy. Note that due to the unit norm constraint $g_{ij} n_i n_j + \cos^2\theta = 1$, the director field takes the form

$$\hat{n} = \left(0, \frac{\sin\theta(z)}{\sqrt{g_{22}}}, \cos\theta(z)\right) = \left(0, \frac{\sin\theta}{f}, \cos\theta\right) \tag{B.32}$$

in the $\{\underline{Y}_1, \underline{Y}_2, \hat{N}\}$ basis.

$$\nabla \cdot \hat{n} = \partial_j n_j + n_l \Gamma^j_{jl} - 2H\cos\theta = -2H\cos\theta = -\cos\theta\left(\frac{f_{ss}}{z_s} - \frac{z_s}{f}\right) \tag{B.33}$$

$$\begin{aligned} \hat{n} \cdot (\nabla \times \hat{n}) &= \frac{\epsilon_{3ji}}{\sqrt{g}} \left[\cos\theta (g_{ik}\partial_j n_k + g_{il} n_k \Gamma^l_{jk}) - (n_k n_l g_{il} L_{jk} + g_{il} n_l \partial_j \cos\theta)\right] \\ &= -\frac{1}{\sqrt{g}}\left[\cos\theta g_{11} n_2 \Gamma^1_{22}\right] + \frac{1}{\sqrt{g}}\left[\cos\theta (g_{22}\partial_1 n_2 + g_{22} n_2 \Gamma^2_{12}) - g_{22} n_2 \partial_1 \cos\theta\right] \\ &= -\frac{1}{f}\left[\cos\theta(-f_s \sin\theta)\right] + \frac{1}{f}\left[\cos\theta\left(f\cos\theta\theta_s - \sin\theta f_s + \sin\theta f_s\right) + f\sin^2\theta\theta_s\right] \\ &= \theta_s + \frac{f_s}{f}\sin\theta\cos\theta \end{aligned} \tag{B.34}$$

$$\begin{aligned}\nabla \times \hat{n} &= \frac{\epsilon_{3ji}}{\sqrt{g}}\left[(g_{ik}\partial_j n_k + g_{il}n_k\Gamma^l_{jk})\hat{N} - (n_k L_{jk} + \partial_j \cos\theta)\underline{Y}_i\right] \\ &= -\frac{1}{\sqrt{g}}\left[g_{11}n_2\Gamma^1_{22}\hat{N} - n_2 L_{22}\underline{Y}_1\right] + \frac{1}{\sqrt{g}}\left[\left(g_{22}\partial_1 n_2 + g_{22}n_2\Gamma^2_{12}\right)\hat{N} - \partial_1\cos\theta\underline{Y}_2\right] \\ &= -\frac{z_s}{f}\sin\theta\underline{Y}_1 + \frac{1}{f}\sin\theta\theta_s\underline{Y}_2 + \left(\frac{f_s}{f}\sin\theta + \cos\theta\theta_s\right)\hat{N} \qquad \text{(B.35)}\end{aligned}$$

$$\begin{aligned}(\nabla\times\hat{n})^2 &= -\frac{z_s^2}{f^2}\sin^2\theta + \frac{\sin^2\theta}{f^2}\theta_s^2 + \left(\frac{f_s}{f}\sin\theta + \cos\theta\theta_s\right)^2 \\ &= \theta_s^2 + \frac{\sin^2\theta}{f^2} + \frac{\theta_s f_s}{f}\sin 2\theta \qquad \text{(B.36)}\end{aligned}$$

Putting B.33- B.36 together, the deGennes energy density is

$$\begin{aligned}F_n &= \int\left(\frac{1}{2}K\left[(\nabla\cdot\hat{n})^2 - 2q\hat{n}\cdot(\nabla\times\hat{n}) + (\nabla\times\hat{n})^2 + q^2\right] + \frac{1}{2}C\sin^2\theta\right)\sqrt{g}ds \\ &= \int\left(\frac{1}{2}K\left[(2H\cos\theta)^2 - 2q\left(\theta_s + \frac{r_s}{r}\sin\theta\cos\theta\right) + \theta_s^2 + \frac{\sin^2\theta}{r^2} + \frac{\theta_s r_s}{r}\sin 2\theta + q^2\right]\right. \\ &\left.+\frac{1}{2}C\sin^2\theta\right) r ds \\ &= \int\frac{1}{2}\left(K\left[(2H\cos\theta)^2 + (\theta_s - q)^2 + \sin 2\theta\frac{r_s}{r}(\theta_s - q) + \frac{\sin^2\theta}{r^2}\right] + C\sin^2\theta\right) r ds\end{aligned}$$

where we have used an equivalent form of the deGennes energy [44].

The variation in θ is

$$\begin{aligned}\delta F_n = \int\frac{1}{2}\Big(K\Big[&-2(2H\cos\theta)(2H\sin\theta\delta\theta) + 2(\theta_s - q)\delta\theta_s + \sin 2\theta\frac{r_s}{r}\delta\theta_s + 2\cos 2\theta\frac{r_s}{r}(\theta_s - q)\delta\theta \\ &+\frac{\sin 2\theta}{r^2}\delta\theta\Big] + C\sin 2\theta\delta\theta\Big) r ds \qquad \text{(B.37)}\end{aligned}$$

$$\begin{aligned}&= \int\frac{1}{2}\left(K\left[-r(2H)^2\sin 2\theta - 2[r(\theta_s - q)]_s - (\sin 2\theta r_s)_s + 2\cos 2\theta r_s(\theta_s - q) + \frac{\sin 2\theta}{r}\right]\right. \\ &\left.+ Cr\sin 2\theta\right)\delta\theta ds.\end{aligned}$$

The variation in r is

$$\delta F_n = \int \frac{1}{2}\left(K\left[(2H\cos\theta)^2 - \frac{2}{r}(2H)\cos^2\theta\sin\psi + (\theta_s - q)^2 - \frac{\sin^2\theta}{r^2}\right] + C\sin^2\theta\right)\delta r ds \tag{B.38}$$

The variation in ψ is

$$\begin{aligned}\delta F_n &= \delta\int \frac{K}{2} r\cos^2\theta(2H)^2 ds \\ &= \int Kr\cos^2\theta(2H)\left(\delta\psi_s + \frac{\cos\psi}{r}\delta\psi\right)ds \\ &= \int K\left([-r\cos^2\theta(2H)]_s + \cos^2\theta(2H)\cos\psi\right)\delta\psi ds\end{aligned} \tag{B.39}$$

The three variations give us the contributions to the Euler-Lagrange equations from the liquid crystalline energy, which give the Euler-Lagrange equations

$$-\kappa r\psi_{ss} - \kappa\cos\psi\psi_s + \kappa\frac{\sin\psi\cos\psi}{r} + \gamma\sin\psi + K\left([-r\cos^2\theta(2H)]_s + \cos^2\theta(2H)\cos\psi\right) = 0 \tag{B.40}$$

and

$$\frac{\kappa}{2}(\psi_s - c_0)^2 - \frac{\kappa}{2}\frac{\sin^2\psi}{r^2} + \mu - \gamma_s + \frac{1}{2}\left(K\left[(2H\cos\theta)^2 - \frac{2}{r}(2H)\cos^2\theta\sin\psi + (\theta_s - q)^2 - \frac{\sin^2\theta}{r^2}\right] + C\sin^2\theta\right) = 0. \tag{B.41}$$

Note that when K and C are zero, we recover the equations B.5 and B.6. The new equation governing the field θ is

$$-(2H)^2\sin 2\theta - 2\frac{1}{r}[r(\theta_s - q)]_s - \frac{1}{r}(\sin 2\theta r_s)_s + 2\cos 2\theta\frac{r_s}{r}(\theta_s - q) + \frac{\sin 2\theta}{r^2} + \frac{1}{\lambda^2}\sin 2\theta = 0. \tag{B.42}$$

where the twist penetration depth is $\lambda = \sqrt{K/C}$.

B.5 Force- and Torque-free boundary conditions for the full liquid crystal energy

In the process of computing the variation of F_n in the previous section, we obtain the folloing new natural boundary conditions:

From the ψ-variation (no bending moment condition), we get

$$\bar{\kappa}\frac{\sin\psi}{r} + (\kappa + K\cos^2\theta)(2H)\Big|_{s=0,L} = 0. \tag{B.43}$$

From the r-variation (radial force condition, unchanged from before),

$$\Gamma + \gamma - \frac{B}{2r^2}\Big|_{s=0,L} = 0. \tag{B.44}$$

Note that the constant B can be set to zero here since the bend energy is already accounted for in the full liquid crystalline energy.

From the θ-variation, the boundary equations for the θ equation are

$$2(\theta_s - q) + \sin 2\theta\frac{\cos\psi}{r}\Big|_{s=0,L} = 0. \tag{B.45}$$

We still have the area conditions

$$A(s=0) = 0 \text{ and } A(s=L) = A_0 \tag{B.46}$$

at the endpoints.

As above, we require an additional boundary condition to close the system. Let

$\mathcal{L}$ be the integrand of the free energy.

$$\begin{aligned}\mathcal{L}/2\pi = &\left[\frac{\kappa}{2}\left(\psi_s + \frac{\sin\psi}{r}\right)^2 + \bar{\kappa}\frac{\psi_s \sin\psi}{r} + \mu\right] r + \gamma(r_s - \cos\psi) \\ &+ \frac{1}{2}\left(K\left[(2H\cos\theta)^2 + (\theta_s - q)^2 + \sin 2\theta \frac{r_s}{r}(\theta_s - q) + \frac{\sin^2\theta}{r^2}\right] + C\sin^2\theta\right) r\end{aligned} \tag{B.47}$$

Since $\partial\mathcal{L}/\partial s = 0$, we have a conserved quantity

$$\mathcal{H} = -\mathcal{L} + \psi_s \frac{\partial\mathcal{L}}{\partial\psi_s} + r_s \frac{\partial\mathcal{L}}{\partial r_s} + \theta_s \frac{\partial\mathcal{L}}{\partial\theta_s} \tag{B.48}$$

We compute

$$\begin{aligned}\frac{\mathcal{H}}{2\pi} &= -\frac{\kappa}{2} r\,(2H)^2 + \kappa r \psi_s (2H) - \mu r + \gamma\cos\psi \\ &- \frac{1}{2} K r \left((2H\cos\theta)^2 - 2\psi_s \cos^2\theta (2H) + (\theta_s - q)^2 - 2\theta_s(\theta_s - q) - \sin 2\theta \frac{r_s}{r} q + \frac{\sin^2\theta}{r^2}\right) \\ &- \frac{1}{2} C r \sin^2\theta \\ &= \frac{r}{2}\left(\kappa + K\cos^2\theta\right)\left(\psi_s^2 - \frac{\sin^2\psi}{r^2}\right) - \mu r + \gamma\cos\theta + \frac{K}{2} r\left(\theta_s^2 - q^2\right) - \frac{K}{2}\frac{\sin^2\theta}{r} \\ &- \frac{C}{2} r\sin^2\theta + \frac{K}{2}\sin 2\theta\cos\psi\theta_s\end{aligned} \tag{B.49}$$

Again, the transversality condition implies that

$$\mathcal{H} = 0 \tag{B.50}$$

is the missing boundary condition, corresponding to the unknown length L of the curve.

Bibliography

[1] M. W. Allersma, F. Gittes, M. J. deCastro, R. J. Stewart, and C. F. Schmidt. Two-dimensional tracking of ncd motility by back focal plane interferometry. *Biophys. J.*, **74**:1074, 1998.

[2] S. Asakura and F. Oosawa. On interaction between two bodies immersed in a solution of macromolecules. *J. Chem. Phys.*, **22**:1255, 1954.

[3] S. Asakura and F. Oosawa. Interaction between particles suspended in solutions of macromolecules. *J. Polym. Sci.*, **33**:183, 1958.

[4] A. Balchunas and Z. Dogic. Private communication.

[5] E. Barry, D. Beller, and Z. Dogic. A model liquid crystalline system based on rodlike viruses with variable chirality and persistence length. *Soft Matter*, **5**:2563, 2009.

[6] E. Barry and Z. Dogic. Entropy driven self-assembly of nonamphiphilic colloidal membranes. *Proc. Natl. Soc. USA*, **107**:10348, 2010.

[7] E. Barry, Z. Dogic, R. B. Meyer, R. A. Pelcovits, and R. Oldebourg. Direct measure of the twist penetration length in a single smectic A layer of colloidal virus particles. *J. Phys. Chem. B*, **113**:3910, 2009.

[8] E. Barry, Z. Hensel, Z. Dogic, M. Shribak, and R. Oldenbourg. Entropy-driven formation of a chiral liquid-crystalline phase of helical filaments. *Phys. Rev. Lett.*, **96**:018305, 2006.

[9] E. Bendito, M. J. Bowick, and A. Medina. Delaunay surfaces. *J. Geom. Symmetry Phys.*, **33**:27, 2014.

[10] M. Bergner, A. Dall'Acqua, and S. Frölich. Willmore surfaces of revolution with two prescribed boundary circles. *J. Geom. Anal.*, **23**:283, 2011.

[11] D. Boal. *Mechanics of the cell.* Cambridge University Press, Cambridge, 2002.

[12] Ph. Boltenhagen, O. D. Lavrentovich, and M. Kléman. Focal conic domains with positive Gaussian curvature and saddle-splay rigidity of smectic l_α phases. *Phys. Rev. A*, **46**:R1743, 1992.

[13] P.B. Canham. The minimum energy of bending as a possible explanation of the biconcave shape of the human red blood cell. *J. Theor. Biol.*, **26**:61–81, 1970.

[14] L. V. Chernomordik and M. M. Kozlov. Mechanics of membrane fusion. *Nat. Struct. Mol. Biol.*, **15**:675, 2008.

[15] R. Courant and D. Hilbert. *Methods of Mathematical Physics I.* Interscience Publishers, New York, NY, 1953.

[16] A. Dall'Acqua, K. Deckelnick, and H.-C. Grunau. Rotationally symmetric classical solutions to the dirichlet problem for willmore surfaces. *Adv. Calc. Var.*, **1**:379, 2008.

[17] A. Dall'Acqua, S. Fröhlich, H.-C. Grunau, and F. Schieweck. Symmetric willmore surfaces of revolution satisfying arbitrary dirichlet boundary data. *Adv. Calc. Var.*, **4**:1, 2010.

[18] P. G. de Gennes. *The Physics of Liquid Crystals.* Clarendon Press, Oxford, 1974.

[19] P. G. de Gennes and C. Taupin. Microemulsions and the flexibility of oil/water interfaces. *J. Phys. Chem.*, **86**:2294, 1982.

[20] C. Delaunay. Sur la surface de révolution dont la courbure moyenne est constante. *J. Math. Pures Appl.*, **6**:309, 1841.

[21] D. E. Discher and F. Ahmed. Polymersomes. *Annu. Rev. Biomed. Eng.*, 8:323, 2006.

[22] M. do Carmo. *Differential Geometry of Curves and Surfaces.* Prentice-Hall, Englewood Cliffs, NJ, 1976.

[23] Z. Dogic and S. Fraden. Cholesteric phase in virus suspensions. *Langmuir*, **16**:7820, 2000.

[24] Z. Dogic and S. Fraden. Development of model colloidal liquid crystals and the kinetics of the isotropic-smectic transition. *Phil. Trans. R. Soc. Lond. A*, **359**:997, 2001.

[25] J. Eells. The surfaces of delaunay. In *Mathematical Conversations.* Springer, Springer, NY, 2001.

[26] E. Evans and W. Rawicz. Entropy-driven tension and bending elasticity in condensed-fluid membranes. *Phys. Rev. Lett.*, **64**:2094, 1990.

[27] T. Gibaud, E. Barry, M. J. Zakhary, M. Henglin, A. Ward, Y. Yang, C. Berciu, R. Oldenbourg, M. F. Hagan, D. Nicastro, R. B. Meyer, and Z. Dogic. Reconfigurable self-assembly through chiral control of interfacial tension. *Nature*, **481**:348, 2012.

[28] T. Gibaud, C. N. Kaplan, P. Sharma, A. Ward, M. J. Zakhary, R. Oldenbourg, R. B. Meyer, and Z. Dogic. Achiral symmetry breaking and positive Gaussian modulus lead to scalloped colloidal membranes. *Proc. Natl. Acad. Sci*, **114**:E3376, 2017.

[29] L. Giomi and L. Mahadevan. Minimal surfaces bounded by elastic lines. *Proc. Roy. Soc. A*, **468**:1851, 2012.

[30] E. Grelet and S. Fraden. What is the origin of chirality in the cholesteric phase of virus suspensions? *Phys. Rev. Lett.*, **90**:198302, 2003.

[31] J. Guven, G. Huber, and D. M. Valencia. Terasaki spiral ramps in the rough endoplasmic reticulum. *Phys. Rev. Lett.*, **113**:188101, 2014.

[32] M. Hadzhilazova, I. M. Mladenov, and J. Oprea. Unduloids and their geometry. *Archivum Mathematicum*, **43**:417, 2007.

[33] W. Helfrich. Elastic properties of lipid bilayers: theory and possible experiments. *Z. Naturforsh.*, **28c**:693, 1973.

[34] W. Helfrich. The size of bilayer vesicles generated by sonification. *Phys. Rev. Lett.*, **50A**:115, 1974.

[35] W. Helfrich and H. J. Deuling. Some theoretical shapes of red blood cells. *J. Phys. (Paris) Colloq.*, 36:C1–327, 1975.

[36] M. Hu, J. J. Briguglio, and M. Deserno. Determining the Gassign curvature modulus of lipid membranes in simulations. *Biophys. J.*, **102**:1403, 2012.

[37] M. Hu, D. H. de Jong, S. J. Marrink, and M. Deserno. Gaussian curvature elasticity determined from global shape transformations and local stress distributions: a comparative study using the MARTINI model. *Faraday Discuss.*, **161**:365, 2013.

[38] L. L. Jia, M. Zakhary, Z. Dogic, R. A. Pelcovits, and T. R. Powers. Chiral edge fluctuations of colloidal membranes. *Phys. Rev. E*, **95**:060701, 2017.

[39] H. Jiang, G. Huber, R. A. Pelcovits, and T. R. Powers. Vesicle shape, molecular tilt, and the suppression of necks. *Phys. Rev. E*, **76**:031908, 2007.

[40] F. Jülicher and U. Seifert. Shape equations for axisymmetric vesicles: A clarification. *Phys. Rev. E*, **49**:4728, 1994.

[41] R. D. Kamien. The geometry of soft materials: a primer. *Rev. Mod. Phys.*, **74**:953–971, 2002.

[42] L. Kang, T. Gibaud, Z. Dogic, and T. C. Lubensky. Entropic forces stabilize diverse emergent structures in colloidal membranes. *Soft Matter*, **12**:386, 2016.

[43] C. N. Kaplan, T. Gibaud, and R. B. Meyer. Intrinsic curvature determines the crinkled edges of "crenelated disks". *Soft Matter*, **9**:8210, 2013.

[44] C. N. Kaplan, H. Tu, R. A. Pelcovits, and R. B. Meyer. Theory of depletion-induced transition from chiral smectic-A twisted ribbons to semi-infinite flat membranes. *Phys. Rev. E*, **82**:021701, 2010.

[45] K. Kenmotsu. Surfaces of revolution with prescribed mean curvature. *Tohoku Math. J.*, **32**:147, 1980.

[46] L. D. Landau and E. M. Lifshitz. *Theory of elasticity*. Pergamon Press, Oxford, 3rd edition, 1986.

[47] A. W. C. Lau, A. Prasad, and Z. Dogic. Condensation of isolated semi-flexible filaments driven by depletion interactions. *EPL*, **87**:48006, 2009.

[48] M. P. Lettinga, E. Barry, and Z. Dogic. Self-diffusion of rod-like viruses in the nematic phase. *Europhys. Lett.*, **71**:692, 2005.

[49] S. T. Milner and T. A. Witten. Bending moduli of polymeric surfactant interfaces. *J. Phys. France*, **49**:1951, 1988.

[50] D. C. Morse. Topological instabilities and phase behavior of fluid membranes. *Phys. Rev. E*, **50**:R2423, 1994.

[51] R. A. Pelcovits and R. B. Meyer. Twist penetration in single-layer smectic A discs of colloidal virus particles. *Liq. Cryst.*, **36**:1157, 2009.

[52] T. R. Powers. Dynamics of filaments and membranes in a viscous fluid. *Rev. Mod. Phys.*, **82**:1607, 2010.

[53] W. Rawicz, K. C. Olbrich, T. McIntosh, D. Needham, and E. Evans. Effect of chain length and unsaturation on elasticity of lipid bilayers. *Biophys. J.*, **79**:328, 2000.

[54] S. A. Safran. *Statistical Thermodynamics of Surfaces, Interfaces, and Membranes*. Perseus Books, Cambridge, MA, 1994.

[55] J. Sambrook, E. F. Fritsch, and T. Maniatis. *Molecular Cloning*. Cold Spring Harbor Laboratory Press, Cold Spring Harbor, NY, 1989.

[56] Udo Seifert, Karin Berndl, and Reinhard Lipowsky. Shape transformation of vesicles: phase diagram for spontaneous-curvature and bilayer-coupling models. *Phys. Rev. A*, **44**:1182, 1991.

[57] F. R. Senti, N. N. Hellman, N. H. Ludwig, G. E. Babcock, R. Tobin, C. A Glass, and B. L. Lamberts. Viscosity, sedimentation, and light-scattering properties of fraction of an acid-hydrolyzed dextran. *J. Polym. Sci..*, **17**:527, 1955.

[58] Peter Shary, Larisa S. Sharaya, and Andrey Mitusov. The problem of scale-specific and scale-free approaches in geomorphometry. *Geografia Fisica e Dinamicca Quaternaria*, **28**:81, 01 2005.

[59] M. Siavashpour, M. Zakhary, C. Wachauf, H. Dietz, and Z. Dogic. Self-assembly of dna origami particles in suspension of non-absorbing depleting polymers. *APS Meeting Abstracts*, **1**:49008, 2015.

[60] D. P. Siegel and M. M. Kozlov. The Gaussian curvature elastic modulus of N-monomethylated dioleoylphosphatidylethanolamine: relevance to membrane fusion and lipid behavior. *Biophys. J.*, **87**:366, 2004.

[61] D.J. Struik. *Lectures on classical differential geometry*. Dover Publications, New York, 2nd edition, 1988.

[62] I. Szleifer, D. Kramer, A. Ben-Shaul, W. M. Gelbart, and S. A. Safran. Molecular theory of curvature elasticity in surfactant films. *J. Chem. Phys.*, **92**:6800, 1990.

[63] M. Terasaki, T. Shemesh, N. Kasthuri, R. W. Klemm, R. Schalek, K. J. Hayworth, A. R. Hand, M. Yankova, G. Huber, J. W. Lichtman, T. A. Rapoport, and M. M. Kozlov. Stacked endoplasmic reticulum sheets are connected by helicoidal membrane motifs. *Cell*, **154**:285, 2013.

[64] Z. Tu. Geometry of membranes. *J. Geom. Symmetry Phys.*, **24**:45, 2011.

[65] Z. C. Tu and Z. C. Ou-Yang. A geometrical theory on the elasticity of biomembranes. *J. Phys. A: Math. Gen.*, **37**:11407, 2004.

[66] Z.-G. Wang. Curvature instability of diblock copolymer bilayers. *Macromolecules*, **25**:3702, 1992.

[67] H. H. Wensink and L. Morales Anda. Elastic moduli of a smectic membrane: a rod-level scaling analysis. *J. Phys.: Condens. Matter*, **30**:075101, 2018.

[68] T. J. Willmore. A survey on willmore immersions. In *Geometry and Topology of Submanifolds, IV*. World Scientific Pub. Co., Leuven, Belgium, 1992.

[69] M. J. Zakhary, T. Gibaud, C. N. Kaplan, E. Barry, R. Oldenbourg, R. B. Meyer, and Z. Dogic. Imprintable membranes from incomplete chiral coalescensce. *Nature Comm.*, **5**:3063, 2014.

[70] M. J. Zakhary, Prerna Sharma, A. Ward, S. Yardimici, and Z. Dogic. Geometrical edgeactants control interfacial bending rigidity of colloidal membranes. *Soft Matter*, **9**:8306, 2013.